INVESTIGATIONS OF INTERFACE PHENOMENA VIA ATOMISTIC SIMULATION

by

James Francis Hickman
A Dissertation
Submitted to the
Graduate Faculty
of
George Mason University
in Partial Fulfillment of
The Requirements for the Degree
of
Doctor of Philosophy
Physics

Committee:

_____	Dr. Yuri Mishin, Dissertation Director
_____	Dr. Karen Sauer, Committee Member
_____	Dr. Erhai Zhao, Committee Member
_____	Dr. Daniel Anderson, Committee Member
_____	Dr. Paul So, Department Chair
_____	Dr. Donna M. Fox, Associate Dean, Office of Student Affairs & Special Programs, College of Science
_____	Dr. Peggy Agouris, Dean, College of Science

Date: _____ Fall Semester 2017
George Mason University
Fairfax, VA

Investigations of interface phenomena via atomistic simulation

A dissertation submitted in partial fulfillment of the requirements for the degree of Doctor of Philosophy at George Mason University

By

James Francis Hickman
Master of Science
George Mason University, 2014
Bachelor of Science
Shippensburg University, 2011

Director: Dr. Yuri Mishin, Professor
Department of Physics and Astronomy

Fall Semester 2017
George Mason University
Fairfax, VA

Dedication

To Edward Thomas Hickman

Acknowledgments

First I would like to thank my advisor Dr. Yuri Mishin for his patience, direction, motivation, support, and advice. Additionally I would like to thank my dissertation committee members for their help and feedback. I also would like to thank all of my previous professors at Shippensburg University for giving me a strong fundamental understanding of physics and math as well as a desire to pursue these disciplines in greater detail. Finally, I want to acknowledge the support of my girlfriend Lillian Parker and my family: parents Ed and Mary Hickman, brothers Ed and John Hickman, and grandparents Elmer and Gertrude Greey.

Table of Contents

Page

List of Tables . . . vii
List of Figures . . . viii
Abstract . . . xvi
1 Introduction . . . 1
1.1 Atomistic simulations . . . 1
1.2 Thermodynamics . . . 2
1.2.1 The micro-canonical ensemble . . . 2
1.2.2 Generalized canonical ensembles . . . 3
1.3 Grain boundaries . . . 6
1.4 Grain boundary pre-melting . . . 8
1.5 Variation in local grain boundary density . . . 10
1.6 Canonical temperature fluctuations . . . 10
2 Methodology . . . 12
2.1 Interatomic potentials . . . 12
2.2 The molecular dynamics Method . . . 14
2.2.1 NVE molecular dynamics . . . 16
2.2.2 NVT molecular dynamics . . . 17
2.3 The Monte Carlo method . . . 17
3 Grain boundary premelting . . . 19
3.1 Theory . . . 21
3.1.1 The liquid layer model of grain boundary premelting . . . 21
3.1.2 Disjoining potential near the solidus line . . . 26
3.1.3 Fluctuations of grain boundary width . . . 27
3.1.4 Types of disjoining potentials . . . 28
3.2 Methodology of simulations . . . 32
3.2.1 Simulation of bulk phases . . . 32
3.2.2 Grain boundary simulations . . . 37
3.2.3 Calculation of the grain boundary width distribution . . . 39

3.2.4 Calculation of the disjoining potential 41
3.2.5 Calculation of properties for thermodynamic integration 43
3.3 Simulation results and interpretation 45
3.3.1 Grain boundary premelting in pure Cu 45
3.3.1.1 Premelting behavior and disjoining potentials 45
3.3.1.2 Free energy of premelted grain boundaries 49
3.3.2 Grain boundary premelting in Cu-Ag solutions 53
3.3.2.1 Premelting behavior and disjoining potentials 53
3.3.2.2 Chemical composition of grain boundaries 58
3.3.2.3 Free energy of premelted grain boundaries 63
3.4 Conclusions 66
4 Generality of metallic grain boundary phases 68
4.1 Simulation methods 68
4.1.1 Fixed GB density minimization 70
4.1.2 Variable GB density minimization 70
4.2 Fixed GB density results 72
4.3 Variable GB density results 74
4.3.1 Structural units 74
4.3.2 Validation of methodology 75
4.3.3 Additional results 77
4.3.4 Silver and Aluminum results 81
4.4 Conclusions 83
5 Canonical ensemble temperature fluctuations 84
5.1 Theory 86
5.2 Methodology of simulations 90
5.2.1 Molecular dynamics simulations 90
5.2.2 Post-processing procedures 91
5.3 Simulation results and discussion 92
5.3.1 NVE simulations 92
5.3.2 NVT simulations 94
5.3.3 Additional tests 102
5.4 Conclusions 106
6 Summary 108
A GB structure catalog 110
Bibliography 117

List of Tables

Table Page

1.1 Abbreviations for common thermodynamic ensembles 6

3.1 Solid-liquid coexistence properties on the Cu-rich side of the Cu-Ag system: The diffusion potential M^*, the solidus and liquidus compositions c_S^* and c_L^*, and the volume per atom in the liquid phase v_L^*. 1325.25 K is the estimated melting point of pure Cu. 36

3.2 Properties of the three symmetrical tilt GBs studied in this work: the lattice rotation angle around the [001] tilt axis, the 0 K GB energy γ, the number of atoms in the simulation block N, and the block dimensions. The GB plane is normal to the z-axis. 38

4.1 Here we provide a list of the various boundaries sampled in this work as well as the energies of these boundaries when they take the form of networks of regular kites 74

A.1 A comparison of the energies associated with the regular kite K_1 with the new global minima obtained in this work. In the rightmost column the new values with energies lower than that of regular kites are displayed in bold font 110

List of Figures

Figure Page

1.1 Schematic of the canonical system defined in the context of an isolated system decomposed into a reservoir and a canonical subsystem 5

1.2 Schematic showing two common classes of grain boundaries (a) a tilt grain boundary (b) a twist grain boundary and (c) the conventional unit cell of the FCC crystal system with cubic Miller directions and an example of the (100) plane depicted (image source: [24, 25]) 7

2.1 Schematic example of a classical atomic system 15

3.1 Premelted GB subject to a normal stress σ_{zz}. The GB region is modeled by a uniform liquid layer of width w bounded by interacting solid-liquid interfaces. 22

3.2 Traditional classification of disjoining potentials into repulsive and attractive. (a) Potential shapes. (b) Equilibrium GB width as a function of undercooling ΔT or undersaturation ΔM for the two types of potentials. The vertical line marks the equilibrium melting point (respectively, solidus line). The dashed curve represents unstable GB states. 29

3.3 Disjoining potentials proposed in this work: repulsive, attractive and intermediate. (a) Potential shapes. Note that the attractive and intermediate potentials have a shallow maximum in the tail region. (b) Non-equilibrium GB free energy $\hat{\gamma}$ relative to $2\gamma_{SL}$ as a function of GB width for the three potential types. The red dashed line represents the term $-p_d^0 w$. The minima of $\hat{\gamma}$ correspond to equilibrium GB states. Note that the intermediate potential creates two local minima corresponding to GB states with widths w_0 and w_0'. (c) Equilibrium GB width as a function of undercooling ΔT or undersaturation ΔM for the intermediate disjoining potential. The green vertical line shows the thin-to-thick transition in the GB. The long vertical line marks the equilibrium melting point (respectively, solidus line). The dashed curve represents unstable GB states. 30

3.4 Chemical composition profiles across the (210) solid-liquid interface in the Cu-Ag system at several temperatures. The interface position was determined from the order parameter profile as explained in the text. The inset shows the relevant portion of the phase diagram with the solid and liquid compositions marked by the points. 31
3.5 Right: Phase diagram of the Cu-Ag system calculated with the EAM potential [131] utilized in this work. Left: Zoomed-in view of the Cu rich side of the phase diagram showing the sampling method of temperatures and compositions studied in this work. 35
3.6 Atomic structures of three GBs studied in this work. The tilt axis [001] is normal to the page and the kite-shaped structural units are outlined. The red and black atoms belong to alternating (002) atomic planes. 37
3.7 Typical order parameter profile used to calculate the GB width in a single snapshot. The blue points are raw values of the structure factor $|S_i|(z_i)$ and the red curve is the smoothed profile $\phi_i(z_i)$. The simulation was for the $\Sigma 5$ GB at 1200 K with the grain composition of 2.23 at.%Ag. The upper image shows the atomic positions projected along the [001] tilt axis normal to the page, with yellow points representing Cu atoms and blue points Ag atoms. 40
3.8 Probability density functions $P_i(w_i)$ for different values of ΔM (in eV) computed for the $\Sigma 5$ GB at the temperature of 1000 K. The inset shows the segments of the disjoining potential extracted from these functions. The curves are the normalized distributions predicted by the analytical disjoining potential. 42
3.9 Premelting of the Cu $\Sigma 5$ GB at three different temperatures below the bulk melting point. The atomic positions are projected along the [001] tilt axis normal to the page. The number in parentheses is the undercooling ΔT. . 46
3.10 Width probability distributions $P(w)$ for three GBs in Cu at 1310 K ($\Delta T = -15.25$ K) with snapshots of the premelted structures. The points represent the original histograms while the curves are the normalized distributions predicted by the analytical disjoining potential. The atomic positions are projected along the [001] tilt axis normal to the page. The numbers indicate the GB widths in the snapshots. 47
3.11 Average GB width $\bar{w}$ as a function of undercooling ΔT for the pure Cu GBs. 48

3.12 Probability density functions for different undercoolings ΔT (in K) for the $\Sigma 5$ GB in pure Cu. The points represent the original histograms while the curves are the normalized distributions predicted by the analytical disjoining potential. The inset shows segments of the disjoining potential obtained by inversion of individual probability functions. 49
3.13 Disjoining potentials for three GBs in pure Cu. The points represent simulation results from the GB width fluctuations. The solid lines are analytical disjoining potentials fitted to the points as discussed in the text. 50
3.14 Excess energy per unit area, $\tilde{U}/A$, as a function of temperature for three GBs in pure Cu. The vertical line indicates the bulk melting point. 51
3.15 GB free energy as a function of temperature for three GBs in pure Cu. The main plot shows the results of thermodynamic integration. The inset compares these results with predictions of the liquid layer model near the melting point (points). 52
3.16 Premelted structures of the $\Sigma 5$ GB at the temperature of 1100 K at different undersaturations Δc (at.%Ag). The atomic positions are projected along the [001] tilt axis normal to the page, with yellow points representing Cu atoms and blue points Ag atoms. 54
3.17 Average width of the (a) $\Sigma 5$, (b) $\Sigma 17$ and (c) $\Sigma 13$ GBs in Cu-Ag solid solutions as a function of the diffusion potential ΔM relative the solidus line. The points represent individual simulations. The solid lines are Bezier curves intended to show the trends. 55
3.18 Disjoining potentials for the $\Sigma 5$ GB in the Cu-Ag solid solution at the three different temperatures and in pure Cu. The insets show the fits of the simulation results (points) by the analytical function $\Psi(w)$ (curves). The main plot summarizes the fitted functions. 56
3.19 Disjoining potentials for the $\Sigma 17$ GB in the Cu-Ag solid solution at the three different temperatures and in pure Cu. The insets show the fits of the simulation results (points) by the analytical function $\Psi(w)$ (curves). The main plot summarizes the fitted functions. Note the transition of the disjoining potential from repulsive to intermediate with decreasing temperature. . . . 57

3.20 Probability density functions for different values of ΔM (in eV) computed for the $\Sigma 17$ GB at the temperature of 1000 K. The points represent the original histograms while the curves are the normalized distributions predicted by the analytical disjoining potential. The inset shows segments of the disjoining potential obtained by inversion of individual probability functions. 58
3.21 A typical fragment of MC simulations for the $\Sigma 17$ GB at 1000 K with undersaturation $\Delta M = -0.0012$ eV. The GB spontaneously switches between two states, labeled A and B, with different widths. Multiple repetitions of such switches produce two peaks in the width probability distribution $P(w)$. The insets show order parameter profiles in snapshots drawn from the two states. The GB widths in the snapshots are indicated. 59
3.22 Disjoining potentials for the $\Sigma 13$ GB in the Cu-Ag solid solution at the three different temperatures and in pure Cu. The insets show the fits of the simulation results (points) by the analytical function $\Psi(w)$ (curves). The main plot summarizes the fitted functions. 60
3.23 Chemical composition c_{GB} at the center of the GB region normalized by the liquidus composition c_L^* as a function of undersaturation ΔM. The lines are Bezier curves intended to highlight the trends. 61
3.24 Chemical compositional profiles (normalized by the liquidus composition c_L^*) across the $\Sigma 5$ GB for different undersaturations ΔM (eV) at the temperature of 1000 K. 62
3.25 Segregation isotherms for the $\Sigma 17$ GB at three temperatures. The vertical dashed lines mark the solidus compositions c_S^*. 63
3.26 Free energy of the (a) $\Sigma 5$, (b) $\Sigma 17$ and (c) $\Sigma 13$ GBs in the Cu-Ag solution at the three temperatures sampled. The solid lines in the main plot were obtained by thermodynamic integration. The dotted lines are linear interpolations to the solidus line ($\Delta c = 0$). The inset compares these results with predictions of the liquid layer model (points) near the solidus. 64
3.27 Solid-liquid interface free energies in the Cu-Ag system computed in this work from GB premelting simulations. The interface planes are indicated in the legends. For comparison, the plot includes γ_{SL} of the (110) interface computed in previous work.[39] 65

4.1 Schematic of the simulation block orientation and the geometry of the subset used to calculate the 0K GB free energy for a given configuration. 69

4.2 Here we show a subset of the results for the special case in which the GB density is fixed ($N_{rm} = 0$). Using the "translate and minimize" method the minimum energy structures appears to be networks of regular kite units no matter how large or small the tilt angle is. The images which show the kite structure are taken by projecting the simulation block down the [001] tilt axis however the center right images shows a projection down the $[1\bar{2}0]$ direction (the $[k\bar{h}0]$ projection for all other regular kite boundaries is similar to the one shown) 73

4.3 Structural units (a) K, (b) L and (c) M found in [001] symmetrical tilt GBs in Cu. The structures are projected parallel to the [001] tilt axis (upper row) and normal to the tilt axis (lower row). The GB density λ are indicated. . . 75

4.4 In this figure we show our results for the two $\Sigma 5$ boundaries. a) (310) boundary and b) (210) Notice that in both grain boundaries the split kite structures emerge near the center of the curves whereas in the (210) boundary there is an additional local minima around $\lambda = 0.14$ which is associated with filled kites. For the various minima we show images of the kite structures which are projections down the [001] tilt axis. For the split kites we also include images projected down the $[k\bar{h}0]$ directions. The blue lines running through the points are bezier curves included as a guide for the eye. 76

4.5 The results of the moving window procedure discussed in the text for the case of the (210) boundary. The blue points are the raw data and the red points are the minimum values chosen by the moving window procedure. The line in the plot are bezier curves fitted to the red points and is included as a guide for the eye 77

4.6 GB energy (in $\mathrm{J\,m^{-2}}$) versus GB density λ (fraction of atoms removed) for representative symmetrical tilt GBs in Cu. For GBs composed on identical structural units, the data points are shown by symbols representing the respective structural units (◇ K, □ L, ◯ M, see Fig. 4.3). The diamond symbols in (a) and (f) represent metastable structures composed structural units K. All other points represent stable structures that minimize the GB energy for each density λ. The dashed line in (b) is an example of a tie line between two GB phases producing cups of the energy. The trend lines are shown as a guide to the eye. 78

4.7 GB energy as a function of GB density λ and misorientation angle θ for [001] symmetrical tilt boundaries in Cu. The actual simulation points are indicated. 81

4.8 GB energy (in $\mathrm{J/m^2}$) versus GB density λ (fraction of atoms removed) for symmetrical tilt GBs in Ag. 82

4.9 GB energy versus GB density λ (fraction of atoms removed) for (a) $\Sigma 17\,(410)$ and (b) $\Sigma 5\,(210)$ GBs in Al. The trend lines are shown as a guide to the eye. The most stable structure of the $\Sigma 5\,(210)$ GBs is composed of M units as shown in (c). 83

5.1 Results of NVE MD simulations. (a) Normalized power spectrum $\hat{C}_{\Delta K \Delta K}(f)$ of kinetic energy fluctuations (filled circles), velocity ACF $\hat{C}_{vv}(f/2)$ (open circles), and phonon density of states $g(f/2)$ (solid line). (b) The kinetic energy ACF $C_{\Delta K \Delta K}(t)$. 93

5.2 Representative fluctuations of the kinetic (blue) and total (orange) energy in the NVT ensemble with the thermostat time constants (a) $\tau_r = 10$ ps and (b) $\tau_r = 100$ ps. To enable comparison, the energies were shifted relative to the average values and normalized by the standard deviations. The insets zoom into shorter time intervals to demonstrate the existence of two different timescales of the fluctuations (fast and slow). 95

5.3 Normalized difference between the right and left-hand sides of fluctuation relations as functions of the averaging time interval θ: Eq.(5.1) (black solid line), Eq.(5.2) (red dashed line) and Eq.(5.3) (blue dotted line) . (a) Langevin thermostat with $t_r = 10$ ps, (b) Langevin thermostat with $t_r = 100$ ps, (c) natural thermostat. 96

5.4 Normalized power spectra of kinetic and total energy fluctuations in the NVT ensemble with a Langevin thermostat for two different time constants (10 and 100 ps). Square and triangle symbols - kinetic energy, circle and nabla symbols - total energy. 98
5.5 Results of NVT MD simulations with a Langevin thermostat ($\tau_r = 10$ ps). (a) Comparison of the kinetic energy ACF and kinetic-potential energy CCF in the frequency domain. Note that both spectra have the same shape but opposite sign at high frequencies and coincide at low frequencies. (b) Comparison of the total energy ACF and kinetic-total energy CCF in the frequency domain. Both functions show a similar monotonic decrease with frequency and die off above $1/\tau_r$. 98
5.6 Energy correlation functions in the time domain obtained by NVT MD simulations with a Langevin thermostat ($\tau_r = 10$ ps). The inset is a zoom into the short-range part of the kinetic energy ACF. 99
5.7 The NVT kinetic energy ACF for a Langevin thermostat with $\tau_r = 10$ ps (red curve) superimposed on the NVE kinetic energy ACF (blue points). The inset shows a zoom into the short-time region. 101
5.8 The anatomy of the "natural" thermostat implemented in this work. (a) Vertical cross-section of the simulation block revealing the cubic system under study at the center, the thermostat regions above and below the system, and a fixed shell enclosing both the system and the thermostat. The entire assembly is much longer in the vertical (z) direction than shown. (b) and (c) show horizontal (x-y) cross-sections at the levels indicated by the arrows. . 103
5.9 Power spectra of kinetic energy from NVT MD simulations of systems connected to a natural thermostat and two Langevin thermostats with the time constants of 10 and 100 ps. 105
A.1 GB energy (in J/m^2) versus GB density λ (fraction of atoms removed) for symmetrical tilt GBs in Cu. 111
A.2 GB energy (in J/m^2) versus GB density λ (fraction of atoms removed) for symmetrical tilt GBs in Cu. 112
A.3 Structures of symmetrical tilt GBs in Cu. The structures are projected parallel to the [001] tilt axis (left) and normal to the tilt axis (right). The GB density λ are indicated. 113

A.4 Structures of symmetrical tilt GBs in Cu. The structures are projected parallel to the [001] tilt axis (left) and normal to the tilt axis (right). The GB density λ is indicated. 114
A.5 Structures of symmetrical tilt GBs in Cu. The structures are projected parallel to the [001] tilt axis (left) and normal to the tilt axis (right). The GB density λ is indicated. 115
A.6 Structures of symmetrical tilt GBs in Cu. The structures are projected parallel to the [001] tilt axis (left) and normal to the tilt axis (right). The GB density λ is indicated. The structures are composed of M units whose connection to each other alternates along the tilt axis from head-to-tail to separated by an extra plane. This explains why the projection along the tilt axis does not look like in other boundaries. 116

Abstract

INVESTIGATIONS OF INTERFACE PHENOMENA VIA ATOMISTIC SIMULATION

James Francis Hickman, PhD

George Mason University, 2017

Dissertation Director: Dr. Yuri Mishin

In the first section of the thesis we examine a phenomenon known as grain boundary (GB) pre-melting in binary systems. Many GBs develop highly disordered, liquid-like structures at high temperatures. In alloys, this effect is less understood as it can be fueled by solute segregation to the boundary. In single component systems, pre-melted GBs are often modeled by a thin liquid layer located between two solid-liquid interfaces interacting via a disjoining potential. We have extended this formalism to binary systems and proposed a single analytical form of the disjoining potential that describes repulsive, attractive and intermediate interactions. The potential is verified by Monte Carlo simulations of three different GBs in Cu-Ag alloys modeled using an embedded atom potential. The proposed approach is generic and can be applied to other alloys in the future.

In section two we introduce a new thermodynamic parameter to the standard description of GBs. Traditionally, GBs are described by five crystallographic angles, which are assumed to fully define the GB structure and energy. Recently, it was realized that variations in a GB's atomic density λ can drastically alter its structure and can cause transformations between different GB phases. Our work extends the previous studies by computing the structures and energies of a large set of [001] symmetrical tilt GBs by allowing arbitrary variations in λ.

In the final section we apply theoretical analysis and molecular dynamics (MD) to elucidate the meaning of temperature fluctuations in canonical systems. We validate a well-known but frequently contested thermodynamic equation predicting the variance of temperature fluctuations. The results clearly demonstrate the existence of quasi-equilibrium states in which a canonical system can be characterized by a well-defined temperature and obeys the aforementioned fluctuation equation.

Chapter 1: Introduction

This dissertation contains three separate projects focusing on grain boundary (GB) premelting in binary systems, the addition of a new variable to the standard description of a grain boundary, and finally a discussion of a novel interpretation of temperature fluctuations in canonical systems. These projects are all unified by their use of a general simulation methodology, a focus on solid state metallic systems, an emphasis on crystalline defects, and the use thermodynamic fluctuation theory. The first chapter introduces relevant general concepts and discusses the scientific and practical significance of the various projects. In the second chapter we provide an overview of the general methods and techniques which are common to all three projects. The third and fourth chapters focus on GB structures, properties and thermodynamic behaviors. Finally in the fifth chapter we address canonical temperature fluctuations.

1.1 Atomistic simulations

The research described in this thesis relies heavily on atomistic simulations as a primary tool for analyzing the phenomena in question. Simulations of this kind are useful for modeling a wide range of materials including amorphous structures, liquids, 2D materials, bulk crystalline phases, and crystals containing defects.

Broadly speaking atomic simulations fall into two methodological categories. The first category corresponds to quantum mechanical (QM) methods such as density functional theory (DFT) and quantum chemical calculations. The QM methods are highly accurate but computationally slow, system size limited, and are often restricted to zero Kelvin simulations. The second category corresponds to faster but less accurate classical methods such as molecular dynamics (MD) or Monte Carlo (MC) simulations. These methods describe

atoms as discrete point particles confined to a box which constitutes the simulation domain. The classical methods facilitate investigations of phenomena which are inaccessible to QM simulations, for instance, many mechanical processes such as nano-indentation, and dislocation nucleation. They also permit a direct treatment of temperature effects and thus enable the modeling many kinetics-dominated processes such as crystal growth and thermal conductivity. In the present work we work exclusively with the classical MC and MD methods which will be discussed more throughly in Sec. 2.

1.2 Thermodynamics

When carrying out either MD or MC simulations the user must specify how the system interacts with the outside world. This is achieved by running the simulations using different choices of thermodynamics ensembles. The various ensembles, e.g. micro-canonical, canonical, isothermal–isobaric, grand-canonical...etc, are defined based on how the system in question interacts with the outside world. To begin we will address the micro-canonical case.

1.2.1 The micro-canonical ensemble

The micro-canonical ensemble describes a system which is completely isolated with no external interactions. As an example consider a completely isolated simple monoatomic fluid, for this system, the equilibrium state is fully defined by the following extensive variables: energy E, volume V, and number of particles N. The entropy S of an isolated equilibrium system is a function of E, V, and N. This function can be established by equilibrating the isolated system with different values of E, V, and N and then measuring or computing S for each set of these parameters. The function $S = S(E, V, N)$ is called the fundamental equation [19, 47, 93] and it incapsulates *all* thermodynamic properties of the substance. It is important to note that, because of the isolation, the variables E, V, and N are fixed by conservation laws and therefore do not fluctuate in time. For the simple fluid the

intensive parameters are temperature T, pressure p and chemical potential μ. These quantities are defined by the fundamental equation as the partial derivatives $T = 1/(\partial S/\partial E)$, $p = T(\partial S/\partial V)$, and $\mu = -T(\partial S/\partial N)$. It is also common to see the fundamental equation written so that E plays the role of the dependent variable, i.e. $E(S, V, N)$, which has the differential given by Eq.(1.1)

$$\begin{aligned} dE &= \left(\frac{\partial E}{\partial S}\right)_{V,N} dS + \left(\frac{\partial E}{\partial V}\right)_{S,N} dV + \left(\frac{\partial E}{\partial N}\right)_{V,S} dN \\ &= TdS - pdV + \mu dN. \end{aligned} \tag{1.1}$$

Finally, the different types of internal equilibrium within the system, i.e. thermal, mechanical, and chemical, are defined by the uniformity of the respective intensive variable across the entirety of the system.

1.2.2 Generalized canonical ensembles

The rest of the thermodynamic ensembles can be are referred to as generalized canonical ensembles [93]. These ensembles describe systems which are not isolated but interact with a so called "reservoir" through the exchange of one or more extensive variables. This exchange facilitates equilibration with the reservoir and therefore the reservoir in effect regulates one or more of the system's intensive variables.

To make the concept more concrete we will address the standard canonical ensemble as an example. For reasons discussed below this ensemble is also referred to as the NVT ensemble. Consider a large isolated equilibrium system with fixed parameters E_T, V_T, and N_T. This system will be referred to as the "total system". Assume the total system is composed of two parts, first a small sub-system with a fixed volume V and a fixed number of particles N. Assume that this subsystem can exchange energy with the rest of the system but only through heat exchange. Next assume that the remainder of the total system, referred to as the reservoir or thermostat, is much much larger than the sub-system. We

will denote quantities corresponding to the reservoir by the subscript R and properties of the subsystem with the absence of subscript. A physical example of a canonical system is a gas trapped in a rigid box with chemically inert but heat conducting walls in a sealed room which has a constant and uniform temperature. In this example the room plays the role of the reservoir while the gas in the box is the canonical subsystem. Because of the conservation laws the reservoir will also have a fixed number of particles $N_R = N_T - N$ and a fixed volume $V_R = V_T - V$. Returning to the subsystem, it is clear that its energy will fluctuate with time, i.e $E = E(t)$ where $E_T = cnst = E_R(t) + E(t)$. Because of these fluctuations it is necessary to introduce average values for any subsystem quantity which is a function of the energy E. For a general property $x(E)$, the average can be computed in two ways. First it can be calculated by integrating the product of $x(E)$ and the probability density function $P(E)$ as shown in Eq. 1.2

$$\langle x \rangle = \int_{-\infty}^{\infty} x(E)P(E)dE. \tag{1.2}$$

The quantity $\langle x \rangle$ is known as the ensemble average and the probability distribution depends on the choice of ensemble. For the NVT ensemble the probability distribution it the well known Gibbs-Boltzmann distribution [70]. Alternatively the averages can also be computed by measuring the quantity for a long enough time that it completely explores all possible states and then taking the time average as given by Eq. 1.3

$$\overline{x} = \lim_{T \to \infty} \int_0^T x(t)dt. \tag{1.3}$$

For an ergodic system the time average is equivalent the ensemble average, this is the case for all of the various thermodynamic ensembles. The equilibrium states for the subsystem and the reservoir are denoted with a subscript 'o' and correspond their average values, i.e. $E_o = \langle E \rangle$. A given fluctuation ΔE of the subsystem is quantified by the system's "distance"

from equilibrium which is given by $\Delta E = E(t) - E_o$. The magnitude of these fluctuations are quantified by the mean square deviation $\left\langle (\Delta E)^2 \right\rangle$ which is also known as the variance. Finally because the total system is assumed to be in thermal equilibrium we have $\langle T \rangle = \langle T_R \rangle$ and therefore the reservoir can be viewed as a heat bath which regulates the temperature of the subsystem via the heat exchange [18, 93]. A schematic of the canonical (NVT) system is shown in Fig. 1.1.

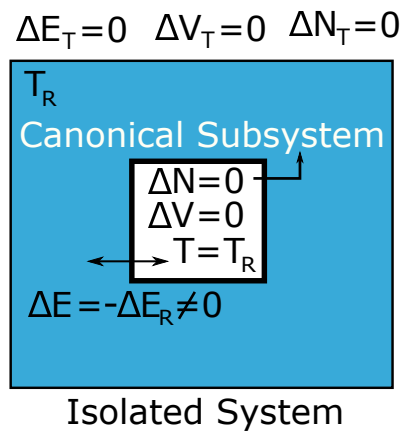

Figure 1.1: Schematic of the canonical system defined in the context of an isolated system decomposed into a reservoir and a canonical subsystem

Generally the most common thermodynamic ensembles are denoted by three letter abbreviations which specify the extensive parameters which are fixed by conservation laws and the intensive variable which are regulated by the reservoir. This is summarized in Tab. 1.1 for several common ensembles. The first column in the table is the name of the ensemble, the second column is the extensive variables which are fixed by conservation laws, the third column is the extensive properties which "flow" between the reservoir and the subsystem, the fourth column is the intensive properties which are regulated by the reservoir, and finally the fifth column is the common abbreviation for the ensemble.

Table 1.1: Abbreviations for common thermodynamic ensembles

Ensemble Name	Fixed extensive	Exchanged extensive	Regulated intensive	Abbreviation
micro-canonical	NVE	—	—	NVE
canonical	NV	E	T	NVT
grand-canonical	V	NE	μT	μVT
isothermal–isobaric	N	VE	pT	NPT
isoenthalpic-isobaric	H	NV	μp	NPH

1.3 Grain boundaries

A grain boundary is an internal interface separating homogeneous crystalline regions (grains) with different crystallographic orientations [117]. GBs are found in metallic materials, ceramics, and less conventional systems such as colloidal crystals [2], ice [124], solid helium [10, 108], graphene [59, 83] and organic crystals such as molecular semiconductors [111] and benzene [26]. The presence of GBs has a strong impact on a material's properties. These effects include changes in mechanical strength, thermal and electric conductivity, and the timescale associated with the onset of corrosion, just to name a few. Because of their practical importance GBs have been extensively studied by experiments [117] and simulations [94] over the past decades.

Crystallographically, a general GB has traditionally been characterized by five angles describing the lattice mis-orientation between the grains and the GB plane. Two commonly studied categories of GB are planar tilt [Fig. 1.2.(a)] and planar twist [Fig. 1.2.(b)] boundaries. These two categories are simplified cases of more realistic GBs which can be non-planar and have a mixed character exhibiting features from both categories. The tilt and twist GBs differ from one another with regard to how the grains are rotated relative to one another as demonstrated in Fig. 1.2. Some tilt GBs have mirror symmetry across their GB planes, GBs with this property are referred to as symmetrical tilt GBs. Finally in the present study we work exclusively with GBs in the face centered cubic (FCC) crystalline

system. In Fig. 1.2.(c) we show the conventional unit cell for this system and include the cubic Miller directions as well as an example of a crystallographic plane as a refresher of the Miller notation for the reader.

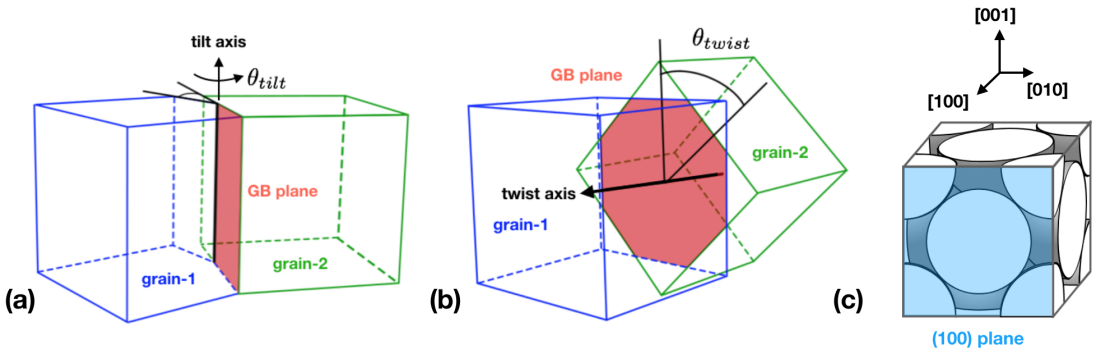

Figure 1.2: Schematic showing two common classes of grain boundaries (a) a tilt grain boundary (b) a twist grain boundary and (c) the conventional unit cell of the FCC crystal system with cubic Miller directions and an example of the (100) plane depicted (image source: [24, 25])

The various GBs analyzed in this work are all planar tilt GBs with a [001] tilt axis and a GB plane with the Miller indices $(hk0)$ where h, k are integers. For such boundaries the tilt angle is given by $\theta = 2tan^{-1}\left(\frac{k}{h}\right)$ which takes on values in the range $[0, 90^o]$. GBs are also often specified by a quantity known as the reciprocal density of coincident lattice sites which is denoted Σ. To understand the notation ΣX or $\Sigma = X$ consider the sub-lattice formed when the grains are rotated about the tilt axis and are allowed to fictitiously interpenetrate. In this interpenetrating lattice some lattice points from the two grains will coincide while other will not. The sub-lattice formed by the overlapping lattice points is used to characterize a given GB and is known as the coincident site lattice. The number Σ is the ratio of coincident to non-coincident sites, e.g. $\Sigma 17$ means that 1 cite in 17 belongs to both lattices. Thus $\Sigma X(hk0)[001]$ would be a complete description of a tilt GB of the form discussed here. For the boundaries in the present work the quantity Σ was obtained from

the relations $h^2 + k^2 = \Sigma$ or $h^2 + k^2 = 2\Sigma$ [17, 117]. Because we focus on boundaries with a fixed tilt axis and a relatively simple geometry we can refer to the various boundaries by the Miller indices of their respective GB planes, e.g. we can refer to the $\Sigma 5(210)[001]$ ($\theta = 53.1^o$) boundary simply as the (210) boundary. Even though we focus on FCC tilt GBs, the theories and methods described below could be extended to non-FCC systems and other types of GBs.

So far we have only discussed the crystallographic description of the GB however the local structure within a given GB core is also very important [46]. This is because different local atomic configurations can result in significantly different physical properties [31, 35, 37, 46]. Two of the chapters in this work focus on local GB structure and how it is effected by variations in density, temperature and chemical composition [53, 55]. In addition to the crystallographic description, a GB can also be described thermodynamically by its excess free energy γ. This quantity is generally a function of grain temperature and composition, however, for a single component system at $T = 0\,K$ it is expressed by the simple formula given in Eq.(1.4),

$$\gamma = \frac{E_{GB} - N\epsilon_G}{A}, \tag{1.4}$$

where E_{GB} is the total energy of a system of N atoms containing a planar GB of area A and ϵ_G is the per-atom energy of the bulk phase making up the grains.

1.4 Grain boundary pre-melting

A typical GB in a polycrystalline material has an atomically ordered structure at low temperatures but becomes increasingly disordered as temperature approaches the bulk melting point T_m [94, 117]. Very near T_m, many GBs develop liquid-like structures and become wider, often turning into a liquid film. The formation of equilibrium liquid-like GB structures near T_m is referred to as GB *premelting*. In alloys, this premelting effect can be fueled

by solute segregation and can occur at lower temperatures than in single-component systems. Premelting can drastically change GB properties, which in turn can impact properties of the material. The phenomenon of GB premelting is also relevant to grain coalescence during solidification of crystalline materials. As differently oriented crystallites growing from the melt merge together during late stages of solidification, they are separated by a layer of the liquid phase bounded by two solid-liquid interfaces. Depending on the nature of interactions between these interfaces, they can close the liquid gap and create a relatively ordered GB structure, or retain a thin (on the order of a nm) liquid layer, forming a premelted GB. Depending on this, the solidified material can exhibit significantly different properties. Despite many years of research, fundamental understanding of the GB premelting effect remains very incomplete.

Direct experimental information about GB premelting is very limited [4, 21, 50, 57, 80, 117]. Most experimental studies report indirect evidence based on unusual behavior of GB diffusion, mobility, sliding resistance, contact angles or other GB properties [21, 29, 48, 60, 86, 117, 127, 129]. The phenomenon has been studied by several computational approaches, such as molecular dynamics [11, 12, 23, 31, 49, 56, 62, 78, 81, 82, 100, 120] and Monte Carlo [8, 9, 130] simulations, phase-field modeling [77, 95, 121, 122, 128], and more recently by the phase field crystal method [1, 3, 7, 79, 91, 112, 116]. A number of possible premelting scenarios were found in the simulations. These ranged from continuous premelting as the temperature approached T_m from below to a thin-to-thick transition below T_m followed by abrupt melting of the entire material at some temperature above T_m. In this work we address the Cu-Ag system by systematic atomistic simulations. The work focuses on three different GBs in an attempt to probe the effect of grain misalignment and GB energy of alloy premelting.

1.5 Variation in local grain boundary density

As mentioned in Sec. 1.3, GBs are traditionally described by five crystallographic angles. These angles were previously assumed to fully define the GB structure and energy. It has recently been realized that variations in the local atomic density λ in the GB region can drastically alter the GB structure and cause transformations between different GB phases [36–38, 46, 89, 90, 106]. The variation in λ is achieved by either removing or adding atoms to the GB core. Some of the newly discovered GB structures behave like two-dimensional phases [21, 45], existing in certain temperature intervals and reversibly transforming to each other by first-order phase transformations. Such phases and transformations among them have been studied by atomistic simulations for two $\Sigma 5$ [001] symmetrical tilt GBs in Cu [37, 46]. In this work, we extend the previous studies of Cu $\Sigma 5$ GBs by computing the structures and energies of a large set of GBs over the entire angular range by allowing arbitrary variations in λ. The results confirm the existence of stable or metastable phases in all GBs studied here. We show that there are three types of structural unit that can describe all GB structures seen in the our study. This work demonstrates that λ should be added to the standard description of GBs as an extra thermodynamic parameter that helps predict the GB phases and transformations among them.

1.6 Canonical temperature fluctuations

Fluctuations of thermodynamic properties play an important role in phase transformations and many other physical phenomena and diverse applications. While fluctuations of energy E, volume V, number of particles N and other extensive parameters are well-understood, controversies remain in the literature regarding the nature, or even existence [63–65], of fluctuations of intensive parameters such as temperature, pressure, and chemical potentials. The question of temperature fluctuations in canonical systems has been the subject of discussions for over a century (see e.g. van Hemmen and Longtin [126] for a historical overview of the subject). A number of different views on temperature fluctuations can be

found in the literature, including the following:

1. Temperature fluctuations in canonical systems is a real physical phenomenon and can be measured experimentally [22] .

2. Temperature of a canonical system is *defined* as the temperature of the thermostat. Thus, $T \equiv T_0$ by definition and the very notion of temperature fluctuations is meaningless [63–65].

3. While fluctuations of the system energy E are well-defined, non-equilibrium temperature T is ill-defined [64, 126].

4. Even for an equilibrium *isolated* system, temperature is not a well-defined parameter. It can be evaluated by measuring the system energy and trying to estimate the temperature of the thermostat with which the system was in equilibrium before being disconnected [30, 84].

Recently, thermodynamics-based arguments for the viewpoint (1) have been put forward as part of a more general thermodynamic fluctuation theory [93]. The goal of the present work [54, 97] is to provide additional insights into the nature of temperature fluctuations by conducting molecular dynamics simulations of a quasi-harmonic crystalline solid.

Chapter 2: Methodology

2.1 Interatomic potentials

Generally the potential energy of a system with N atoms is given by the function $U(\boldsymbol{r}_1...\boldsymbol{r}_N)$ where $\boldsymbol{r}_1...\boldsymbol{r}_N$ is the position vectors of the atoms. This function is known as the potential energy surface (PES) and all classical methods rely heavily on some approximate representation of it. In practice a given approximation is simply referred to as an interatomic potential. In the literature there are many interatomic potential paradigms which represent $U(\boldsymbol{r}_1...\boldsymbol{r}_N)$ in different ways depending on the nature of the system's atomic interactions. Some popular examples of interatomic potential paradigms include the embedded atom method (EAM) potential [27], Tersoff potentials [123], angular dependent potentials (ADP) [98], charge-optimized many-body (COMB) potentials [73], and reactive force fields (REAX) [125]. The various paradigms have different strengths and weaknesses, for example, the EAM potential is computationally fast and particularly good at describing metallic systems whereas the Tersoff format is more commonly used for covalent systems such as Silicon or Germanium. In most paradigms the PES is approximated by a relatively simple collection of physically inspired functions which are "tuned" to properties of a particular material by adjusting a set of fitting parameters p_i ($i \approx 10 - 20$). These parameters are optimized by fitting to a small training set of experimental and first-principles DFT data. When an optimal fit of the data is obtained, the parameters are fixed once and for all and the potential parameterization is published for use by other researches. Therefore when an individual refers to a specific interatomic potential they are referring a particular parameterization made in the context of one of the various paradigms. For example there are many EAM potentials of varying qualities available for different elemental and multicomponent systems. The quality of the

potential depends on how carefully it was optimized during its development. The potentials used in this work, along with many others describing a wide range of materials, can be found at the National Institute for Standards and Technology (NIST) interatomic potential repository [6]. The choice of potential format and parameterization is very important because the accuracy of predictions made by MD or MC simulations is directly correlated with the quality of the potential being used. Depending on the potential, the predictions can range from being in very close agreement with experiment to results that have little or no connection with reality. For our analysis we exclusively utilize EAM type potentials. Furthermore to ensure that our results are realistic we work with potentials which are recognized by the atomistic community as being highly robust and accurate. Because we rely so heavily on the EAM formate we will provide a brief description of the method, see [99] for a more detailed discussion.

In the EAM format the total potential energy of the system is expressed as a sum over the individual atomic energies as given by Eq.(2.1)

$$U_{tot} = \sum_i U_i = \frac{1}{2}\sum_{ij} V(r_{ij}) + \sum_i F(\overline{\rho_i}). \tag{2.1}$$

In this expression the function $V(r_{ij})$ is a pair potential, r_{ij} is the distance between the ith and j^{th} atoms, $\overline{\rho_i}$ is the host electron density around atom-i, and $F(\overline{\rho})$ is known as the embedding function [99]. In this model the pair potential describes the interactions between bonded atoms. Textbook examples of pair potentials include the well known Lennard Jones potential and the Morse type potential [34]. In the EAM format the pair potential is typically more complicated containing combinations of different Morse functions. In a classical simulation there are no actual electrons present however their effect is accounted for in the EAM model by the second term in Eq.(2.1). This term gives the energy associated with inserting atom-i into the host electron density created by its neighbors. The host electron density at atom-i is calculated by summing over the atom's neighbors as shown in

Eq.(2.2)

$$\overline{\rho_i} = \sum_{j \neq i} \rho(r_{ij}). \tag{2.2}$$

In Eq.(2.2) the function $\rho(r)$ is the electron density function. This function is expressed as the sum of a repulsive exponential term and a gaussian type function. Finally the embedding function $F(\overline{\rho})$ is a polynomial and its exact form can be found in the literature [99].

2.2 The molecular dynamics Method

Molecular dynamics is a classical method for simulating the motion of a relatively large number of atoms or molecules ($N \approx 10^1$ to 10^7). It allows the user to simulate materials at any desired temperature or pressure and can produce results consistent with the thermodynamic ensembles mentioned in Sec. 1.2. From a classical point of view a system with N atoms is defined at any instance in time by a collection of position vectors $\boldsymbol{r}_i$ $(i = 1, 2, \ldots N)$ and velocity vectors $\boldsymbol{v}_i$ $(i = 1, 2, \ldots N)$. Assume that these atoms are treated as point particles and are confined to a box of volume V. As time progresses the $6N$ components making up $\boldsymbol{r}_i$ and $\boldsymbol{v}_i$ all vary with time [34]. A schematic showing a classical system at a fixed instant in time, i.e. a snapshot, is depicted in Fig. 2.1.

The atoms in the system may or may not interact with external world through the boundary. If the system is isolated then its total internal energy E is simply the sum of the various atom's kinetic and potential contributions. The kinetic term is easily calculated from the instantaneous velocity vectors ($K = \sum_i m \left|\boldsymbol{v}_i\right|^2 /2$). The potential term on the other hand is more complex and depends on how the particles in the system interact with one another as discussed in the pervious section. This classical description maps directly onto the scenario realized in an MD simulation where the vectors $\boldsymbol{r}_i$ and $\boldsymbol{v}_i$ are known at every time-step. Notice that many extensive thermodynamics variables are readily available from the simulation data including E, V and N. Furthermore many intensive parameters

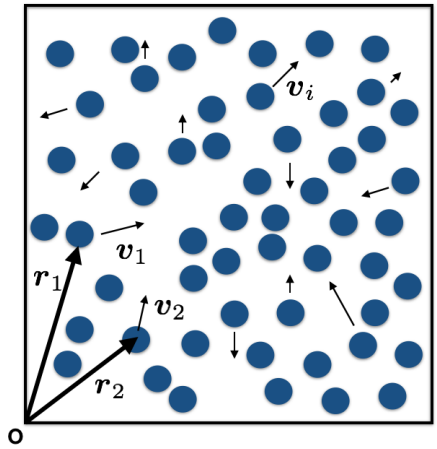

$$\boldsymbol{r}_i \;\; (i = 1, 2, \ldots N)$$
$$\boldsymbol{v}_i \;\; (i = 1, 2, \ldots N)$$
$$E = K + U$$
$$= \sum_i m \left|\boldsymbol{v}_i\right|^2 / 2 + U(\boldsymbol{r}_1 \ldots \boldsymbol{r}_N)$$

Figure 2.1: Schematic example of a classical atomic system

can be obtained from the knowledge of $\boldsymbol{r}_i$ and $\boldsymbol{v}_i$, for example, the time average temperature can be obtained using the equipartition theorem as

$$\langle T \rangle = \frac{2 \langle K \rangle}{3Nk} = \frac{1}{3Nk} \left\langle \sum_i m \left|\boldsymbol{v}_i\right|^2 \right\rangle$$

where k is the Boltzmann constant. Additionally in the case of a simple fluid the pressure can be calculated from the ideal gas law. For a solid state systems there are more complicated expressions to calculate the stress tensor however the idea is similar [34]. There are several software package available for carrying out MD simulations however for the present work we utilize the molecular dynamics package LAMMPS (Large-scale Atomic/Molecular Massively Parallel Simulator) developed at Sandia National Lab [107]. One drawback of MD is that there is no way to vary the system's chemical composition throughout the simulation. This makes modeling chemical equilibration via MD impractical.

2.2.1 NVE molecular dynamics

For simplicity we will discuss the MD algorithm in the context of the NVE ensemble; however, the ideas extend to simulating the other ensembles. The basic premise behind the MD algorithm is that the forces felt by a given atom can be calculated based on its position relative to the other atoms using Eq.(2.3)

$$\boldsymbol{F}_i = -\frac{\partial U(\boldsymbol{r}_1 ... \boldsymbol{r}_N)}{\partial \boldsymbol{r}_i}. \tag{2.3}$$

From this force, the acceleration on that atom can be calculated using Newton's law. Using the atom's current velocity and acceleration one can predict the future position after some time-step Δt ($\approx 10^{-12}$ sec) using the Verlet algorithm (see [34]). There are also many details concerning how boundary conditions are enforced as well as techniques to improve computational efficiency, these however will not be addressed here. For simplicity, we just provide the general outline of the algorithm [34].

1. First the positions and velocities of the N atom are initialized. For the atomic locations it is best to choose positions as close to equilibrium as possible. For solids this can be obtained from knowledge of the material's crystal structure, lattice constant and thermal expansion behavior. The velocities can then be initialized by sampling the Maxwell-Boltzmann velocity distribution.

2. Loop through time

   - At each time step the code loops over all atoms, for each atom ($\mathbf{r}_i$) in this loop a second loop over all other atoms ($\mathbf{r}_j$) is carried out which calculates the distances (r_{ij}) between atom i and all other atoms. From the distances the force on $\mathbf{r}_i$ can be computed. Once both loops are finished the forces on all atoms are know at that time-step, from this the position and velocities of all atoms can be calculated

at the next time-step. The process is then repeated at successive time-steps for as long as is necessary.

2.2.2 NVT molecular dynamics

We will also discuss the MD algorithm in the context of the NVT ensemble because this ensemble is the central focus of the fifth chapter of this work. There are multiple ways to mimic a heat reservoir in MD. These methods typically add additional artificial forces to the atoms in such a way that the collective motion of the atoms is consistent with a canonical system with an average temperature $\langle T \rangle$. One method commonly used to achieve this is known as the Langevin thermostat [34]. In this algorithm the atoms are treated as though they are immersed in a sea of much smaller fictitious particles which have a fixed temperature T. These fictitious particles exert a drag force as well as a stochastic noise force $\boldsymbol{R}$ that constantly perturbs the actual atoms in the simulation. Using this method the total force on atom i, with mass m_i is

$$\boldsymbol{F}_i = -\frac{\partial U(\boldsymbol{r}_1 ... \boldsymbol{r}_N)}{\partial \boldsymbol{r}_i} - m_i \gamma \boldsymbol{v}_i + \boldsymbol{R}_i. \tag{2.4}$$

The drag term depends on the damping constant γ, the inverse of which controls the timescale τ_r of the energy exchanges between the system and the thermostat. During the simulation, the noise $\boldsymbol{R}_i$ is randomly sampled from a normal or uniform distribution at time intervals much shorter than $\tau_r = 1/\gamma$. The variance of the noise defines the thermostat temperature T_0 via the standard fluctuation-dissipation relation [34].

2.3 The Monte Carlo method

To begin our discussion of the MC method we will discuss it in the context of simulating atomic motion at a fixed temperature. In this context the temperature is an input parameter which controls the extent to which the atoms are allowed to deviate via thermal fluctuations away from their equilibrium positions. When modeling motion the MC and MD

methods produce similar results however their implementation is very different. The first notable difference is that the MC procedure doesn't have any concept of time inherent in the method. It is instead an iterative statistical procedure where the system progresses forward by randomly displacing atoms and determining whether the new location is energetically favorable. To determine if a position is favorable the method utilizes the Boltzmann factor $exp(-\frac{U(\boldsymbol{r}_1...\boldsymbol{r}_N)}{kT})$ from statistical mechanics [34]. To be more specific on how MC models motion, we give a brief outline of the Metropolis algorithm which can be summarized as follows:

- Select a particle with location $\boldsymbol{r}_i$ and calculate the current energy $U = U(\boldsymbol{r}_1...\boldsymbol{r}_N)$.
- randomly displace the atoms by some amount $\Delta\boldsymbol{r}_i$ and recompute the energy $U' = U(\boldsymbol{r}_1 \ldots \boldsymbol{r}_i + \Delta\boldsymbol{r}_i...\boldsymbol{r}_N)$
- Accept the move with the probably $min(1, exp(-\frac{U'}{kT})/exp(-\frac{U}{kT}))$

This algorithm is looped over all atoms, which constitutes one "MC step". The process is repeated as many times as is needed to meet the user's needs. Using MC in this way effectively reproduces the NVT ensemble discussed above.

One of the most important advantages of the MC method is that it can also be used to vary the chemical composition of the simulation block. This is done by artificially switching the chemical species of a given atom and deciding whether to keep the chemical swap based on the resultant energy difference. In this way the code can model a thermodynamically open system and establish chemical equilibrium which, as previously mentioned, is not possible using MD [34]. The exact details of how compositionally variable MC is implemented will be discussed in chapter-3 which is the only section of the thesis which utilizes this method.

Chapter 3: Grain boundary premelting

The simplest and most productive model of GB premelting is one that represents the GB by a uniform liquid layer between two solid-liquid interfaces interacting by a thermodynamic potential $\Psi(w)$ depending on the GB width w [74, 75]. This model [74] and it's subsequent detailed analysis [33, 75] were transferred from the theory of wetting of substrates by thin liquid films, in which the wetting behavior depends on the interaction potential between the two interfaces. This model is capable of predicting a number of GB premelting scenarios, depending on the form of the interaction potential. In this work we refer to this model as the "liquid layer model" of GB premelting.[1] In addition to simplicity, the advantage of this model is that it puts the GB premelting effect in the context of phase transitions theory and critical phenomena [33, 105].

The focus of this work is on GB premelting in binary alloys. This case is more complex and less studied than premelting in single-component systems. Rappaz et al. [110] performed multiphase-field simulations of a binary alloy system in the context of late-stage solidification. The emergence of "dry" or "wet" GBs observed in their simulations was explained by different solid-liquid interaction potentials $\Psi(w)$. The latter were modeled by exponential functions $\Psi(w) = C\exp(-w/\delta)$, which could be made repulsive or attractive by choosing the sign of C. Rappaz et al. [110] related their solid-liquid interaction potential to the disjoining effect known from the field of thin liquid films. Following their paper, the interaction potential $\Psi(w)$ employed in GB premelting models came to be called the "disjoining potential". Tang et al. [122] developed a phase-field model of GB premelting in binary systems and analyzed possible premelting behaviors in an abstract eutectic system

[1] Rappaz et al. [110] refer to this model as the "sharp interface model" since the solid-liquid interfaces are treated as sharp. We find this term somewhat ambiguous since it might suggest that the entire GB is treated as a sharp interface as it is done in many other theories. The term "liquid layer model" avoids this potential confusion and, we believe, better represents the main idea.

A–B. GB premelting was also studied [95] by a multiphase-field method with realistic model parameters reproducing the eutectic Cu-Ag system. This study revealed that the disjoining potential can have a variety of shapes intermediate between purely repulsive and purely attractive. The simulations have demonstrated that, under certain conditions, first-order thin-to-thick GB phase transitions can occur near the solidus line. Such transitions can be represented by a transition line on the Cu-Ag phase diagram starting at a GB prewetting point and ending at a critical point near the melting point of pure Cu. A similar multiphase-field model was analyzed by Wang et al. [128], who additionally developed an analytical approach to calculations of interaction forces between solid-liquid interfaces. Although their work was primarily focused on a single-component system, they did consider the case of a dilute binary alloy and were able to reproduce the thin-to-thick transition. On the other hand, Rowan [112] performed phase field crystal simulations of GB premelting in binary alloys and did not see such transitions. The disjoining potentials extracted from her simulations were either purely repulsive or purely attractive.

As far as atomistic simulations are concerned, the MD timescale is too short to reach chemical equilibrium with today's computer capabilities. Consequently, MC remains the only feasible approach to simulate binary systems [94]. Williams et al. [130] applied the semi-grand canonical MC method with an embedded atom potential to study premelting in a high-energy $\Sigma 5$ GB in Cu–Ag alloys. It was found that Ag segregation strongly favors GB premelting, which commences at temperatures significantly lower than in pure Cu. As the chemical composition of the grains approached the solidus line from below, the boundary developed a relatively thick layer of the liquid solution whose composition approached the liquidus composition on the phase diagram. Because of the statistical scatter of the data, it was not possible in that work to detect thin-to-thick transitions or extract the disjoining potential.

In this work we revisit the Cu-Ag system [130] by more accurate and systematic atomistic simulations. Three different GBs are included in order to probe the effect of GB energy. The disjoining potential has been calculated for all three boundaries by analyzing their width

fluctuations. Depending on the chemical composition, the boundaries exhibit repulsive, attractive or intermediate cases of the disjoining potential. An analytical form of disjoining potential is proposed that describes all these cases. Among a number of different premelting scenarios predicted by this potential, the simulations do reveal the thin-to-thick transition that has not been reported in atomistic simulations previously.

In Sec. 3.1 of the chapter, we discuss different forms of disjoining potentials and propose a new analytical form. We also derive expressions for the equilibrium disjoining pressure near a solidus line, which is one of the ingredients of the liquid layer model. To enable calculations of the disjoining potential from simulation data, we present an equation relating the disjoining potential to equilibrium fluctuations of the GB width in a binary system. After describing our simulation methodology in Sec. 3.2, we report the results for GB premelting in pure Cu (Sec. 3.3.1) and Cu-Ag alloys (Sec. 3.3.2). For completeness, we also apply the thermodynamic integration method to compute GB free energies as functions of temperature and/or grain composition. Extrapolation of the computed free energies to the premelting region allows us to validate the disjoining potential calculations and, by extension, the liquid-layer model itself. In Sec. 3.4 we summarize our findings and draw conclusions.

3.1 Theory

3.1.1 The liquid layer model of grain boundary premelting

Consider a chemically closed binary system containing a liquid layer between two solid regions (Fig. 3.1). The cross-section of the system is fixed once and for all. We will assume that the system always remains in thermal equilibrium with a thermostat at a given temperature T.

Calculations that do not take thermal equilibrium for granted and solve the problem in terms of energy and entropy can be found in Ref. Mishin:2015ab. The present derivation is simpler and adapted to the context of atomistic simulations reported later in the chapter.

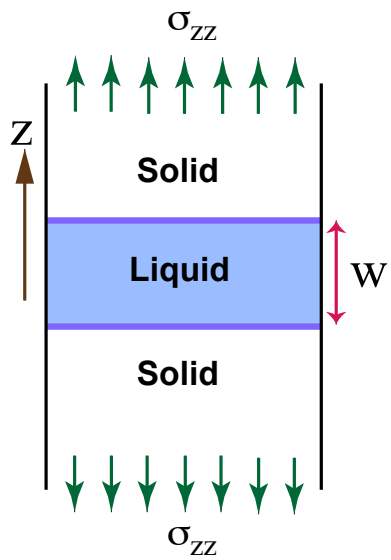

Figure 3.1: Premelted GB subject to a normal stress σ_{zz}. The GB region is modeled by a uniform liquid layer of width w bounded by interacting solid-liquid interfaces.

Before discussing the solid-liquid equilibrium, we need to specify thermodynamic properties of the bulk phases. The solid (S) and liquid (L) phases are described by the equations of state

$$F_L(T, N_L, N_{2L}, V_L), \tag{3.1}$$

$$F_S(T, N_S, N_{2S}, V_S), \tag{3.2}$$

where F is Helmholtz free energy, N total number of atoms in the phase, N_2 the number of solute atoms (component 2), and V is volume. The derivatives of the free energy are $\partial F_L/\partial N_L = \varphi_L$, $\partial F_S/\partial N_S = \varphi_S$, $\partial F_L/\partial N_{2L} = \mu_2 - \mu_1 \equiv \Delta\mu$, $\partial F_S/\partial N_{2S} = M$, $\partial F_L/\partial V_L = -p_L$, $\partial F_S/\partial V_S = \sigma_{zz}$, where μ_1 and μ_2 are the chemical potentials in the liquid phase, M is the diffusion potential [71] of the solute relative to the solvent in the solid phase, p_L is pressure in the liquid, and σ_{zz} is the stress component normal to the interfaces. The functions φ_L and φ_S are thermodynamic potentials of the phases (per atom) that will be used below.

Applying the Euler theorem to the homogeneous first degree functions (3.1) and (3.2), we obtain

$$F_L - (\Delta\mu)N_{2L} + p_L V_L = N_L \varphi_L,$$

$$F_S - MN_{2S} - \sigma_{zz} V_S = N_S \varphi_S.$$

The left-hand sides are Legendre transforms of the free energy with respect to N_2 and V. Accordingly, φ_L and φ_S are functions of the variables conjugate to N_2 and V:

$$\varphi_L = \varphi_L(T, \Delta\mu, p_L),$$

$$\varphi_S = \varphi_S(T, M, \sigma_{zz}),$$

with the derivatives $\partial\varphi_L/\partial\Delta\mu = -c_L$, $\partial\varphi_S/\partial M = -c_S$, $\partial\varphi_L/\partial p_L = v_L$ and $\partial\varphi_S/\partial\sigma_{zz} = -v_S$, where $c_L = N_{2L}/N_L$ and $c_S = N_{2S}/N_S$ are solute concentrations (atomic fractions) in the phases and v_L and v_S are the respective atomic volumes. Note that each phase is specified by three independent variables (three degrees of freedom).

The equations of thermodynamic equilibrium between the phases are obtained from the condition $\delta F_L + \delta F_S = 0$ under the constraints of fixed volume and fixed number of atoms of each component. This gives

$$p_L^* = -\sigma_{zz}, \tag{3.3}$$

$$\Delta\mu^* = M^*, \tag{3.4}$$

$$\varphi_L(T, M^*, -\sigma_{zz}) = \varphi_S(T, M^*, \sigma_{zz}). \tag{3.5}$$

Here and everywhere below, the asterisk marks properties related to thermodynamic equilibrium between the bulk phases. Equation (3.3) is the condition of mechanical equilibrium while Eqs.(3.4) and (3.5) are the conditions of chemical equilibrium and equilibrium with respect to the phase transformation, respectively. T and σ_{zz} play the role of control parameters. For each pair (T, σ_{zz}), Eqs.(3.3)-(3.5) can be solved for M^*, $\Delta\mu^*$ and p_L^*. Knowing

these, $c_L^* = -(\partial\varphi_L/\partial\Delta\mu)_*$ and $c_S^* = -(\partial\varphi_S/\partial M)_*$ give the equilibrium chemical compositions of the phases. These compositions define two points on the solidus and liquidus lines of the equilibrium phase diagram.

Next, we consider a solid-liquid interface between the equilibrium phases. Following Gibbs' interface thermodynamics, we choose a geometric dividing surface inside the interface region. Suppose the precise position of this surface is adjusted so that the Gibbsian excess of the total number of atoms relative to this surface be zero: $\tilde{N} = 0$. We will use tilde to indicate excess quantities relative to this choice of the dividing surface. Generally, the free energy γ_{SL} (reversible work of formation) of a solid-liquid interface is the excess of the potential [39]

$$\Phi = F + pV - \mu_1 N - MN_2. \tag{3.6}$$

In the present case we obtain[2]

$$\gamma_{SL} A = \tilde{F} - M^* \tilde{N}_2 \tag{3.7}$$

since the terms with $\tilde{N}$ and $\tilde{V}$ vanish. Note that γ_{SL} is defined only in the state of phase equilibrium and is a function of two independent variables, e.g., T and σ_{zz}.

Now return to the liquid layer embedded between two grains (Fig. 3.1). Suppose the layer is so thin that the inhomogeneous regions of the solid-liquid interfaces overlap. Thus, the liquid layer is no longer homogeneous. In the model discussed here, the liquid is still treated as homogeneous and the solid-liquid interfaces are attributed the same properties as those of an isolated interface at the given T and σ_{zz}. The difference between this idealized picture and the real system is accounted for by introducing a coupling between the two interfaces called the disjoining interaction. The position of each interface is defined by the dividing surface for which $\tilde{N} = 0$. This choice of dividing surfaces ensures that, as the distance w between them increases, we eventually obtain two non-interacting interfaces discussed in the previous paragraph. In this limit, the liquid layer model becomes exact.

[2]In a more general treatment [39], γ_{SL} is expressed in terms of generalized excesses introduced by Cahn.[15] In this work, it will suffice to use one particular type of excess, namely $[X]_{NV}$, where X is any extensive property. To simplify the notations we denote this excess $\tilde{X}$.

According to this model, the free energy of the system is

$$F = F_L(T, N_L, N_{2L}, V_L) + F_S(T, N_S, N_{2S}, V_S) + 2\tilde{f}(T, \sigma_{zz})A + \Psi(T, \sigma_{zz}, w)A.$$

Here, F_L and F_S are the free energies of the phases computed assuming that they remain homogeneous all the way to the dividing surfaces, $\tilde{f}$ is the excess free energy (per unit area) at each interface, and Ψ is called the disjoining potential. Note that, due to our choice of the dividing surfaces, the total number of atoms in the system is $N = N_L + N_S$. Similarly, the Φ-potential of the system is

$$\Phi = \varphi_L N_L + \varphi_S N_S - \mu_1(N_L + N_S) + 2\gamma_{SL}A + [\Psi - (\partial\Psi/\partial w)w]A. \tag{3.8}$$

The derivative

$$p_d = \frac{\partial \Psi}{\partial w} \tag{3.9}$$

is called the disjoining pressure. By definition, $\Psi \to 0$ and $p_d \to 0$ at $w \to \infty$.

It is easy to derive the conditions of thermodynamic equilibrium in this system from the requirement that $\delta F = 0$ under the constraints $\delta N_L + \delta N_S = 0$, $\delta N_{2L} + \delta N_{2S} = 0$, $\delta V_L + \delta V_S = 0$ and $\delta V_L = A\delta w$. Eliminating these constraints,

$$\delta F = (\varphi_L - \varphi_S)\delta N_L + (\Delta\mu - M)\delta N_{2L} + (p_d - p_L - \sigma_{zz})\delta V_L = 0$$

with three independent variations δN_L, δN_{2L} and δV_L. The equilibrium conditions become

$$p_d = p_L + \sigma_{zz}, \tag{3.10}$$

$$\Delta\mu = M, \tag{3.11}$$

$$\varphi_L(T, M, p_d - \sigma_{zz}) = \varphi_S(T, M, \sigma_{zz}). \tag{3.12}$$

Equation (3.10) shows that the liquid layer is subject to the disjoining pressure p_d in addition to the pressure $-\sigma_{zz}$ exerted by the solid. For each set of control parameters (T, M, σ_{zz}) defining the state of the solid, Eqs.(3.10)-(3.12) can be solved for the liquid properties $\Delta\mu$, p_L and p_d. The equilibrium width w is then the found from Eq.(3.9). The equilibrium compositions of the phases can be calculated from the relations $\partial\varphi_L/\partial\Delta\mu = -c_L$ and $\partial\varphi_S/\partial M = -c_S$.

3.1.2 Disjoining potential near the solidus line

If the liquid layer is thin, the phase compositions are different from the liquidus and solidus compositions at the same T and σ_{zz}. They only approach c_L^* and c_S^* if the liquid layer is thick enough to neglect the disjoining effect. Suppose T and σ_{zz} are fixed and M approaches M^*. The disjoining pressure is small and, to the leading order, is expected to be proportional to the undersaturation $\Delta M \equiv M - M^*$. Indeed, linearizing equation (3.12) with respect to the small parameters ΔM and p_d we obtain

$$\varphi_L(T, M^*, -\sigma_{zz}) - c_L^*\Delta M + v_L^* p_d = \varphi_S(T, M^*, \sigma_{zz}) - c_S^*\Delta M.$$

The zeroth order terms cancel by Eq.(3.5) and we arrive at the equation relating the disjoining pressure to ΔM:

$$p_d = \frac{c_L^* - c_S^*}{v_L^*}\Delta M. \tag{3.13}$$

Similarly, for a single-component system close to the bulk melting point T_m, p_d is small and is expected to be proportional to the undercooling $\Delta T \equiv T - T_m$. In this case, the phase equilibrium conditions at and below T_m are, respectively,

$$\varphi_L(T_m, -\sigma_{zz}) = \varphi_S(T_m, \sigma_{zz}) \tag{3.14}$$

and

$$\varphi_L(T, p_d - \sigma_{zz}) = \varphi_S(T, \sigma_{zz}). \tag{3.15}$$

Linearizing Eq.(3.15) with respect to ΔT and p_d and using Eq.(3.14) we obtain

$$p_d = \frac{H_m}{v_L^* T_m} \Delta T, \tag{3.16}$$

where $H_m = (s_L^* - s_S^*)T_m$ is the heat of melting per atom, s_L^* and s_S^* being the entropies of the equilibrium phases per atom.

3.1.3 Fluctuations of grain boundary width

We now return to the liquid layer model of GB premelting. The equilibrium GB free energy γ is the excess of the Φ-potential given by Eq.(3.8). Thus,

$$\gamma_0 = 2\gamma_{SL} + \Psi(w_0) - p_d^0 w_0, \tag{3.17}$$

where index 0 is a reminder that the relevant quantities are computed in the state of equilibrium described by Eqs.(3.10)-(3.12).

We should also consider the non-equilibrium GB free energy

$$\hat{\gamma}(w) = 2\gamma_{SL} + \Psi(w) - p_d^0 w. \tag{3.18}$$

For brevity, we have suppressed T and σ_{zz} as parameters of the disjoining potential and of p_d^0. This free energy is obtained by allowing the GB width to vary while keeping the phases in the same equilibrium state. The equilibrium GB free energy $\gamma = \hat{\gamma}(w_0)$ can be found by minimizing $\hat{\gamma}$ with respect to w.

A premelted GB fluctuates around its equilibrium state. To describe fluctuations of the GB width w, we consider only fluctuations of the disjoining interaction while treating all other thermodynamic parameters as properties of a large reservoir. Using the generalized

canonical distribution [93], the probability of finding w in an interval dw is

$$P(w)dw = P_m \exp\left[-A\frac{\Psi(w) - \Psi(w_0) - \left(\frac{\partial\Psi}{\partial w}\right)_0 (w - w_0)}{k_B T}\right] dw, \tag{3.19}$$

where k_B is Boltzmann's constant and P_m is the maximum value of the probability density $P(w)$. According to this equation, w_0 is the most probable value of the GB width, i.e., the position of the peak of $P(w)$. Equation (3.19) can be rewritten in the form

$$P(w) = C \exp\left(-A\frac{\Psi(w) - p_d^0 w}{k_B T}\right), \tag{3.20}$$

where the pre-exponential coefficient C can be found from the normalization condition $\int_0^\infty P(w)dw = 1$. A similar equation was employed in previous studies of single-component systems [1, 31, 56]. Here, it has been extended to a binary system. Recall that for a binary system, p_d^0 is given by Eq.(3.13).

Equation (3.20) is the main equation used for the calculation of disjoining potentials from GB width fluctuations. It can be written in the alternative form [1, 31, 56]

$$P(w) = C' \exp\left(-\frac{\hat{\gamma}(w)A}{k_B T}\right), \tag{3.21}$$

where C' is a normalization factor.

3.1.4 Types of disjoining potentials

Two categories of disjoining potentials have been discussed in the literature: repulsive and attractive [1, 31, 56, 77, 112, 116, 128] [Fig. 3.2(a)].

For metallic systems, both the repulsive and attractive interactions are short-range and

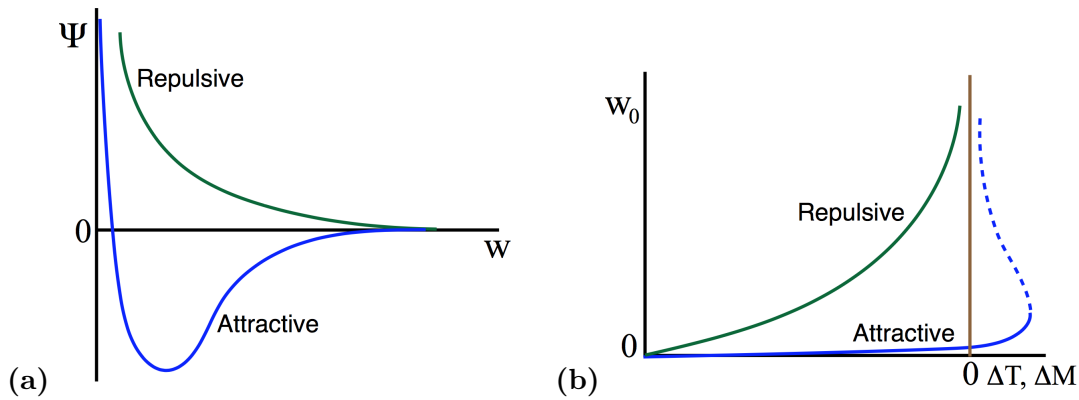

Figure 3.2: Traditional classification of disjoining potentials into repulsive and attractive. (a) Potential shapes. (b) Equilibrium GB width as a function of undercooling ΔT or undersaturation ΔM for the two types of potentials. The vertical line marks the equilibrium melting point (respectively, solidus line). The dashed curve represents unstable GB states.

have a structural character: the attraction is due to the overlap of density perturbations near the solid-liquid interfaces and the repulsion arises from the orientation mismatch of the merging crystal lattices [1, 31, 56, 116, 128]. The repulsion and attraction are usually modeled by exponential functions. Both the repulsion and attraction can be described by a single functional form [112, 128]

$$\Psi(w) = C_1 e^{-w/\delta_1} - C_2 e^{-w/\delta_2}, \tag{3.22}$$

where the four coefficients C_1, C_2, δ_1 and δ_2 depend on the thermodynamic state of the grains. This functional form predicts two premelting scenarios: either continuous premelting with a logarithmic divergence of the GB width at the melting point (or solidus line), or a relatively narrow boundary that can be overheated above the melting point (respectively, oversaturated above the solidus line) until an instability point at which it abruptly melts [Fig. 3.2(b)].

A limitation of Eq.(3.22) is that it does not predict the thin-to-thick premelting transitions that were observed in phase field simulations [95, 128] and the atomistic study

described later in this chapter. It was suggested [95] that such transitions require a non-exponential potential. Namely, that the potential shape have a concave region between two convex regions [Fig. 3.3(a)], so that a common tangent could be constructed with two different touching points.

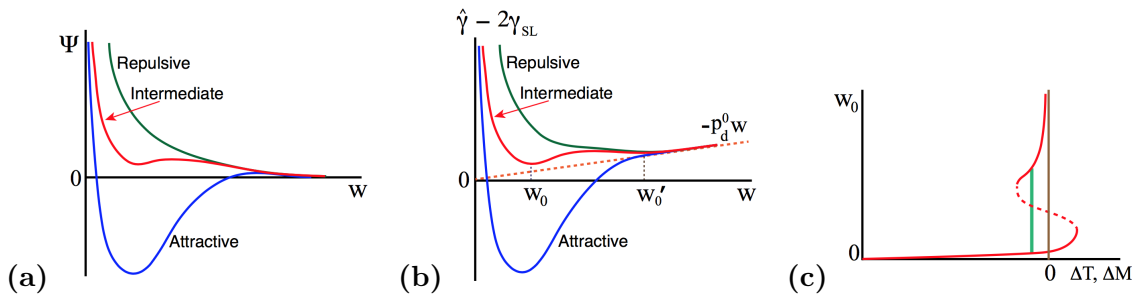

Figure 3.3: Disjoining potentials proposed in this work: repulsive, attractive and intermediate. (a) Potential shapes. Note that the attractive and intermediate potentials have a shallow maximum in the tail region. (b) Non-equilibrium GB free energy $\hat{\gamma}$ relative to $2\gamma_{SL}$ as a function of GB width for the three potential types. The red dashed line represents the term $-p_d^0 w$. The minima of $\hat{\gamma}$ correspond to equilibrium GB states. Note that the intermediate potential creates two local minima corresponding to GB states with widths w_0 and w_0'. (c) Equilibrium GB width as a function of undercooling ΔT or undersaturation ΔM for the intermediate disjoining potential. The green vertical line shows the thin-to-thick transition in the GB. The long vertical line marks the equilibrium melting point (respectively, solidus line). The dashed curve represents unstable GB states.

We call this type of a disjoining potential *intermediate*. The plot of $\hat{\gamma}$ versus w can then have two local minima giving rise to stable and metastable states of the boundary [Fig. 3.3(b)]. At an appropriate undercooling (undersaturation), the minima have an equal depth. This situation corresponds to equilibrium between two GB phases and is the point of a thin-to-thick transition [Fig. 3.3(c)]. Above this point, the GB width continues to increase and eventually diverges at the melting point (respectively, solidus line). In a binary system, such transitions can be represented by a thin/thick coexistence line below the solidus line on the equilibrium phase diagram [95].

As the state of the grains varies, the disjoining potential can evolve from repulsive to intermediate to attractive. To describe this evolution, it is desirable to have a single

analytical form of $\Psi(w)$ that describes all three cases, depending on the choice of the parameters. In this work we propose the following functional form:

$$\Psi(w) = c_1 e^{-c_2 w} - c_3 e^{-c_4 w} \sin(c_5 w + c_6), \tag{3.23}$$

with six coefficients c_i. This form is a generalization of Eq.(3.22) and can be shown to capture all three cases. The first term describes exponential repulsion at small w. The sine in the second (attractive) term creates the intermediate shape mentioned above that leads to the thin-to-thick transition.

An additional effect captured by Eq.(3.23) is the presence of damped oscillations in the tail part of the disjoining potential. The incorporation of such oscillations is motivated by the existence of composition patterning near solid-liquid interfaces. Compositional oscillations in the liquid phase near solid-liquid interfaces were found in several alloy systems in both experiments [5, 61, 102] and simulations [39, 51, 52, 88]. This effect was also found in the present work as illustrated in Fig. 3.4.

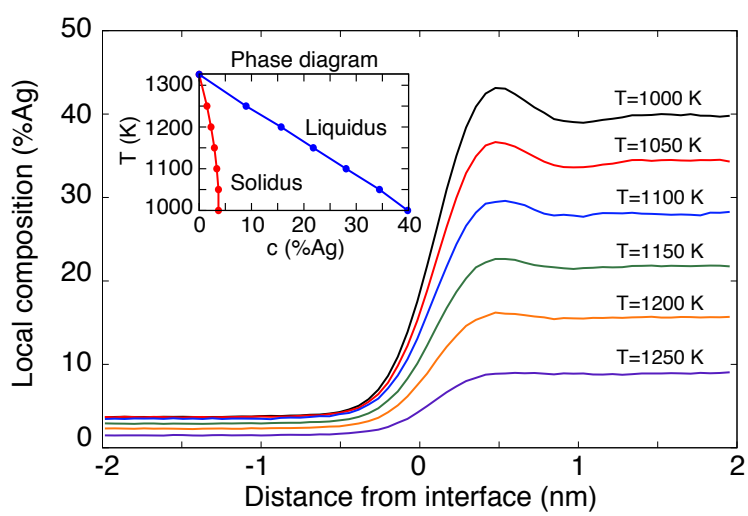

Figure 3.4: Chemical composition profiles across the (210) solid-liquid interface in the Cu-Ag system at several temperatures. The interface position was determined from the order parameter profile as explained in the text. The inset shows the relevant portion of the phase diagram with the solid and liquid compositions marked by the points.

The methodology of the simulations shown in this figure will be explained later. At this point, it is important to notice the compositional oscillations in the liquid near the solid-liquid interface. The peak of Ag concentration closest to the interface, which we call the principal peak, is followed by a set of local minima and maxima with fast decreasing amplitude until the composition levels out at c_L^*.

Similar compositional oscillations were found near the (110) oriented interface in the same system [39], pointing to the generality of the effect. In fact, simulations show that any static perturbation of chemical composition in this system produces a relaxation zone with oscillatory behavior of the chemical composition. For example, compositional oscillations were observed under an open surface of Cu-Ag melt [39]: underneath the topmost layer enriched in Ag relative to the bulk, there is a layer depleted in Ag, followed by a layer slightly enriched in Ag, and so on until the composition become practically uniform deeper in the bulk. In a premelted GB, the solid-liquid interfaces create a superposition of such compositional oscillations in a manner similar to wave interference. Since it is this overlap that gives rise to the disjoining attraction, we expect that the disjoining potential may display rapidly decaying oscillations in the tail region. The concave region mentioned above, and thus the thin-to-thick transition, are associated with the overlap of depletion zones. In principle, the higher-order peaks may create an entire cascade of additional thin-to-thick transitions closer to the solidus line. The situation is similar to the layering transitions [105] in surface adsorption and would give rise to a set of tightly spaced transition lines on the phase diagram, each ending at a critical point.

3.2 Methodology of simulations

3.2.1 Simulation of bulk phases

Atomic interactions in the Cu-Ag system were described by the embedded-atom method (EAM) [27] potential [131] that accurately predicts a large number of properties of Cu and Ag and was fitted to a first-principles database of Cu-Ag compounds. The potential

reproduces the Cu-Ag phase diagram in reasonable agreement with experiment (Fig. 3.5).

Although MD was the main simulation method in the previous GB premelting studies in pure metals [31, 56], this method is not well suited for alloy systems. As mentioned above, the accessible MD simulation times are too short to achieve chemical equilibrium of the premelted GB structure by atomic diffusion through the solid solution. Hence, MC simulations were chosen as the main simulation method, as was done in the previous work [131]. For consistency of methodology, MC was also used in premelting simulations of pure Cu, even though MD could have been applied. We utilized the parallel MC code developed by V. Yamakov at NASA [58, 109, 132]. Two MC modes were implemented in this work: the semi-grand canonical ensemble and the composition-controlled algorithm.

In semi-grand canonical MC simulations [34, 69], the temperature T and the diffusion potentials M of Ag relative to Cu are fixed while the chemical composition is allowed to vary. In this work, the chemical composition was measured as a fraction of Ag atoms. Depending on the goal of the simulation, some or all of the system dimensions were allowed to vary. The trial moves of the MC process included displacements of randomly selected atoms by a small random amount in a random direction with simultaneous random re-assignment of the chemical species of the chosen atom to either Cu or Ag. The number of trial moves equal to the number of atoms in the system constitutes one MC step. After each MC step, the dimensions of the simulation block in all or some of the x, y and z directions were altered by random amounts with appropriate re-scaling of atomic coordinates. Such fluctuations of the system dimensions ensure zero normal stresses σ_{ii} in the respective directions ($i = x, y, z$). The trial moves were accepted or rejected by the Metropolis algorithm [34, 69]. Namely, a move was accepted with the probability $\exp(-\Omega/k_B T)$ if $\Omega > 0$ and unconditionally if $\Omega \leq 0$, where [13, 14, 92]

$$\Omega \equiv \Delta E \pm M \pm \frac{3}{2} k_B T \ln \frac{m_{\mathrm{Cu}}}{m_{\mathrm{Ag}}}. \tag{3.24}$$

Here, m_{Cu} and m_{Ag} are atomic masses of Cu and Ag and ΔE is the energy change due to the trial move. The positive sign applies when Cu is replaced by Ag and negative when Ag

is replaced by Cu. The logarithmic term with atomic masses comes from the integration of the state probability over the linear momenta of atoms, giving a pre-exponential factor proportional to the product of masses of all atoms to the power of 3/2. In the probability ratio of two atomic configurations, all masses cancel out except for the masses of the atom whose species changes, giving rise to the pre-exponential factor of either $(m_{\mathrm{Cu}}/m_{\mathrm{Ag}})^{3/2}$ or $(m_{\mathrm{Ag}}/m_{\mathrm{Cu}})^{3/2}$. The MC simulations bring the system to thermodynamic equilibrium under the imposed boundary conditions. Since the redistribution of chemical species is implemented by an artificial procedure that does not require diffusion, chemical equilibrium is achieved much faster than in MD. Once equilibrium is reached, a long MC run was implemented to compute expectation values of thermodynamic properties in the given statistical ensemble. In the case of pure Cu, the canonical ensemble was implemented, which included all of the foregoing steps except that the chemical species of the atoms remained unaltered.

The composition-controlled MC simulations [92, 109, 132] impose a desired average chemical composition c of the simulation block and let the system adjust the diffusion potential M to achieve this composition. To reach the preset composition c, a feedback loop is created between the current value of c and the imposed diffusion potential M according to the iteration scheme

$$M^{(n)} = M^{(n-1)} - a\left(\frac{c^{(n-1)} + c^{(n-2)}}{2} - c\right), \tag{3.25}$$

where index n labels MC steps and a is an adjustable parameter that controls the computational efficiency of the simulation without affecting the result. After the system reaches equilibrium, both the composition and diffusion potential slightly fluctuate around their equilibrium values. It can be shown [92] that the feedback algorithm is similar to the variance constrained MC method proposed by Sadigh et al [114].

The study of GB premelting required the knowledge of thermodynamic properties of the bulk solid and liquid phases and the exact positions of the solidus and liquidus lines on the

phase diagram. To compute thermodynamic properties of the solid solution, we used a cubic simulation block containing 5324 perfect lattice cites with periodic boundary conditions. Stress-free ($\sigma_{xx} = \sigma_{yy} = \sigma_{zz} = 0$) semi-grand canonical MC simulations were executed for a set of temperature-composition pairs (T, c) with the desired compositions achieved by properly choosing the diffusion potential. Typically, the system was equilibrated by 3×10^4 MC steps followed by 2×10^5 production steps to gather statistics. The pairs (T, c) were chosen to sample the regions of interest on the phase diagram for both GB premelting simulations and thermodynamic integration as will be discussed later. For each (T, c), a set of properties was computed including the diffusion potential, the average potential energy per atom, and the thermo-chemical expansion factor of the lattice relative to pure Cu at 0 K. Similar calculations were conducted for pure Cu ($c = 0$) for a chosen set of temperatures.

Although the approximate positions of the solidus and liquidus lines predicted by this interatomic potential were known from previous calculations [131] (Fig. 3.5), the premelting simulations required a more precise knowledge of the solidus and liquidus compositions, c_S^* and c_L^*, at temperatures of interest.

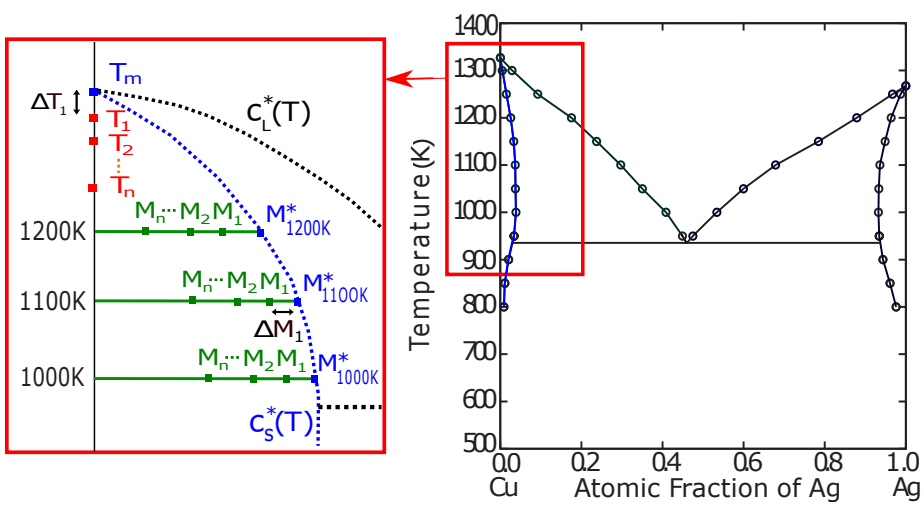

Figure 3.5: Right: Phase diagram of the Cu-Ag system calculated with the EAM potential [131] utilized in this work. Left: Zoomed-in view of the Cu rich side of the phase diagram showing the sampling method of temperatures and compositions studied in this work.

They were calculated at the temperatures of 1000 K, 1100 K and 1200 K by the following phase-coexistence procedure. A rectangular periodic simulation block was prepared with dimensions of approximately $4 \times 4 \times 16$ nm containing 22,000 atoms. The block contained two regions filled with the solid and liquid phases separated by a (210)-oriented solid-liquid interface normal to the long direction z. The lattice of the solid phase was pre-expanded according to the equilibrium lattice parameter at the chosen temperature and the equilibrium diffusion potential M^* estimated in the previous work [131]. Since the final values of M^* were close to the initial estimates, the solid phase remained virtually stress-free. Next, a composition-controlled MC simulation run was executed at a fixed cross-section of the simulation block and zero-stress condition imposed in the z direction. Knowing the previously estimated c_S^* and c_L^* values, the imposed chemical composition c was selected by the lever rule so as to give an approximately 50:50 volume fraction of both phases. After equilibration, a 3×10^6 MC step simulation was performed to compute refined values of M^*, c_S^* and c_L^*. The latter were obtained by averaging the compositions of bulk regions inside each phase unaffected by the interface. The results are summarized in Tab. 3.1, which also includes the computed atomic volume v_L^* of the liquid phase.

Table 3.1: Solid-liquid coexistence properties on the Cu-rich side of the Cu-Ag system: The diffusion potential M^*, the solidus and liquidus compositions c_S^* and c_L^*, and the volume per atom in the liquid phase v_L^*. 1325.25 K is the estimated melting point of pure Cu.

T (K)	M^* $\left(\frac{\text{eV}}{\text{atom}}\right)$	c_S^* (%Ag)	c_L^* (%Ag)	v_L^* $\left(\frac{\text{nm}^3}{\text{atom}}\right)$
1000	0.5692	39.83	3.69	.01552
1100	0.5194	28.06	3.36	.01493
1200	0.4437	15.66	2.26	.01426
1325.25	—	0	0	.01339

Similar calculations were performed for solid-liquid coexistence in pure Cu, excepts that the MC ensemble was canonical. While our previous calculations[131] and work by other authors suggested that the melting temperature predicted by the present EAM potential is

between 1326 and 1327 K, in this work we find that $T_m = 1325.25$ K provides more consistent results for GB premelting (see details below). The 1 K scatter of the temperatures may reflect system size effects and/or limitations of different calculation methods. At 1325.25 K, there was no discernible growth of either phase during the longest MC simulation runs that we could afford. The melting enthalpy H_m was calculated from the energy difference between the phases at 1325.25 K. The obtained $H_m = 0.1239$ eV/atom is in good agreement with 0.1244 eV/atom reported previously [131].

3.2.2 Grain boundary simulations

Three symmetric tilt GBs were studied in this work: Σ5(210)[001], Σ17(530)[001] and Σ13(320)[001]. Here, Σ is the reciprocal density of coincident sites, [001] is the tilt axis, and the symbols in parentheses indicate the GB plane. In the remainder of the chapter, these boundaries will be refereed to as Σ5, Σ17 and Σ13, respectively. Their 0 K structures were obtained by applying standard geometric constructions and minimizing the total energy with respect to local atomic displacements and rigid translations of the grains relative to each other [119]. The GB structures obtained are in agreement with previous simulations [17] as shown in Fig. 3.6.

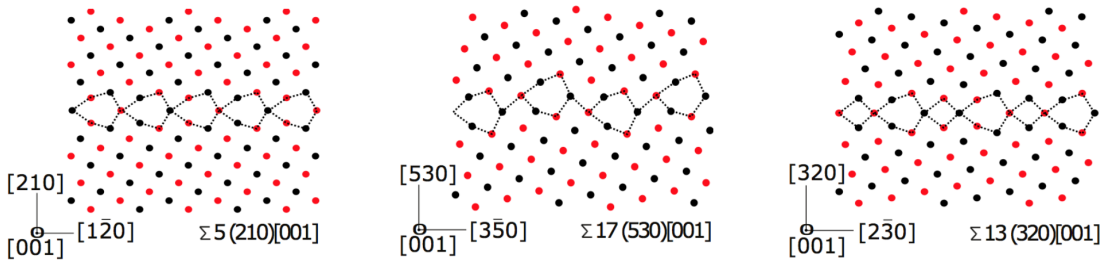

Figure 3.6: Atomic structures of three GBs studied in this work. The tilt axis [001] is normal to the page and the kite-shaped structural units are outlined. The red and black atoms belong to alternating (002) atomic planes.

Their 0 K energies, misorientation angles and dimensions of the periodic simulation

blocks are listed in Table 3.2. Note that the GB energy decreases in the order Σ5, Σ17 and Σ13.

Table 3.2: Properties of the three symmetrical tilt GBs studied in this work: the lattice rotation angle around the [001] tilt axis, the 0 K GB energy γ, the number of atoms in the simulation block N, and the block dimensions. The GB plane is normal to the z-axis.

Boundary	Tilt angle	γ (J/m^2)	N	L_x (nm)	L_y(nm)	L_z(nm)
Σ5(210)	53.13°	0.951061	22000	4.04	3.98	16.17
Σ17(530)	61.93°	0.856302	21216	4.23	4.69	12.63
Σ13(320)	67.38°	0.790050	29120	5.21	5.06	13.03

For pure Cu GBs, canonical MC simulations were performed at several temperatures from 100 K to 1324 K (1 K below the melting point). As with bulk simulations, the system was pre-expanded by the known thermal expansion factor of the lattice. The (x, y) cross-section of the simulation block was then fixed while the z-dimension (normal to the GB plane) was allowed to fluctuate to maintain the $\sigma_{zz} = 0$ condition. These boundary conditions ensured zero stress inside the grains while allowing the thermal expansion of the GB region to be different from that of the lattice.

At temperatures below 1280 K, the GB structures were relatively ordered and premelting was not a consideration. Simulations at these temperature were carried out solely to obtain data needed for the subsequent thermodynamic integration (see Secs. 3.2.5 and 3.3.1.2). At each temperature, the system was equilibrated by 10^5 MC steps before a production run for 5×10^5 MC steps. Snapshots were saved every 2000 steps. Above 1280 K, the simulations were run much longer (typically, between 4×10^6 and 3×10^7 MC steps) in order to obtain sufficient statistics of GB width fluctuations. The temperature step was reduced as temperature increased. The temperatures closest to the melting point were 1300 K, 1310 K, 1315 K, 1320 K and 1324 K.

For binary alloys, the simulation block was similarly pre-expanded according to the lattice parameter at the chosen temperature and grain composition. Semi-grand canonical

MC simulations were carried out with a fixed GB cross-section and fluctuating z-dimension maintaining the $\sigma_{zz} = 0$ condition. At each of the three temperatures studied (1000 K, 1100 K and 1200 K), the simulations were run for two sets of diffusion potentials. The first set started with dilute alloys and sampled grain composition far away from the solidus line. Such simulations were only needed for thermodynamic integration as will be discussed later. The second set included grain compositions very close to the solidus line and was designed for the fluctuation analysis of the GB width. The numbers of MC steps implemented in both sets were similar to those for pure Cu far away and close to the melting point, respectively.

To verify that the scaling of the lattice indeed ensured zero stress conditions inside the grains, multiple snapshots containing local stress data were averaged to compute the stress profiles $\sigma_{ij}(z)$. For both pure Cu and Cu-Ag alloys, such profiles showed a nearly perfect zero stress inside the grains and a sharp spike of σ_{xx} and σ_{yy} caused by the interface stress in the GB regions.

3.2.3 Calculation of the grain boundary width distribution

The width w of a premelted GB was identified with the width of the liquid layer formed inside the boundary. The first step in calculating w was to construct an order parameter profile across the boundary. As such, we chose the parameter characterizing the periodic order of the (002) crystal planes normal to the tilt axis [001] (y-direction) [39, 40, 120]. This order parameter is the modulus of the structure factor $S(\boldsymbol{k})$ computed for a set of bins parallel to the GB plane:

$$|S_i(\boldsymbol{k})| = \sqrt{\left(\frac{\sum_j \cos(\boldsymbol{k}\cdot\mathbf{r}_j)}{N_i}\right)^2 + \left(\frac{\sum_j \sin(\boldsymbol{k}\cdot\mathbf{r}_j)}{N_i}\right)^2}, \tag{3.26}$$

where $\boldsymbol{k} = 2\pi(0, 2/a, 0)$ is the reciprocal lattice vector, $\mathbf{r}_j$ is the position of atom j in bin i, a is the cubic lattice parameter in the grains, and the summation runs over all N_i atoms in the bin. This order parameter is unity in the perfect crystal at 0 K, has a positive value

smaller than 1 in the grains at finite temperatures, and is zero in the liquid phase. An example of an order parameter profile $|S_i|(z_i)$ computed from a single snapshot is shown in Fig. 3.7, z_i being the center of bin i and the bin width was 0.0615 nm. The scatter of the points is due to thermal noise.

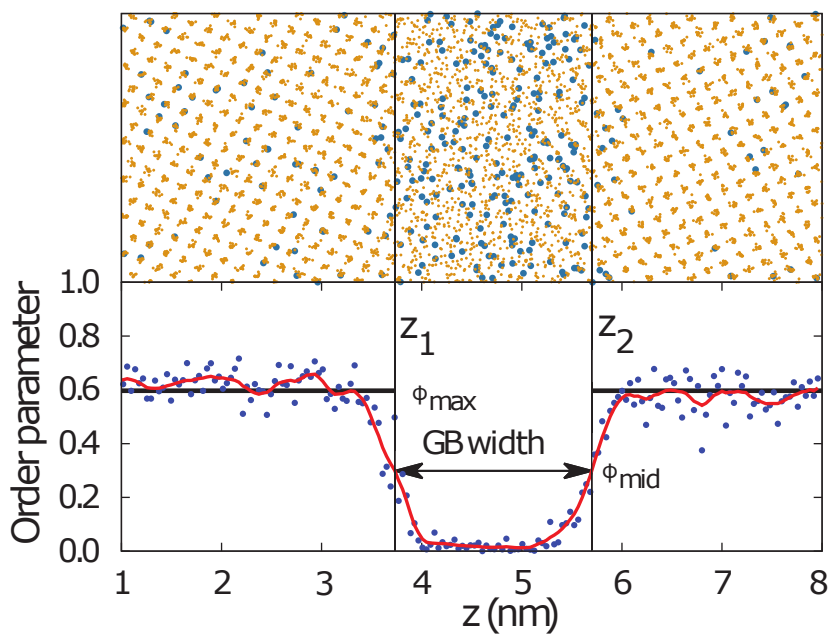

Figure 3.7: Typical order parameter profile used to calculate the GB width in a single snapshot. The blue points are raw values of the structure factor $|S_i|(z_i)$ and the red curve is the smoothed profile $\phi_i(z_i)$. The simulation was for the Σ5 GB at 1200 K with the grain composition of 2.23 at.%Ag. The upper image shows the atomic positions projected along the [001] tilt axis normal to the page, with yellow points representing Cu atoms and blue points Ag atoms.

To mitigate the noise effect, a smoothing procedure was applied where each of the $|S_i|$ values was averaged with two neighboring points on either side. This resulted in a smoothed profile that we denote $\phi_i(z_i)$ and show as a red curve in Fig. 3.7 (the discrete points are connected by line segments).

The grain value ϕ_{max} was computed by averaging over regions far away from the GB. Next, two locations z_1 and z_2 were found at which the order parameter was equal to ϕ_{mid}=

$\phi_{max}/2$. Because the function $\phi_i(z_i)$ is discrete, linear interpolation of ϕ_i was applied to find z_1 and z_2. The GB width was then defined as the difference $w = |z_1 - z_2|$. Note that, due to the periodic boundary conditions, each snapshot effectively contained two GBs, both of which were used to calculate w. For the alloy system, the chemical composition profile could be alternatively used to calculate w. However, we chose to use the structural order parameter throughout this work to ensure consistency between the alloy and pure Cu simulations.[3]

The described calculation of w was repeated for all N_p snapshots saved in each simulation. The number of snapshots increased as the simulation condition approached the solidus line. From the entire set of GB widths obtained in a simulation, a histogram was constructed using the number of bins $2(N_p)^{1/3}$ (Rice rule). The histogram was then scaled by the bin width and divided by N_p to obtain a discrete probability density function $P_i(w_i)$ normalized to unity of its midpoint Riemann sum. As an example, Fig. 3.8 shows a set of probability functions for the $\Sigma 5$ boundary at 1000 K. In total, twelve such sets were generated in this work (three GBs, three temperatures for the alloys, and one temperature set for pure Cu).

3.2.4 Calculation of the disjoining potential

As discussed in Sec. 3.1.3, the GB width distribution $P(w)$ is related to the disjoining potential $\Psi(w)$ by Eq.(3.20). Inverting this equation,

$$\Psi(w) = -\frac{k_B T}{A} \ln P(w) + p_d^0 w + D, \tag{3.27}$$

where D is the logarithm of the normalization coefficient. Recall that p_d^0 is given by Eq.(3.16) for pure Cu and by Eq.(3.13) for a Cu-Ag alloy, the superscript 0 being a reminder that

[3] As indicated in Sec. 3.1.1, the GB width w is defined as the distance between two dividing surfaces in the solid-liquid interfaces satisfying the condition $\tilde{N} = 0$. The described practical definition of w through the order parameter profile need not satisfy this condition and constitutes an approximation. The larger w, the more accurate this approximation becomes.

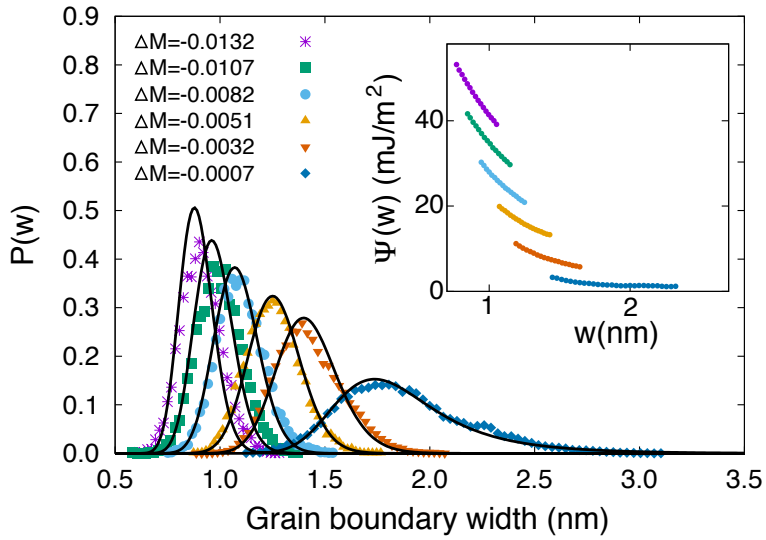

Figure 3.8: Probability density functions $P_i(w_i)$ for different values of ΔM (in eV) computed for the $\Sigma 5$ GB at the temperature of 1000 K. The inset shows the segments of the disjoining potential extracted from these functions. The curves are the normalized distributions predicted by the analytical disjoining potential.

this disjoining pressure is computed at the bulk solid-liquid equilibrium. The undercooling temperature ΔT and undersaturation potential ΔM are known in each simulation.

Ideally, if the function $P(w)$ could be computed accurately over the entire range $0 \leq w < \infty$, the coefficient D could be determined from the normalization condition $\int_0^\infty P(w)dw = 1$. The entire disjoining potential $\Psi(w)$ could be then obtained from a single simulation. In reality, a reliable calculation of $P(w)$ is limited to a certain interval around the peak and accurate normalization is unfeasible. Since D remains unknown, a single simulation recovers only a segment of $\Psi(w)$ up to an arbitrary vertical shift D. Examples of such segments are shown in Fig. 3.8. In this work, each segment was obtained from the probability distribution function in the interval $\bar{w} \pm 1.5\sigma$, where $\bar{w}$ is the average GB width estimated from the given distribution and σ is the standard deviation of the distribution.[4] The points outside this interval had relatively small probabilities and were usually not fully converged. Accordingly,

[4]For bimodal distributions, the segment of $\Psi(w)$ was calculated in the interval $0.8 \leq w \leq 2.2$ nm that encompassed both peaks. The rest of the distribution consisted of very small probabilities and was excluded.

they were not included in the calculation. Note that the segments calculated at different undercoolings (respectively, undersaturations) were defined in overlapping width intervals.

The next step was to join the segments together into a single continuous curve. This was accomplished by shifting the segments relative to each other so as to minimize the mean-square deviation between neighboring segments in the overlap intervals. Since the segments did not generally share the same mesh, they had to be remapped onto a common mesh in the overlap region using a linear interpolation scheme. The minimization was then implemented on this common mesh. Once the shifts were optimized, the values of $\Psi(w)$ in the overlap regions were obtained by averaging over the two segments on the common mesh.

This procedure resulted in a continuous curve defined up to a rigid shift that remained an unknown parameter. The postulated analytical potential given by Eq.(3.23) was then fitted to this curve. To this end, the mean-square deviation between the curve and the function was minimized with respect to six fitting parameters c_i plus the rigid shift.[5]

3.2.5 Calculation of properties for thermodynamic integration

Calculations of the GB free energy by thermodynamic integration required the knowledge of certain GB and bulk properties as functions of temperature and/or grain composition. Such properties include $\tilde{U}$, $\tilde{N}_2$, L_x, L_y, τ_{ii}, $(\partial e_{ii}/\partial T)_{c=0}$, $(\partial e_{ii}/\partial c)_T$ $(i = 1, 2)$ and $(\partial M/\partial c)_T$. Here c is the grain composition (it was earlier denoted c_S in the context of solid-liquid coexistence; we can now simplify the notation).

For GBs, the tilde sign denotes the Gibbsian excesses computed at a fixed number of

[5]Formally, extrapolation of $\Psi(w)$ to $w \to 0$ gives $(\gamma_{\rm dry} - 2\gamma_{SL})$, where $\gamma_{\rm dry}$ is the free energy of a hypothetical "dry" GB in which the two solid-liquid interfaces are infinitely close to each other. Clearly, in this limit the entire liquid layer model loses its physical meaning. On the other hand, since the simulations only sampled GB widths larger than several Angstroms, the function fitted in this width interval could display totally unreasonable behavior when extrapolated to the $w \to 0$ limit. Therefore, we chose to impose the boundary condition $\Psi(w) \to (\gamma_{\rm dry} - 2\gamma_{SL})$ at $w \to 0$ with a small weight during the curve fitting. We approximated $\gamma_{\rm dry}$ by the GB energy at 0 K and used the γ_{SL} values obtained by forcing the liquid layer model to match the thermodynamic integration result at the last point of the simulations (see text for more detail). This condition did not practically affect the quality of the fit in the physically meaningful width interval but gave a reasonable order of magnitude of $\Psi(w)$ at $w \to 0$.

atoms ($\tilde{N} = 0$).[6] In pure Cu, the excess energy $\tilde{U}$ was first computed in each snapshot by the following procedure. Knowing the locations of the two GBs from the order parameter profile, a layer containing each boundary together with surrounding grain regions was selected. Let the total energy and total number of atoms in both layers together be U_I and N_I, respectively. The rest of the simulation block was comprised of lattice regions unperturbed by the GBs. Their total energy U_g and number of atoms N_g represented a reference grain system. The excess $\tilde{U}$ was computed from the equation

$$2\tilde{U} = U_I - N_I \frac{U_g}{N_g}, \tag{3.28}$$

where the factor of 2 takes into account that the right-hand side represents two GBs. This $\tilde{U}$ was then averaged over all snapshots saved during the simulation. In alloys simulations, the excess Ag amount was computed in a similar manner using the equation

$$2\tilde{N}_2 = N_{2I} - N_I \frac{N_{2g}}{N_g}. \tag{3.29}$$

The cross-sectional dimensions of the GB, L_x and L_y, were known as functions of temperature and grain composition from the perfect-lattice simulations described in Sec. 3.2.1. From these data, the derivatives

$$\left(\frac{\partial e_{11}}{\partial T}\right)_{c=0} = \frac{1}{L_x}\left(\frac{\partial L_x}{\partial T}\right)_{c=0}, \quad \left(\frac{\partial e_{22}}{\partial T}\right)_{c=0} = \frac{1}{L_y}\left(\frac{\partial L_y}{\partial T}\right)_{c=0}, \tag{3.30}$$

$$\left(\frac{\partial e_{11}}{\partial c}\right)_{T} = \frac{1}{L_x}\left(\frac{\partial L_x}{\partial c}\right)_{T}, \quad \left(\frac{\partial e_{22}}{\partial c}\right)_{T} = \frac{1}{L_y}\left(\frac{\partial L_y}{\partial c}\right)_{T} \tag{3.31}$$

were calculated by numerical differentiation using polynomial fits through the relevant sets

[6] In terms of generalized excesses describing GBs [43, 44], $\tilde{X}$ is equivalent to $[X]_N$, X being any extensive property.

of temperatures or compositions. The GB area $A = L_x L_y$ was also calculated as a function of temperature and/or composition.

The diffusion potentials and the respective grain compositions were known from the MC simulations of bulk phases discussed in Sec. 3.2.1. The derivative $(\partial M/\partial c)_T$ was computed from a polynomial fit through the set of points (M, c) at a fixed temperature.

The interface stress was calculated from the relation [39–42, 44]

$$\tau_{ii} = \frac{\sigma_{ii} V}{A}, \quad , i = 1, 2, \tag{3.32}$$

V being the system volume. This equation assumes zero stress outside the GB region, which was ensured in the present simulations. The work term $\sigma_{ii} V$ was computed by summing up the virial stress tensors over all atoms inside the interface layer (containing the GB and grain regions) and averaging over all snapshots.

Finally, thermodynamic integration required the knowledge of one reference value γ_{ref} of the GB free energy. To obtain it, the free energy of each GB in pure Cu was calculated in the quasi-harmonic approximation at the reference temperature $T_{\text{ref}} = 300$ K as in previous work [32, 40, 44]. The values obtained were 0.888 J/m^2, 0.798 J/m^2 and 0.737 J/m^2 for the $\Sigma 5$, $\Sigma 17$ and $\Sigma 13$ GBs, respectively.

3.3 Simulation results and interpretation

3.3.1 Grain boundary premelting in pure Cu

3.3.1.1 Premelting behavior and disjoining potentials

In all three GBs studied, the formation of a liquid layer was observed as the bulk melting point was approached from below; however, the extent of premelting was different. Fig. 3.9 illustrates the gradual accumulation of disorder in the $\Sigma 5$ GB with increasing temperature culminating in the formation of a thick liquid layer a few degrees below T_m.

To demonstrate the differences between the GBs, Fig. 3.10 shows typical snapshots at

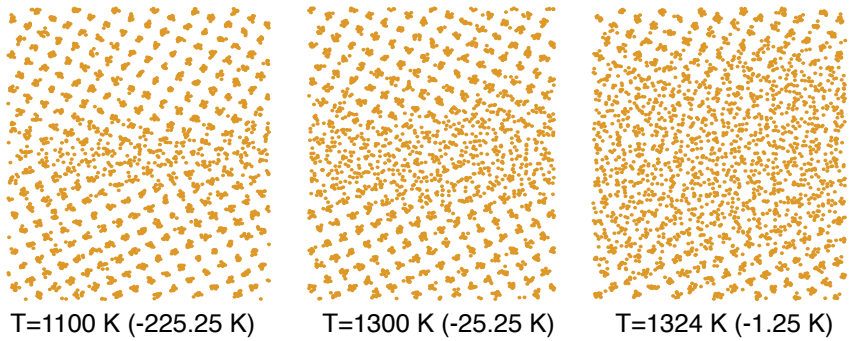

Figure 3.9: Premelting of the Cu Σ5 GB at three different temperatures below the bulk melting point. The atomic positions are projected along the [001] tilt axis normal to the page. The number in parentheses is the undercooling ΔT.

$\Delta T = -15.25$ K together with the width probability distributions. While the Σ5 and Σ17 GBs are strongly premelted at this temperature, the Σ13 GB is disordered but not to the extent that it could be described as a liquid layer. These different behaviors are reflected in different positions of the peak of the GB width distribution.

The plots of the average (over the probability distribution) GB width $\bar{w}$ as a function of undercooling ΔT (Fig. 3.11) indicate that, in all three GBs, the liquid layer thickness diverges to infinity at the bulk melting point. As discussed in Sec. 3.1, this behavior is indicative of a repulsive disjoining potential.

As mentioned above, the disjoining potentials reconstructed from individual segments (Fig. 3.12) were initially defined up to an unknown rigid shift.

They were then fitted by the analytical function in Eq.(3.23) with six parameters plus the rigid shift as the seventh fitting parameter. Fig. 3.13 summarizes the disjoining potentials for the three GBs with optimized rigid shifts. By its physical meaning, $\Psi(w)$ must approach zero in the limit of $w \to \infty$ (no interaction between isolated solid-liquid interfaces). Note, however, that at the largest GB widths sampled in the simulations, some of the obtained $\Psi(w)$ points are slightly above or slightly below zero due to statistical errors. Such deviations from zero are especially pronounced for the Σ13 GB at $w > 3.5$ nm. For this boundary,

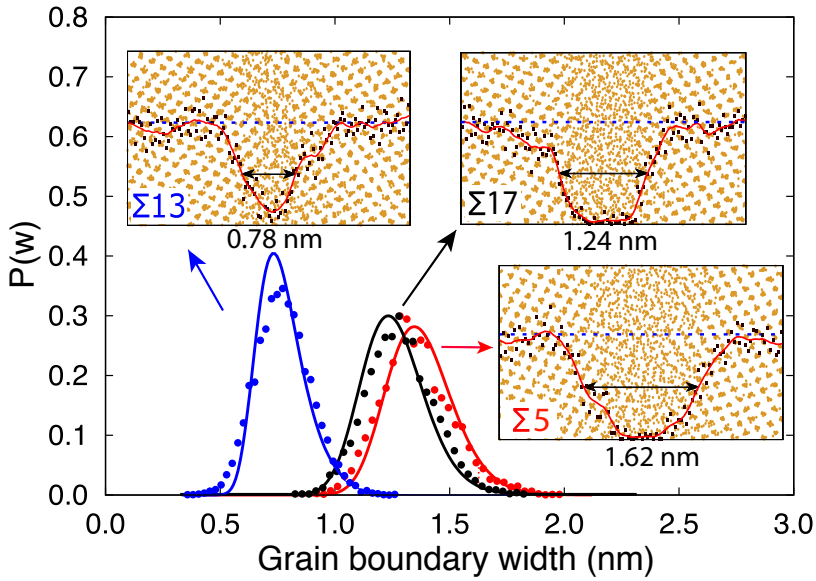

Figure 3.10: Width probability distributions $P(w)$ for three GBs in Cu at 1310 K ($\Delta T = -15.25$ K) with snapshots of the premelted structures. The points represent the original histograms while the curves are the normalized distributions predicted by the analytical disjoining potential. The atomic positions are projected along the [001] tilt axis normal to the page. The numbers indicate the GB widths in the snapshots.

the deviations could represent a combined effect of statistical errors and systematic factors. Indeed, the $\Sigma 13$ boundary remains rather narrow and displays only slight premelting until a few degrees below the melting point. Under such conditions, modeling this boundary by a liquid layer is a more drastic approximation than for the $\Sigma 5$ and $\Sigma 17$ GBs.

As evident from Figs. 3.10-3.13, the $\Sigma 5$ GB exhibits the most extensive premelting and can be represented by a liquid layer most accurately. Accordingly, we expect that its disjoining potential must be exponentially repulsive and become practically zero at $w > 3.5$ nm. It was found that to meet this condition, a precise adjustment of the bulk melting point of Cu was necessary. As already mentioned, $T_m = 1325.25$ K was found to give the most accurate agreement with zero Ψ at $w > 3.5$ nm. With this melting temperature, the disjoining potential of the $\Sigma 5$ GB could be fitted by a purely exponential function [$c_3 = 0$ in Eq.(3.23)]. By contrast, accurate fitting for the $\Sigma 17$ and $\Sigma 13$ GBs required all terms

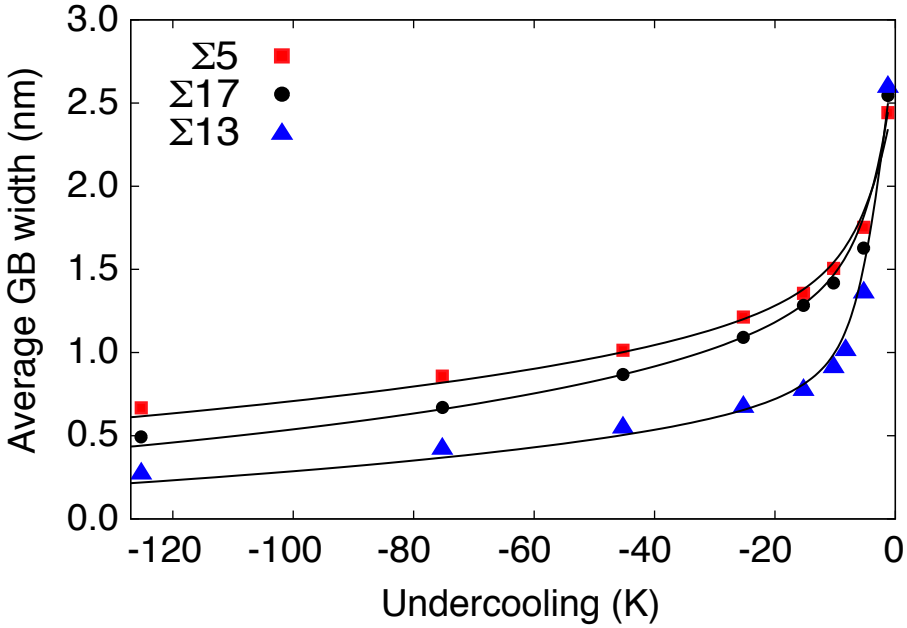

Figure 3.11: Average GB width $\bar{w}$ as a function of undercooling ΔT for the pure Cu GBs.

in Eq.(3.23). Note that for the Σ13 GB, the disjoining potential below 1.5 nm exhibits a characteristic shape suggestive of a developing shoulder.

As a consistency check, the analytical disjoining potentials obtained by the fitting were inserted in Eq.(3.20) and the width probability distributions were normalized to unity by numerical integration. The probability distributions obtained are shown by solid curves in Figs. 3.8, 3.10 and 3.12. At temperatures close to the melting point, these curves reproduce the individual distributions quite well. At larger undercoolings, the agreement becomes less accurate, which is not surprising given that the GBs become nearly dry and their description as a liquid layer is a crude approximation.

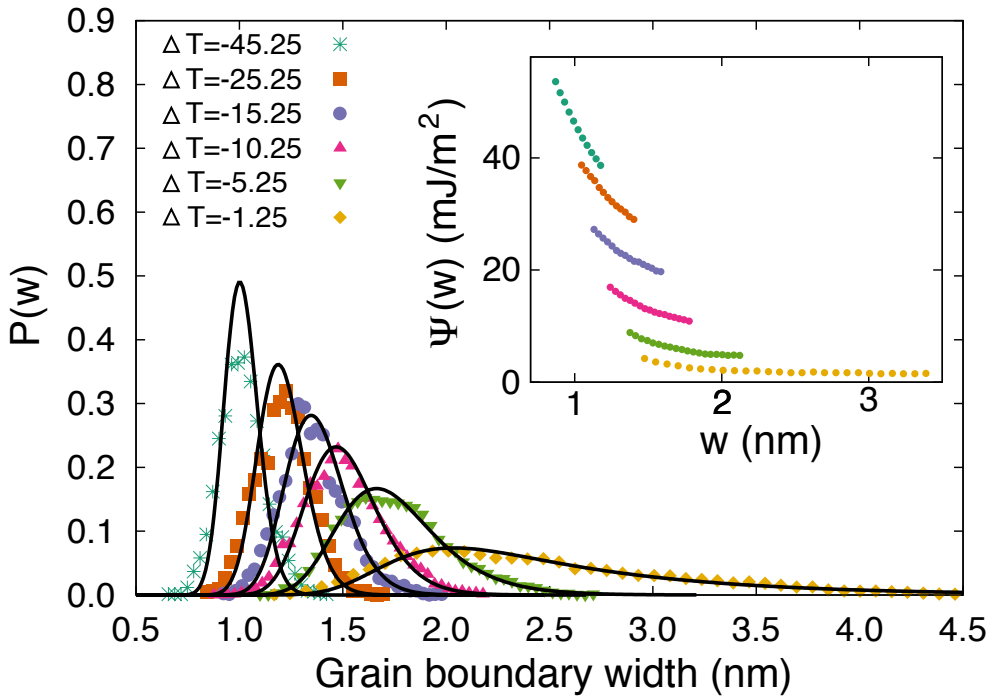

Figure 3.12: Probability density functions for different undercoolings ΔT (in K) for the $\Sigma 5$ GB in pure Cu. The points represent the original histograms while the curves are the normalized distributions predicted by the analytical disjoining potential. The inset shows segments of the disjoining potential obtained by inversion of individual probability functions.

3.3.1.2 Free energy of premelted grain boundaries

The GB free energies were computed by thermodynamic integration. We used the integration scheme [44]

$$\gamma(T) = \frac{A_{\mathrm{ref}} T}{A T_{\mathrm{ref}}} \gamma_{\mathrm{ref}} + \frac{T}{A} \int_{T_{\mathrm{ref}}}^{T} \left(\sum_{i=1}^{2} \frac{A \tau_{ii}}{T} \frac{\partial e_{ii}}{\partial T} - \frac{\tilde{U}}{T^2} \right) dT, \tag{3.33}$$

where the excess energy $\tilde{U}$ and the interface stress τ_{ii} were discussed in Sec. 3.2.5. The quantities with index "ref" must be computed in the reference state. The term with the

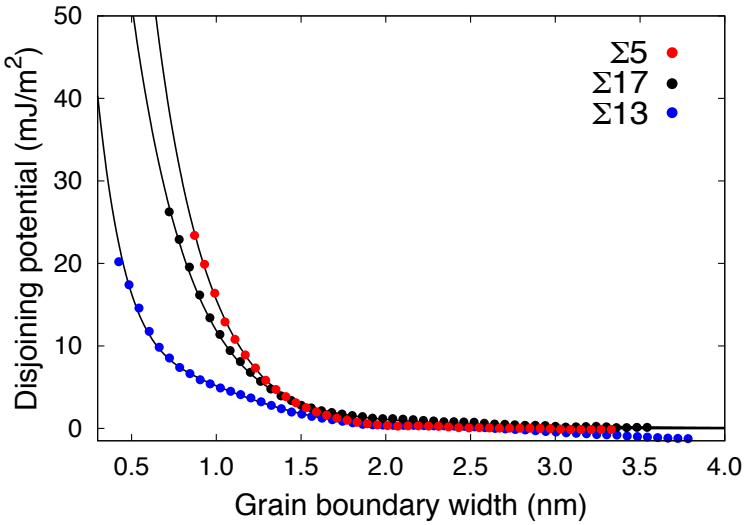

Figure 3.13: Disjoining potentials for three GBs in pure Cu. The points represent simulation results from the GB width fluctuations. The solid lines are analytical disjoining potentials fitted to the points as discussed in the text.

excess energy makes the leading contribution to the integral. Fig. 3.14 shows the excess energy per unit GB area as a function of temperature.

This energy remains nearly constant at low temperatures and sharply increases in the premelting region. It is interesting to note that the ranking of the GB energies at 0 K ($\gamma_{\Sigma 5} > \gamma_{\Sigma 17} > \gamma_{\Sigma 13}$) persists all the way to the melting point. This trend suggests that high/low energy GBs at 0 K are likely to remain high/low energy boundaries at all temperatures. Accordingly, the 0 K GB energy can be a reasonably good predictor of premelting behavior. This correlation was also noted in the previous phase field studies on GB premelting [95]. The reference temperature T_{ref} was 300 K and the integration in Eq.(3.33) was carried out numerically.

The functions $\gamma(T)$ for the three GBs are plotted in Fig. 3.15.

The plots include the GB energies at 0 K and the free energies at 100 K and 200 K computed in the quasi-harmonic approximation. These extra points demonstrate a smooth

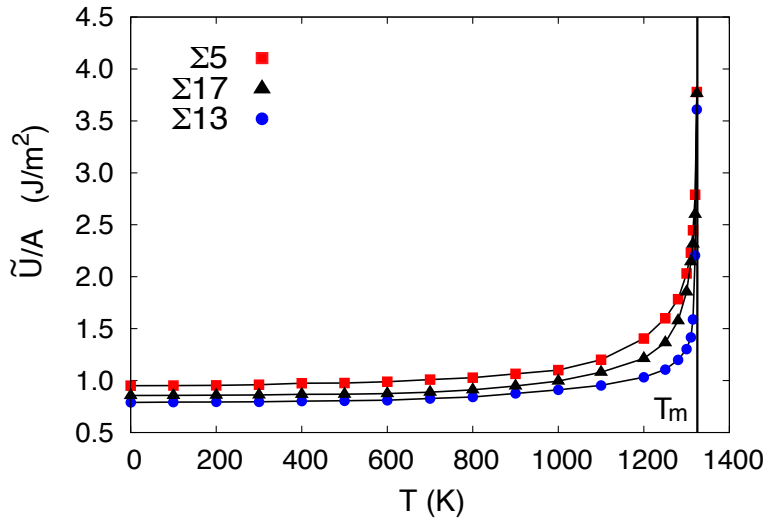

Figure 3.14: Excess energy per unit area, $\tilde{U}/A$, as a function of temperature for three GBs in pure Cu. The vertical line indicates the bulk melting point.

continuation of the curves below the temperature range 300 K $\leq T \leq$ 1324 K of thermodynamic integration. Although this method becomes less accurate as we deviate further away from the reference state, it was interesting to examine the values of γ at the bulk melting point. In the liquid layer model with a repulsive disjoining potential, these γ are expected to give $2\gamma_{SL}$. Thus, γ_{SL} could be obtained by linear extrapolation of the plots from 1324 K to 1325.25 K. Instead, we used a slightly more refined procedure explained below. The calculation gives the γ_{SL} values of 0.196 J/m^2, 0.194 J/m^2 and 0.192 J/m^2 for the $\Sigma5$, $\Sigma17$ and $\Sigma13$ GBs, respectively. These numbers refer to the solid-liquid interface orientations of (210), (320) and (520), respectively. The orientation dependence of γ_{SL} suggested by these numbers is small. All three numbers are in close agreement with $\gamma_{SL} = 0.199$ J/m^2 obtained in the previous work [39, 40] for the (110) interface orientation using the same interatomic potential.

The GB free energy can also be calculated within the liquid layer model using the analytical disjoining potentials $\Psi(w)$ and the normalized width probability distributions

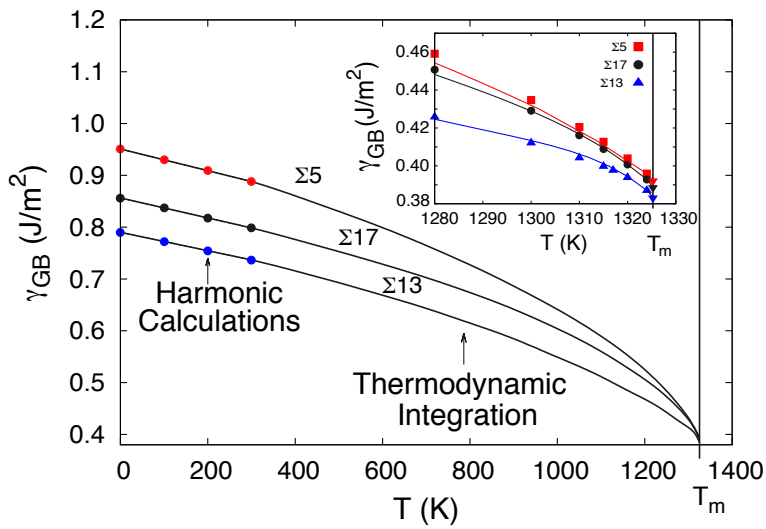

Figure 3.15: GB free energy as a function of temperature for three GBs in pure Cu. The main plot shows the results of thermodynamic integration. The inset compares these results with predictions of the liquid layer model near the melting point (points).

$P(w)$. Note that thermodynamic integration naturally includes the effect of GB width fluctuations. Thus, the quantity that should be compared with the results of thermodynamic integration is the GB free energy $\bar{\gamma}$ averaged over the width distribution. Using Eq.(3.18) we obtain

$$\bar{\gamma} = 2\gamma_{SL} + \overline{\Psi(w)} - p_d^0 \bar{w}, \tag{3.34}$$

where the bar denotes averaging over the width probability distribution:[7]

$$\bar{w} = \int_0^\infty wP(w)dw, \tag{3.35}$$

$$\overline{\Psi(w)} = \int_0^\infty \Psi(w)P(w)dw. \tag{3.36}$$

[7]Note the difference between the average values, such as $\bar{w}$ and $\bar{\gamma}$, and the previously introduced most probable values w_0, γ_0, etc. For highly asymmetric distributions, especially those with two local maxima, they can be numerically different.

These integrals were computed numerically. The following procedure was then applied. We postulate that at the last point sampled (1324 K), $\bar{\gamma}$ matches γ obtained by thermodynamic integration. From this condition, we obtain

$$\gamma_{SL} = \frac{1}{2}\left(\gamma - \overline{\Psi(w)} + p_d^0 \bar{w}\right), \tag{3.37}$$

where $\bar{w}$ and $\overline{\Psi(w)}$ were computed at the last point. The values of γ_{SL} obtained by this procedure were quoted in the previous paragraph. Using these values of γ_{SL}, the entire function $\bar{\gamma}(T)$ was calculated from Eq.(3.34). The inset in Fig. 3.15 compares the GB free energies computed by the two methods. Given that the two calculations are independent (except for forcing their match at 1324 K), the agreement is very good. This lends additional credence to the liquid layer model at premelting temperatures. At lower temperatures, the comparison becomes impossible since the width probability distributions could not be extracted from the simulations and the liquid layer model is not expected to be valid.

3.3.2 Grain boundary premelting in Cu-Ag solutions

3.3.2.1 Premelting behavior and disjoining potentials

As the grain composition c approaches the solidus line, the amount of GB segregation of Ag rapidly increases (Fig. 3.16).

The segregation zone grows wider and the atomic positions within this zone become increasingly disordered. At the undersaturation of $\Delta c = -0.11$ at.%Ag, the $\Sigma 5$ GB becomes essentially a layer of the Cu-Ag liquid solution. This trend is quantified in Fig. 3.17 where the average GB width $\bar{w}$ is plotted against ΔM for all three GBs.

Each GB becomes wider with increasing temperature at a fixed ΔM or with decreasing $|\Delta M|$ at a fixed temperature. At fixed T and ΔM, the GB width decreases in the order $\Sigma 5$, $\Sigma 17$, $\Sigma 13$. While the widths of the $\Sigma 5$ and $\Sigma 17$ GBs diverge to infinity when approaching the solidus line, the $\Sigma 13$ GB retains a finite width at the solidus line. In this case it was

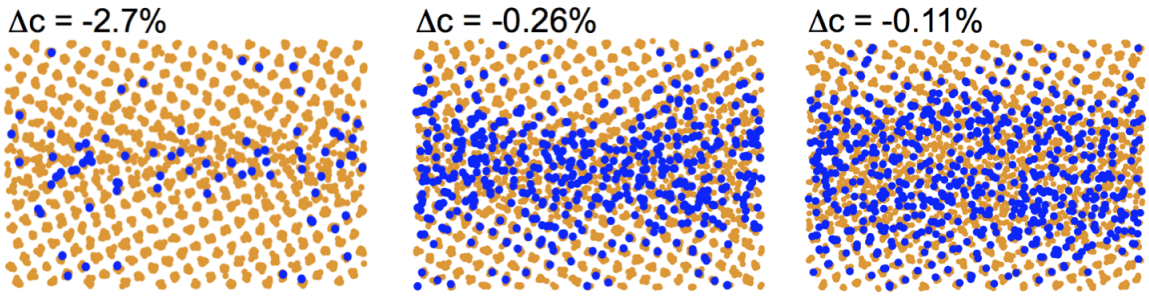

Figure 3.16: Premelted structures of the Σ5 GB at the temperature of 1100 K at different undersaturations Δc (at.%Ag). The atomic positions are projected along the [001] tilt axis normal to the page, with yellow points representing Cu atoms and blue points Ag atoms.

possible to oversaturate the grains beyond the solidus line. In such oversaturated states, the GB width still remained finite until some point at which the entire system abruptly melted.

The disjoining potentials were extracted from the width probability distributions computed by the methodology discussed in Secs. 3.2.3 and 3.2.4 and illustrated in Figs. 3.7 and 3.8. For the Σ5 GB, $\Psi(w)$ remains repulsive at all points along the solidus (Fig. 3.18).

Although the changes in the shape of the disjoining potential are small, there is a trend for it to shift towards smaller GB widths and develop a shoulder at around 1.5-2 nm as the temperature decreases. By contrast, the disjoining potential of the Σ17 GB varies with temperature more dramatically (Fig. 3.19).

As temperature decreases along the solidus line, the initially repulsive disjoining potential of pure Cu gradually transitions to the intermediate shape discussed in Sec. 3.1.4 [cf. Fig. 3.3(a)]. The shoulder on the curve flattens at 1000 K and develops a double-well shape with a shallow minimum at $w \approx 1.3$ nm. This shape evolution originates from the emergence of a second maximum in the width probability distribution as illustrated in Fig. 3.20.

It should be mentioned that, due to the low temperature and complex shape of the distributions, these calculations required the longest simulation runs of all that were implemented

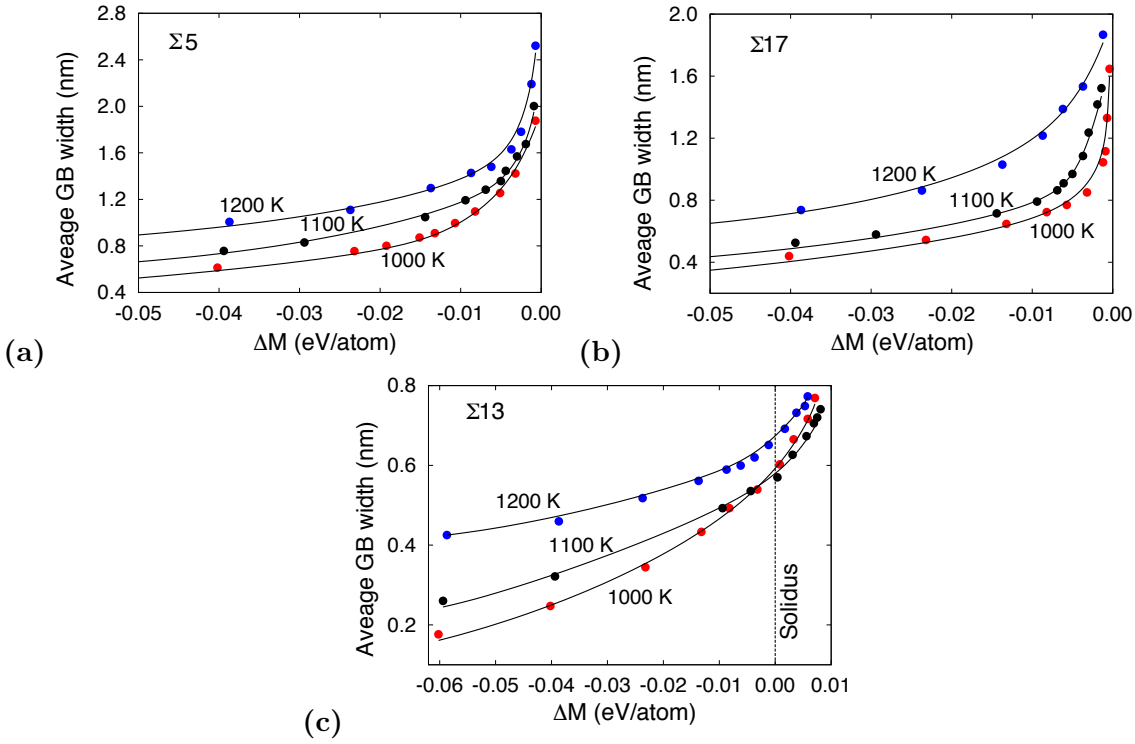

Figure 3.17: Average width of the (a) Σ5, (b) Σ17 and (c) Σ13 GBs in Cu-Ag solid solutions as a function of the diffusion potential ΔM relative the solidus line. The points represent individual simulations. The solid lines are Bezier curves intended to show the trends.

in this work.[8] The results are still subject to larger statistical errors than for single-peak distributions. At $\Delta M = -0.0032$ eV, the distribution does have a single peak. However, as we approach closer to the solidus line ($\Delta M \geq -0.0012$ eV), a second peak emerges and grows higher until we reach the last point closest to the solidus ($\Delta M = -0.0004$ eV) at which the second peak is higher than the first.

Because of the importance of the bimodal distributions as evidence of the intermediate disjoining potential, special care was taken to ensure that the bimodality is not an artifact and to understand its origin. Fig. 3.21 shows a typical fragment of the simulation for the

[8]To obtain additional statistics for the bimodal distributions, the MC simulations were run four times longer than for unimodal distributions. The segments of the disjoining potential had significant overlaps where they did not match as smoothly as for unimodal distributions. Nevertheless, the existence of two peaks and thus the oscillatory region of the disjoining potential at 1000 K (Fig. 3.19) are beyond reasonable doubts.

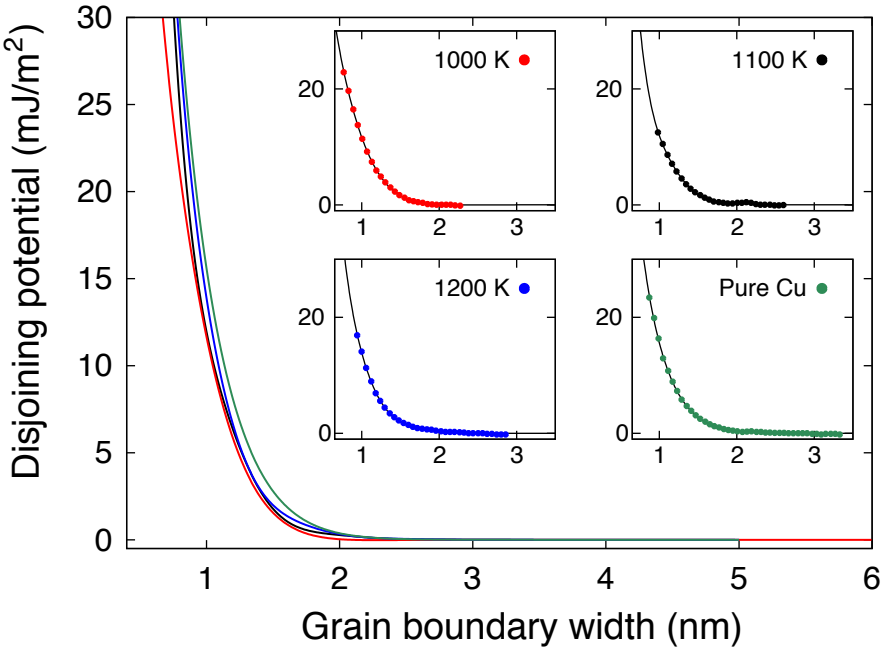

Figure 3.18: Disjoining potentials for the Σ5 GB in the Cu-Ag solid solution at the three different temperatures and in pure Cu. The insets show the fits of the simulation results (points) by the analytical function $\Psi(w)$ (curves). The main plot summarizes the fitted functions.

Σ17 GB at 1000 K for one of the grain compositions showing the bimodality.

The plot clearly shows that the boundary spontaneously switches back and forth between two states, with a smaller and a larger average width. One of the two states is stable while the other metastable. It is the existence of these two states that gives rise to the two peaks in the GB width distribution $P(w)$. The relative heights of the peaks bear information about the relative stability of the two states. Thus, the rise of the peak corresponding to the wider GB state indicates that this GB state becomes increasingly more stable as we approach the solidus line, and eventually becomes more stable than the narrower state. Therefore, we can expect that a thin-to-thick transition occurs between the two states at some value of ΔM. As discussed in Sec. 3.1.4, this transition arises due to the intermediate shape of the disjoining potential.

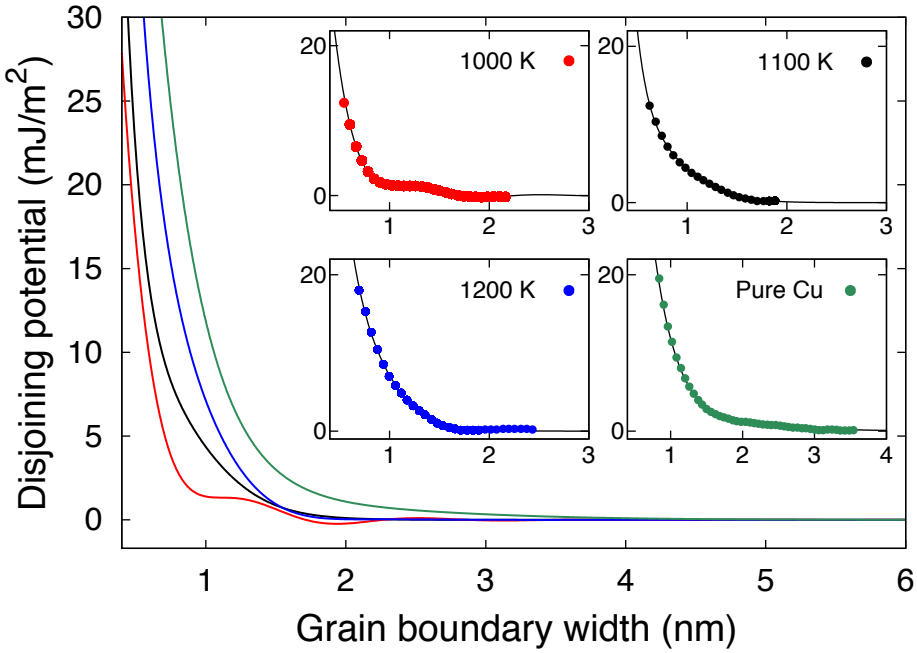

Figure 3.19: Disjoining potentials for the Σ17 GB in the Cu-Ag solid solution at the three different temperatures and in pure Cu. The insets show the fits of the simulation results (points) by the analytical function $\Psi(w)$ (curves). The main plot summarizes the fitted functions. Note the transition of the disjoining potential from repulsive to intermediate with decreasing temperature.

Finally, the disjoining potential of the Σ13 GB evolves from repulsive to attractive as temperature decreases along the solidus line (Fig. 3.22).

In pure Cu, the potential curve is only beginning to develop a shoulder but remains monotonically decreasing with w (cf. Fig. 3.13). Accordingly, the boundary premelts continuously when approaching T_m and can be described by the liquid layer model satisfactorily (although not as accurately as for the two other GBs). As the potential evolves to attractive, the GB width becomes relatively small (< 1 nm) and its description as a liquid layer becomes a crude approximation. Nevertheless, the simulation results show unambiguously that the disjoining potential is attractive. The boundary retains a finite width along the solidus line until close to pure Cu and can be oversaturated beyond the solidus line. The

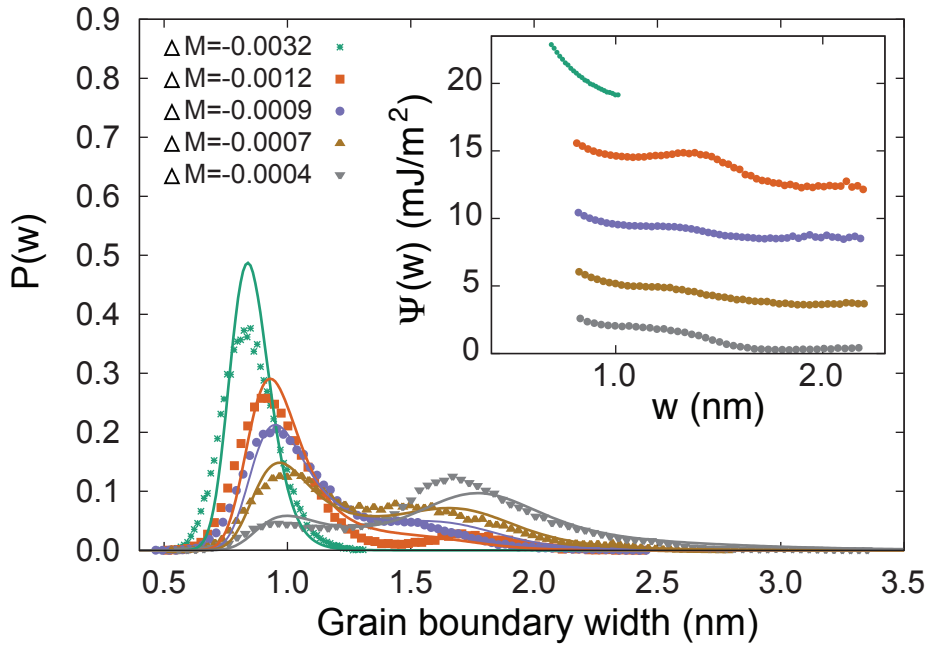

Figure 3.20: Probability density functions for different values of ΔM (in eV) computed for the $\Sigma 17$ GB at the temperature of 1000 K. The points represent the original histograms while the curves are the normalized distributions predicted by the analytical disjoining potential. The inset shows segments of the disjoining potential obtained by inversion of individual probability functions.

shapes of the curves in Fig. 3.22 suggest that $\Psi(w)$ must become intermediate at temperatures between 1200 K and T_m, but a study of this temperature interval was not pursued in this work.

3.3.2.2 Chemical composition of grain boundaries

When a GB becomes a liquid layer, its chemical composition is expected to approach the liquidus composition c_L^* as the grains approach the solidus composition c_S^* at the same temperature. In the previous MC study of the $\Sigma 5$ GB, [130] this trend was indeed followed within the statistical scatter of the data. The present simulations offer the opportunity of a more accurate test of this trend for the $\Sigma 5$ and $\Sigma 17$ GBs (we excluded the $\Sigma 13$ GB for which the notion of a liquid layer is not well-defined).

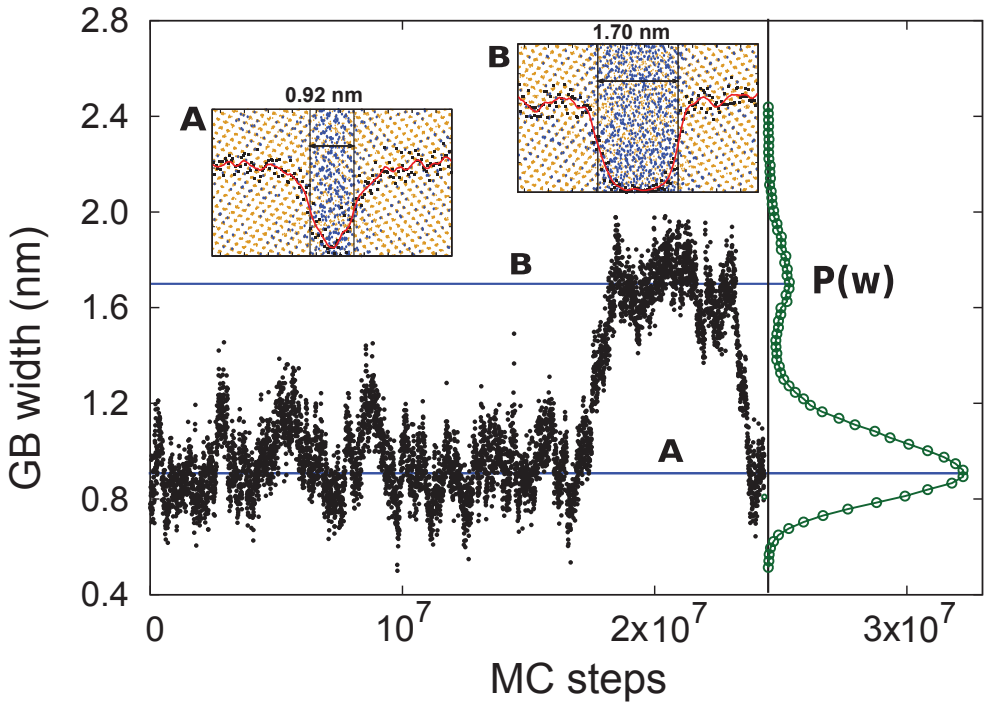

Figure 3.21: A typical fragment of MC simulations for the Σ17 GB at 1000 K with undersaturation $\Delta M = -0.0012$ eV. The GB spontaneously switches between two states, labeled A and B, with different widths. Multiple repetitions of such switches produce two peaks in the width probability distribution $P(w)$. The insets show order parameter profiles in snapshots drawn from the two states. The GB widths in the snapshots are indicated.

Figure 3.23 shows the chemical composition, c_{GB}, at the center of the GB region as a function of ΔM. To find c_{GB}, the bounds z_1 and z_2 of the GB region were calculated from the order parameter profile in each snapshot as illustrated in Fig. 3.7.

The GB center was defined by $z_c = (z_1 + z_2)/2$ and its chemical composition c_{GB} was computed by averaging over a 0.1 nm window centered at z_c. Each point shown in Fig. 3.23 was obtained by averaging c_{GB} over all snapshots saved in the simulation. We observe that at high temperatures, c_{GB} increases monotonically with ΔM and reaches the liquidus composition c_L^* as the grains reach the solidus line ($\Delta M \to 0$). We also see that, at a given ΔM, c_{GB} increases with decreasing temperature. In other words, the GB segregation becomes stronger at low temperatures, suggesting a negative segregation energy (binding of

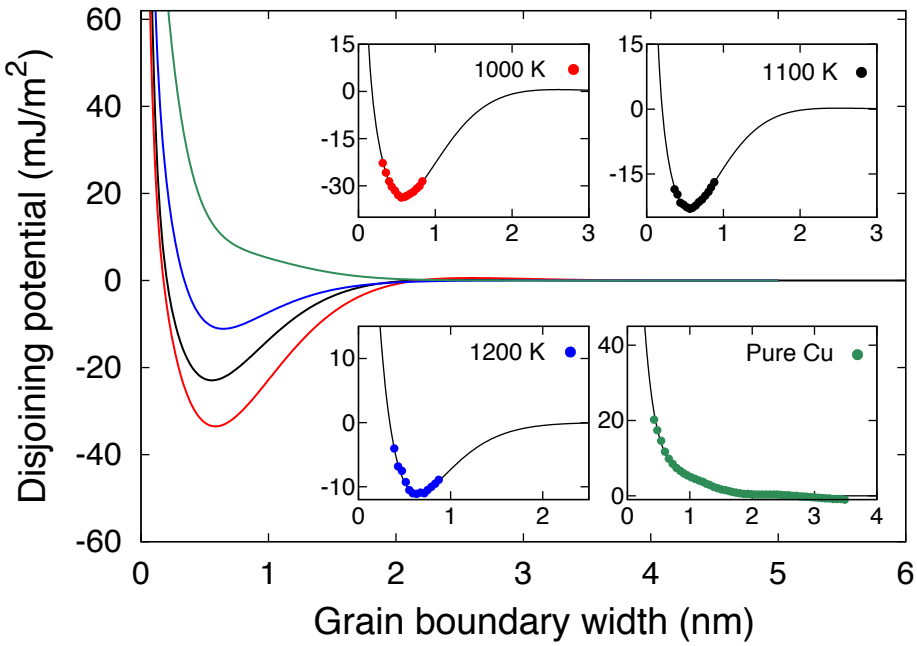

Figure 3.22: Disjoining potentials for the Σ13 GB in the Cu-Ag solid solution at the three different temperatures and in pure Cu. The insets show the fits of the simulation results (points) by the analytical function $\Psi(w)$ (curves). The main plot summarizes the fitted functions.

Ag to the GBs). It is interesting to note, however, that at low temperatures, c_{GB} overshoots c_L^* before turning over and returning to c_L^* from above. Furthermore, at least for the Σ5 GB at 1100 K, the overshoot is followed by a slight undershoot before c_{GB} reaches c_L^*. These subtle but important effects could not be resolved in the previous work [130], nor were they seen in the phase field simulations [95].

For a more detailed understanding of these effects, we examined the local chemical composition profiles across the GBs. To obtain them, the GB center z_c was found in each snapshot and the entire simulation block was translated to bring this point to $z = 0$. This re-centering procedure was applied to all snapshots saved in the simulation. A set of thin layers parallel to the GB plane was then constructed and the chemical composition of each layer was averaged over all snapshots. The discrete composition profile obtained was thus

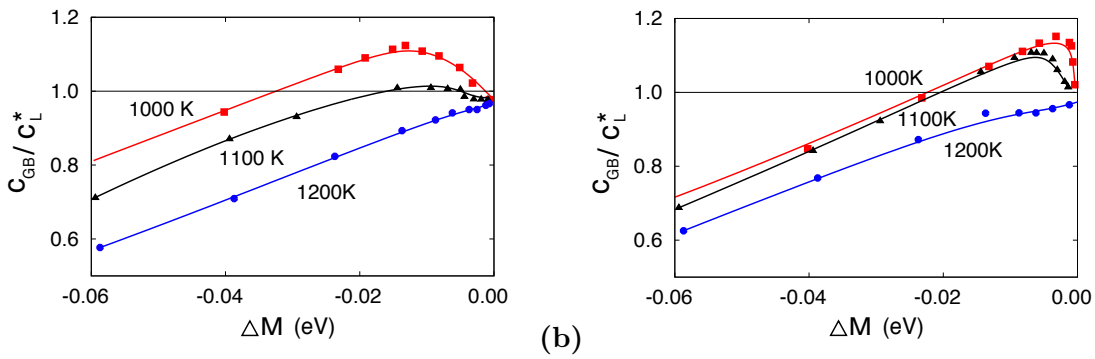

Figure 3.23: Chemical composition c_{GB} at the center of the GB region normalized by the liquidus composition c_L^* as a function of undersaturation ΔM. The lines are Bezier curves intended to highlight the trends.

centered at $z = 0$. It was then represented by a continuous profile by linear interpolation between the bin centers.

Examples of composition profiles are shown in Fig. 3.24 for the $\Sigma 5$ GB at 1000 K for a set of ΔM values near the solidus (similar profiles were also generated for the $\Sigma 17$ and $\Sigma 13$ GBs with similar results).

At early stages of premelting, the profile has a single maximum whose height increases as we move closer to the solidus line. At some point, the maximum overshoots the liquidus composition. Then, instead of growing higher, the peak begins to widen, forms a plateau, and then splits into two local maxima on either side of a local minimum forming at $z = 0$. The composition at this minimum decreases and becomes slightly below c_L^*. Although it was not possible in this work to probe the states even closer to the solidus, we expect that c_{GB} later increases and eventually approaches c_L^* as the grain composition reaches the solidus line. This evolution of the composition profiles is consistent with the formation of two solid-liquid interfaces bounding a liquid layer. The two maxima are associated with the principal peaks of the compositional oscillations created by the solid-liquid interfaces (cf. Fig. 3.4), whereas the minimum in between is a superposition of the depletion zones existing next to the principal peaks. This superposition can explain the slight undershoot

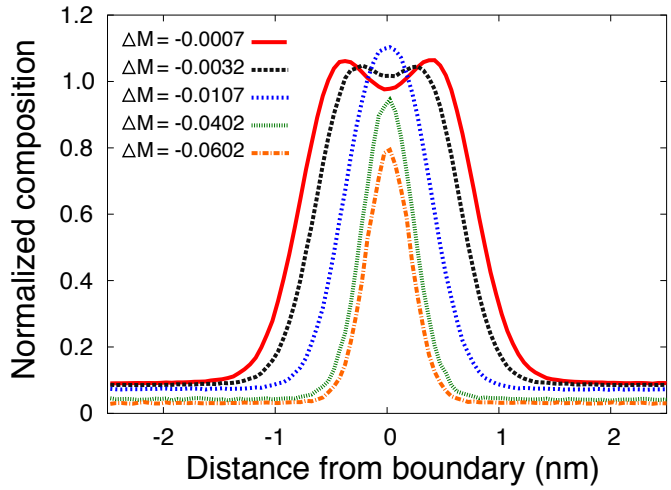

Figure 3.24: Chemical compositional profiles (normalized by the liquidus composition c_L^*) across the $\Sigma 5$ GB for different undersaturations ΔM (eV) at the temperature of 1000 K.

of c_{GB} (Figs. 3.23 and 3.24). When the GB is narrow, the principal peaks merge into a single peak and amplify each other, giving rise to the compositional overshoot discussed above.

The chemical composition of the GBs can also be characterized by the total amount of segregation, $\tilde{N}_2/A$, per unit GB area. Examples of the computed segregation isotherms are shown in Fig. 3.25.

The isotherms remain nearly linear until the grain composition approaches the solidus line, at which point the segregation rapidly accelerates and diverges to infinity. This behavior closely correlates with the divergence of the GB width (Fig. 3.17), which is expected given that the composition inside the GB becomes nearly constant (and close to the liquidus composition) and therefore $\tilde{N}_2/A \propto w$.

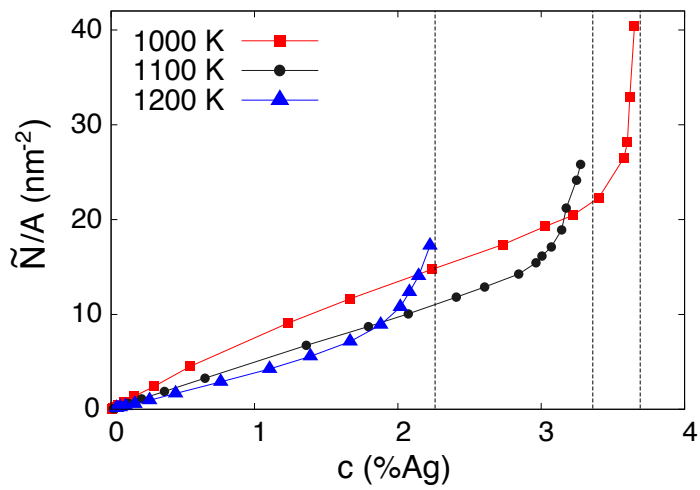

Figure 3.25: Segregation isotherms for the Σ17 GB at three temperatures. The vertical dashed lines mark the solidus compositions c_S^*.

3.3.2.3 Free energy of premelted grain boundaries

To compute the GB free energies, we applied the thermodynamic integration scheme based on the equation [44]

$$\gamma(c) = \frac{A_p}{A}\gamma_p + \int_0^c \left[-\frac{\tilde{N}_2}{A}\left(\frac{dM}{dc}\right)_T + \sum_{i=1}^{2}\tau_{ii}\left(\frac{de_{ii}}{dc}\right)_T \right] dc, \quad \text{fixed } T. \tag{3.38}$$

(The original equation [44] has been modified by changing the integration variable from M to c.) Here, γ_p and A_p are the free energy and cross-sectional area of the GB in the pure Cu state ($c = 0$), which are known from the calculations reported in Sec. 3.3.1.2. The properties appearing in the integrand were discussed in Sec. 3.2.5. The segregation term plays the dominant role while the interface stress term makes a small correction. The integration in Eq.(3.38) was performed numerically.

The functions $\gamma(c)$ are shown in Fig. 3.26 for all three GBs. At a fixed temperature, γ decreases with the solute concentration in the grains, which is consistent with the Gibbs

adsorption equation given that the solute segregation is positive ($\tilde{N}_2 > 0$) and $(dM/dc)_T > 0$. Similar to the pure Cu case, γ_{SL} values were computed for the Σ5 and Σ17 GBs by applying Eq.(3.37) at the point closest to the solidus line. The calculations give the values of 0.161 J/m^2, 0.171 J/m^2 and 0.183 J/m^2 for the Σ5 GB and 0.165 J/m^2, 0.175 J/m^2 and 0.184 J/m^2 for the Σ17 GB at the temperatures of 1000 K, 1100 K and 1200 K, respectively. These numbers are in good agreement with previous calculations (by a different method) for a solid-liquid interface with the (110) orientation [39], which gave the free energies of 0.177 J/m^2, 0.184 J/m^2 and 0.190 J/m^2 at the respective temperatures. A more detailed comparison is shown in Fig. 3.27.

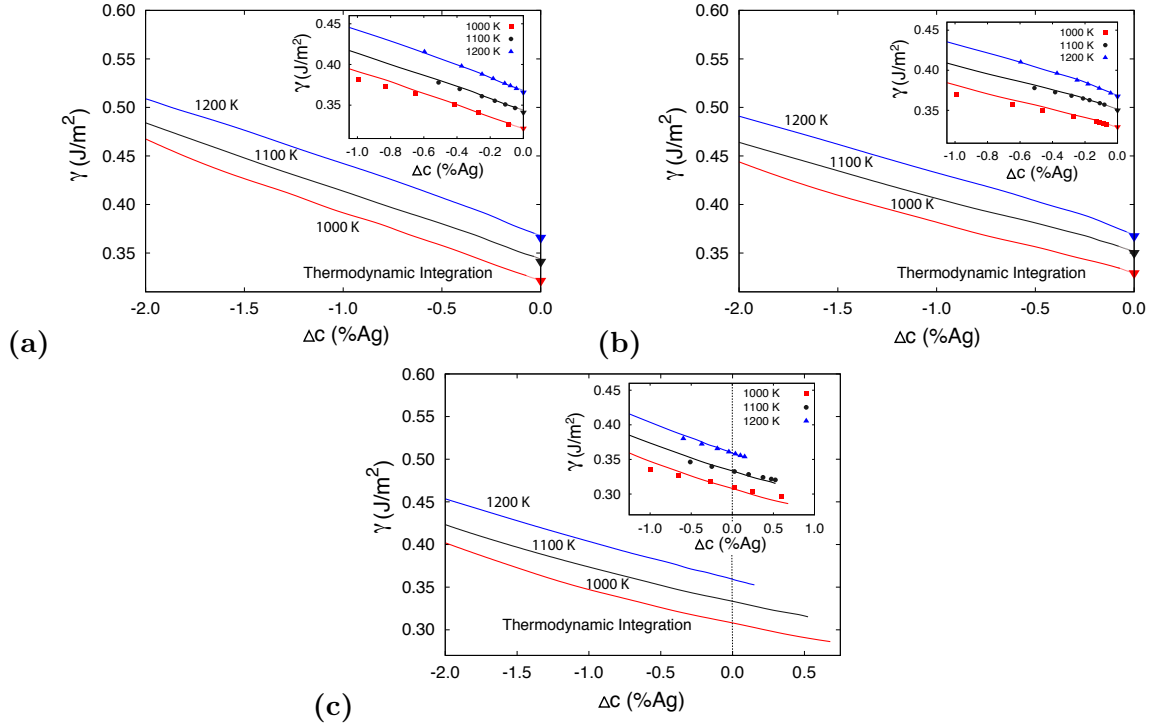

Figure 3.26: Free energy of the (a) Σ5, (b) Σ17 and (c) Σ13 GBs in the Cu-Ag solution at the three temperatures sampled. The solid lines in the main plot were obtained by thermodynamic integration. The dotted lines are linear interpolations to the solidus line ($\Delta c = 0$). The inset compares these results with predictions of the liquid layer model (points) near the solidus.

It is difficult to separate calculation errors from the intrinsic orientation dependence of γ_{SL}. Nevertheless, all calculations indicate that γ_{SL} increases with temperature along the solidus line. This consistency of the results further validates the present methodology. For the sake of completeness, Fig. 3.27 also includes γ_{SL} values obtained by formally applying the same procedure to the $\Sigma 13$ GB (0.172 J/m^2, 0.178 J/m^2 and 0.185 J/m^2 at the temperatures of 1000 K, 1100 K and 1200 K, respectively).

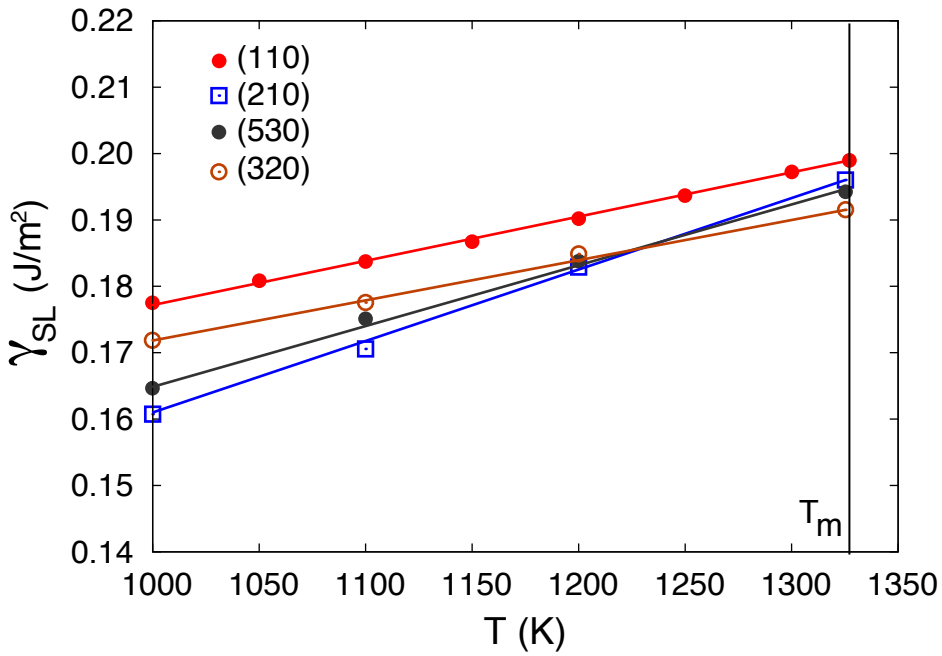

Figure 3.27: Solid-liquid interface free energies in the Cu-Ag system computed in this work from GB premelting simulations. The interface planes are indicated in the legends. For comparison, the plot includes γ_{SL} of the (110) interface computed in previous work.[39]

Surprisingly, the results are consisted with those for the truly premelted GBs, even though this boundary can hardly be represented by a liquid layer. This agreement could be partially fortuitous. Fig. 3.26 also compares the GB free energies γ from thermodynamic integration with calculations of $\bar{\gamma}$ within the liquid layer model using Eqs.(3.34)-(3.36). Recall that γ and $\bar{\gamma}$ are forced to coincidence at the last point of the simulations before the solidus, but all other points are results of independent calculations. Note the good

agreement between the two calculations, especially at 1200 K.

3.4 Conclusions

The proposed analytical form of the disjoining potential describes repulsive, attractive and intermediate interactions between solid-liquid interfaces by a single equation. In contrast to the previously used exponential potentials, Eq.(3.23) captures two physical effects. First, the potential can reproduce two (or more) local minima of the GB free energy and thus stable and metastable GB states separated by a barrier. This, in turn, leads to first order thin-to-thick phase transitions in premelted GBs. Such transitions give rise to GB phase equilibrium lines on bulk phase diagrams that end at a critical point. Such lines were predicted in previous phase field simulations [95, 121, 122]. Second, the potential has an oscillating tail. These oscillations are strongly damped and reflect the existence of spatial oscillations of chemical composition at solid-liquid interfaces (see, e.g., Fig. 3.4). Superposition of these compositional oscillations is expected to produce oscillations of the attraction forces between interfaces. Furthermore, these oscillations might, in principle, produce a whole cascade of thin-to-thick transitions similar to the layering transitions in surface adsorption. Future work may explore if the monolayer, double-layer and other segregation patterns in alloy GBs [37, 38] (often referred to as different "complexions") [21] can also be described by disjoining potentials with oscillating tails.

The atomistic simulations of GBs in binary Cu-Ag solutions conducted in this work have explored various temperatures, chemical compositions and GB energies. The fluctuation approach applied previously to single-component GBs [31, 56] and extended here to binary systems, was applied to extract the disjoining potentials from the simulations under various conditions. All three types of disjoining potentials were found – repulsive, attractive and intermediate, in full agreement with predictions of the liquid layer model with the analytical potential. Multiple consistency checks performed during the simulations demonstrate the reliability of the results. In particular, the GB free energy was computed by thermodynamic integration, producing results consistent with the liquid layer model with the analytical

disjoining potential. Calculations of solid-liquid interface free energies also gave consistent results for different GBs and are in agreement with previous calculations by independent methods.

An important result of the simulations is the confirmation of the existence of multiple stable and metastable states of premelted GBs under appropriate conditions. Such states are characterized by different GB widths as well as other excess properties. During continuous variations of thermodynamic state of the grains, the relative stability of such states varies and at some point can result in a thin-thick phase coexistence. Additional calculations could generate a thin-thick phase coexistence line on the Cu-Ag phase diagram, but this is left for future work.

Chapter 4: Generality of metallic grain boundary phases

In this chapter of the thesis we demonstrate that the multiplicity of GB phases arising from variations in local atomic density, as seen in previous studies [46], is not specific to the $\Sigma 5$ tilt GBs. Indeed the emergence of new GB structures appears to be a generic phenomenon that must take place in almost every GB. The work therefore demonstrates that the atomic density in the GB core must be considered as an additional thermodynamic parameter whose variation can cause structural transformations.

4.1 Simulation methods

Recall that in this thesis we focus on planar symmetric tilt grain boundaries in the FCC crystalline system. Specifically we examine GBs with $(hk0)$ grain boundary planes, a [001] tilt axis, and a grain mis-alignment characterized by the tilt angle θ. Unless otherwise stated we work with Copper as a model FCC system and describe the atomic interactions using an EAM potential [99]. The coordinate system for our simulations was selected so that the x, y, and z directions are respectively aligned to the $[k\bar{h}0]$,$[hk0]$ and [001] crystal directions, i.e. the y direction is always normal to the GB plane and the z direction is always parallel to the tilt axis. The GB structures were generated and minimized in LAMMPS [76] using the standard geometric construction in which the upper grain ($y > 0$) is rotated about the y axis by 180° relative to the lower grain ($y < 0$) [17]. The y-dimension of the simulation block was chosen to be roughly $8\,nm$ for all GBs however for each GB orientation several different cross-sectional areas were sampled. The various cross-sections will be referred to as $n \times m$ where n and m are integers which represent the number of times the minimum possible block lengths were multiplied in the x and z directions respectively. For this system the minimum block lengths consistent with the periodicity of bulk lattice

are $L_x^{min} = \left(h^2 + k^2\right)^{\frac{1}{2}} a_o$, $L_y^{min} = \left(h^2 + k^2\right)^{\frac{1}{2}} a_o$, and $L_z^{min} = a_o$ where a_o is the 0 K lattice constant.

All simulations used periodic boundary conditions in the x and z directions whereas the y dimension of the crystal terminated in an open surface on both ends. Because of this vacuum region the simulation block only contained a single GB located in the center of the block. For a given 0 K structural configuration the grain boundary free energy γ was calculated from Eq.(1.4) where E_{GB} was computed by selecting a subset of atoms centered at the grain boundary ($y = 0$) in a window with a width of roughly $\Delta y = 4\,nm$. The width of this window is chosen so that the ends are deep enough in the bulk phase so that no effects from the GB are present. A schematic of the simulation block and the formation of the window Δy is shown in Fig. 4.1.

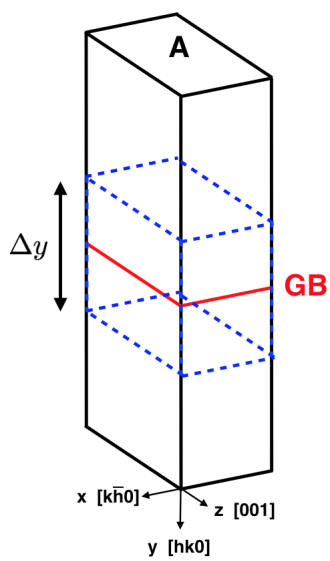

Figure 4.1: Schematic of the simulation block orientation and the geometry of the subset used to calculate the 0K GB free energy for a given configuration.

4.1.1 Fixed GB density minimization

As a starting point we carried out simulations to obtain the minimum energy grain boundary structure for the special case of a GB with a fixed local density and a simulation block which contained the same number of atoms as a prefect crystalline block without any misalignment. This was done using the standard method [17] in which the upper grain ($y > 0$) is translated relative to the lower grain ($y < 0$) by some increment Δx and Δz in the x and z directions respectively. This translation is then followed by a static relaxation using the conjugate gradient method. The process is repeated by looping over a mesh of possible translations. At the end of the loop the the optimal translation corresponding to the lowest energy structure can is obtained.

4.1.2 Variable GB density minimization

In order to study variations in the local GB density it is necessary to either inject vacancies or add new atoms to the simulation block as interstitials. In order to avoid difficulties associated with adding atoms we choose to vary the density by strictly removing atoms rather than adding. For a simulation block with a $n \times m$ cross-section the $(hk0)$ GB plane in the bulk will contain a certain number of atoms which we denote $N_{(hko)}$. The value of $N_{(hko)}$ sets an upper limit on how many atoms need to be removed from the GB. This is because for a particular cross-section removing an entire plane is equivalent to not removing any atoms. Thus for a given cross section we can vary the GB density by removing N_{rm} atoms from the GB core where N_{rm} is an integer in the range $[0, N_{(hko)}]$. This provides a means of quantifying the local GB density. Specifically we define λ as the fraction of the $N_{(hko)}$ plane which has been removed from the boundary region, i.e. $\lambda = \frac{N_{rm}}{N_{(hko)}}$. Simulation blocks with smaller cross-sections have fewer atoms in the $(hk0)$ plane and therefore these blocks sample smaller subsets of the possible values of λ. For this reason we carry out

simulations with several different cross-sections for each GB. We found that the cross-sections $1\times1, 1\times2, 2\times2, 2\times4$ and 3×2 [9] provided an adequate number of sample λ points. These cross-sections corresponded to block sizes ranging anywhere from a few hundred to around 10,000 atoms.

There are many possible ways to search for minimum energy structures by removing atoms from the GB region. In this work we develop a brute force algorithm to address the problem. The general idea of the method is to randomly remove atoms from the GB and then use short MD runs to redistribute the resultant vacancies. During the MD runs we periodically save atomic configurations and at the end we randomly select a subset of these for energy minimization. The advantage of this method is that it is conceptually very simple and only requires the removal of atoms once which dramatically simplifies the process of figuring out which atoms to remove. The details of the method are as follows: For a given GB $(hk0)$ and cross-section $n \times m$ we loop over the set of possible atomic removals $N_{rm} \in [0, N_{(hko)}]$. For each value of N_{rm} we randomly remove the given number of atoms from a region $0.2\,nm$ wide centered at the GB. We then loop over a set of $n_T = 20$ random translations $(\Delta x, \Delta z)$ of the upper grain $(y > 0)$ relative to the lower grain (where $\Delta x \in [0, \left(h^2+k^2\right)^{\frac{1}{2}} a_o]$ and $\Delta z \in [0, a_o]$). For a given translation we define three groups, top, middle, and bottom within the simulation block. These groups are defined by partitioning the block only in the y dimension, i.e each region encompasses the entire cross section similar to what is shown Fig. 4.1. The boundaries of the groups are given by $y_{bottom} \in [-\infty, -l]$,$y_{middle} \in [-l, l]$ and $y_{top} \in [l, \infty]$ where l was chosen to be $0.4\,nm$. The atoms in the bottom group don't move throughout the MD run and remain fixed in their 0K positions. The GB atoms in the center group undergo an NVT molecular dynamics run in which the temperature is ramped from room temperature up to 85% of the melting temperature and then back down to $0K$, each MD run is 150,000 steps using

[9] For the $\Sigma5(210)$ and $\Sigma5(310)$ boundaries we used larger cross-sections than used for the other boundaries. This was done to facilitate comparison with the plots from Ref.[46] and to ensure that our curves had a comparable number of points as those in the previous work which also focused on the two $\Sigma5$ boundaries. Specifically for these boundaries we sampled the following cross sections $1\times2, 1\times6, 2\times4, 2\times7, 2\times11$ and 2×13

a $2\,fs$ time step. Finally the atoms in the top group also remain in their 0 K equilibrium positions however the entire group can move as a rigid body. This allows the upper grain to relieve normal stress from the thermally active GB atoms as well as translate in the x and z directions. The gliding behavior of the upper grain allows the system to refine the initial random translation and find a more energetically favorable relative locations. During NVT runs we could have allowed all atoms to move however our method constrains the GB by keeping it in contact with the 0 K crystal and saves time on the quench due to the fact that most atoms are still in their 0 K positions. Because we do not allow for thermal expansion of the in-plane directions the NVT run has some level of residual stress at the elevated temperature but this vanishes after the subsequent 0 K minimization. During the MD run 1500 snapshots are saved for each cross section and each value of N_{rm}, i.e. 75 snapshots per translation. From the 1500 snapshots we randomly select 250 to be minimized using the conjugate gradient method and keep the lowest energy result. If the algorithm works correctly then the output gives the minimal structural energy associated with a given value of λ. By sampling a set of λ values we obtain the function $\gamma(\lambda)$ for each GB. This function is the primary result obtained in this work. One noteworthy property of this method is that it can be easily parallelized because the MD runs and 0 K minimizations can be carried our independently. Finally during the MD portion of the algorithm we are only interested in rearranging the vacancies and therefore one could potentially speed the algorithm up by increasing the time step to higher than usual values. In the present study however we elected to used a conventional $2\,fs$ time step.

4.2 Fixed GB density results

In this work we studies a total of twelve symmetric tilt grain boundaries over a wide range of tilt angles. As described in Sec. 4.1.1 we first carried out minimizations for the special case of a GB with a fixed density, specifically $N_{rm} = 0$ and $\lambda = 0$. This was done by looping over a set of rigid translations to find the optimal relative displacement of the upper and lower grains. We find that for all of the GBs studied using the fixed density method the

minimal energy configurations are networks of a common structural unit which we denote as type K (kite). These structural units are well known in the literature [17]. In Fig. 4.2 we provide images of a subset of the regular kite structures obtained using this method. This figure is included so the reader can compare with the non-regular kite structures in the subsequent sections.

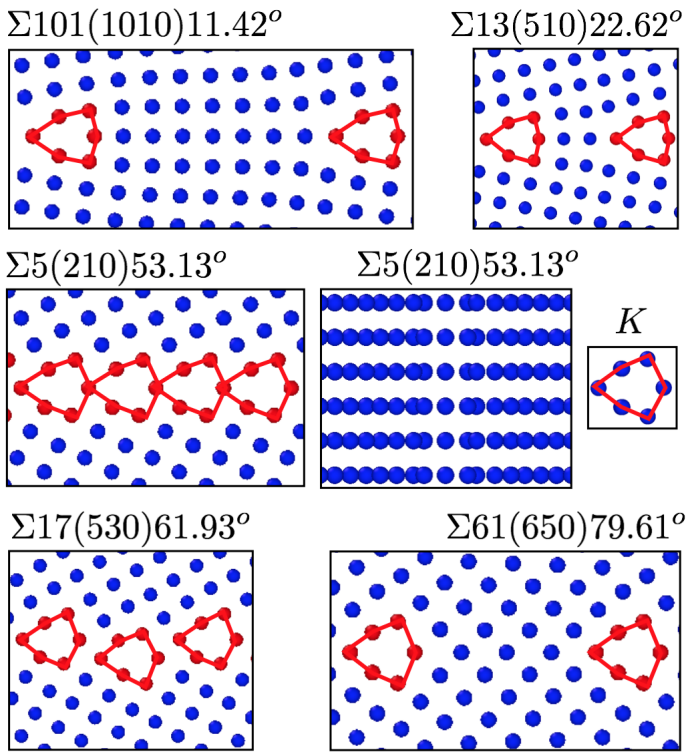

Figure 4.2: Here we show a subset of the results for the special case in which the GB density is fixed ($N_{rm} = 0$). Using the "translate and minimize" method the minimum energy structures appears to be networks of regular kite units no matter how large or small the tilt angle is. The images which show the kite structure are taken by projecting the simulation block down the [001] tilt axis however the center right images shows a projection down the $[1\bar{2}0]$ direction (the $[k\bar{h}0]$ projection for all other regular kite boundaries is similar to the one shown)

In Tab. 4.1 we provide a list the various GBs sampled in this work as well as the GB energies which arise when the boundaries take the form of networks of regular kites. These

energies are in good agreement with those in ref.[17] which studied the same set of GBs using the same EAM potential as in the current study.

Table 4.1: Here we provide a list of the various boundaries sampled in this work as well as the energies of these boundaries when they take the form of networks of regular kites

Boundary	θ	γ_{gb} (Jm^{-2}) (regular kites)
Σ101(1010)	11.42^o	0.686
Σ25(710)	16.26^o	0.796
Σ37(610)	18.92^o	0.837
Σ13(510)	22.62^o	0.878
Σ17(410)	28.07^o	0.914
Σ53(720)	31.89^o	0.939
Σ5(310)	36.87^o	0.905
Σ5(210)	53.13^o	0.951
Σ17(530)	61.93^o	0.856
Σ13(320)	67.38^o	0.790
Σ25(430)	73.74^o	0.677
Σ61(650)	79.61^o	0.533

4.3 Variable GB density results

4.3.1 Structural units

In this work three distinct structural units were found which could describe all of the various GBs analyzed. Projections of these units down the [001] tilt axis are shown in in Fig. 4.3. These include the well-known kite-shaped structural unit discussed in the previous section and two additional units which were referred to in [37, 46] as split kites and filled kites. For brevity, we will call these structural units K, L and M, respectively, and will symbolize them by a diamond, a square, and a circle.

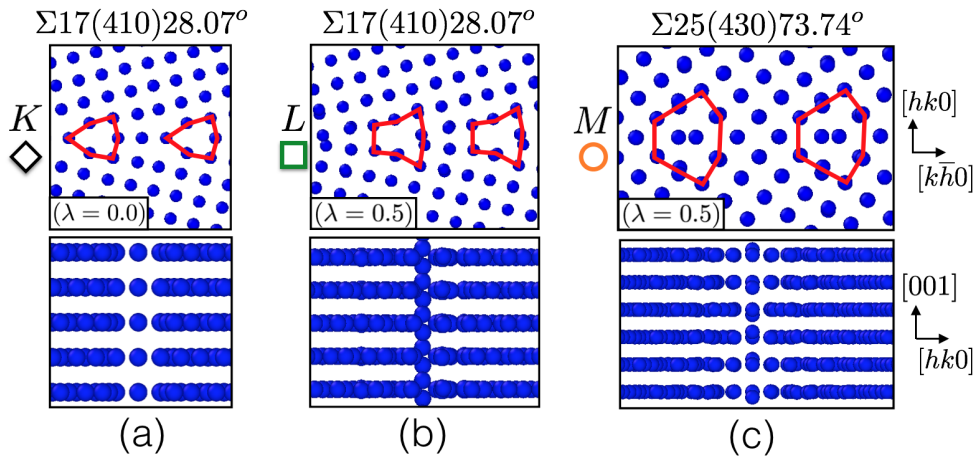

Figure 4.3: Structural units (a) K, (b) L and (c) M found in [001] symmetrical tilt GBs in Cu. The structures are projected parallel to the [001] tilt axis (upper row) and normal to the tilt axis (lower row). The GB density λ are indicated.

4.3.2 Validation of methodology

We first tested our algorithm on the two $\Sigma 5$ boundaries. This was done to ensure that our method was effectively finding the minimum energy structures. The functions $\gamma(\lambda)$ for the $\Sigma 5$ boundaries are known to have additional minima for value of $\lambda \neq 0$ [37, 46]. In the previous studies it was shown that at 0 K the $\Sigma 5(210)$ boundary has three minima obtained when λ is roughly 0, 0.53 and 0.14. These configurations respectively correspond to structural units K, L and M and have free energies $0.951, 0.936$ and $0.953\ Jm^{-2}$. Additionally it was shown that the $\Sigma 5(310)$ boundary has two minima occurring when λ is roughly 0 and 0.6. These structures respectively had energies 0.9047 and 0.911 Jm^{-2}. In Fig. 4.4 we show our results for the 0 K $\gamma(\lambda)$ curves for these two boundaries and include selected representative structures for the two $\Sigma 5$ GBs. Using our method we obtain results which are in excellent agreement with the previous studies [37, 46]. In particular show Fig. 4.4 that for the $\Sigma 5\,(210)$ GB the L units connect to each other head to tail to produce a more favorable structure than the standard K units [37, 46].

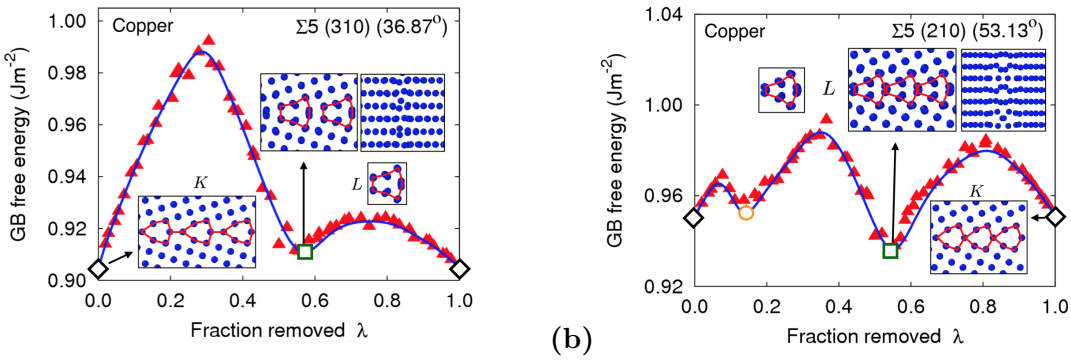

Figure 4.4: In this figure we show our results for the two Σ5 boundaries. a) (310) boundary and b) (210) Notice that in both grain boundaries the split kite structures emerge near the center of the curves whereas in the (210) boundary there is an additional local minima around $\lambda = 0.14$ which is associated with filled kites. For the various minima we show images of the kite structures which are projections down the [001] tilt axis. For the split kites we also include images projected down the $[k\bar{h}0]$ directions. The blue lines running through the points are bezier curves included as a guide for the eye.

Because we are only interested in the minimum possible values of γ as a function of λ we carry out a procedure in which we use a moving window (window width $\Delta\lambda \approx 0.05$) to scan across the raw data and extract a curve which gives the minimum envelope of the raw data (the window moves in discrete steps of size $\Delta\lambda$). This is done by only keeping the minimum value of γ within a given position of the moving window. This effectively extracts a curve associated with the minimum values obtained from our algorithm and removes higher energy outliers. This procedure is carried out for all $\gamma(\lambda)$ curves presented in this work and an example of the result of this procedure is shown in Fig. 4.5 for the (210) boundary. For the lower angle boundaries (relative to $\theta = 0^o$ and 90°) the results of this procedure are more dramatic because the data tends to have more scatter however the result is the same.

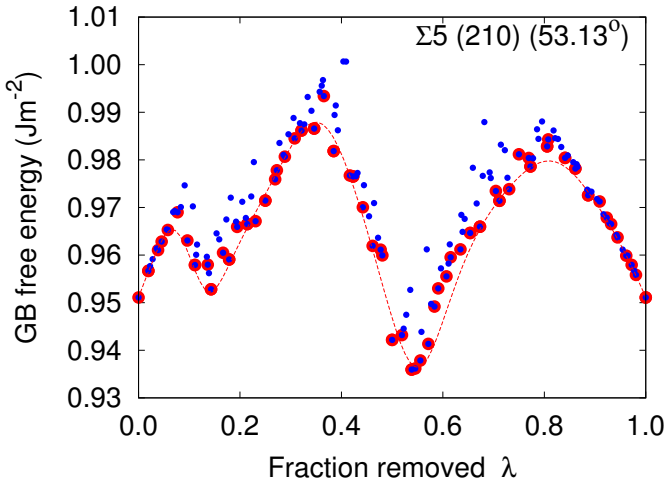

Figure 4.5: The results of the moving window procedure discussed in the text for the case of the (210) boundary. The blue points are the raw data and the red points are the minimum values chosen by the moving window procedure. The line in the plot are bezier curves fitted to the red points and is included as a guide for the eye

4.3.3 Additional results

In this section we provide a summary of the rest of the results obtained in this work, specifically in Fig. 4.6 we provide a subset of the various $\gamma(\lambda)$ which were calculated. A complete catalog of the $\gamma(\lambda)$ curves and structures corresponding to local and global minima can be found in the appendix of this work. Low-angle GBs form when θ is small and when it is close to 90°. In the first case, the GB represents an array of dislocations running parallel to the tilt axis. Standard energy minimization without adjusting the GB density predicts that the dislocation cores are composed of K units. However, Fig. 4.6(a) presents an example where this structure is, in fact, *not* the ground state. If λ is allowed to vary, γ is reduced by removing an equivalent of a half-plane ($\lambda = 0.5$) and forming a new structure composed of L units. In fact, even if the GB density remains fixed at the initial value ($\lambda = 0$), our calculations show that the structure composed of K units is still not the ground state. This structure is metastable and is shown in Fig. 4.6(a) by a diamond symbol.

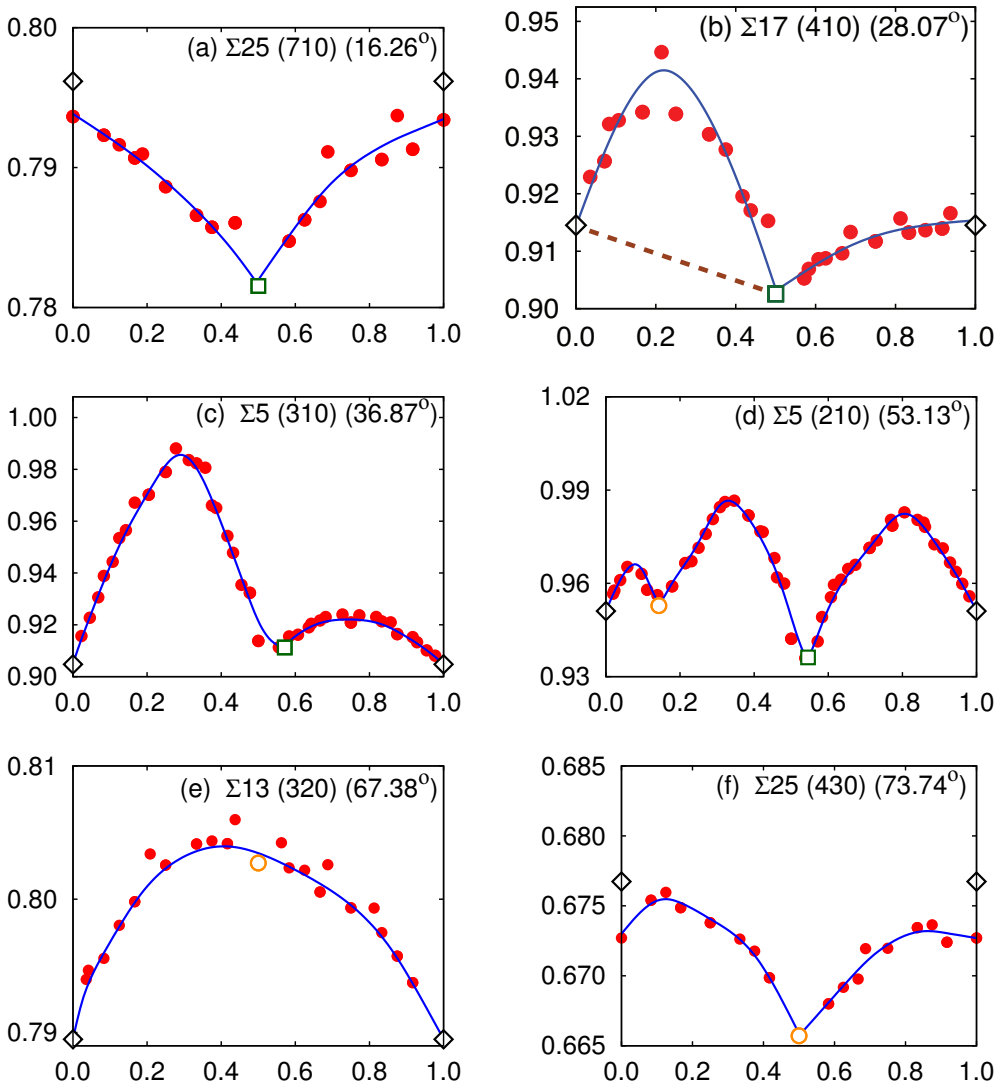

Figure 4.6: GB energy (in $\mathrm{J\,m^{-2}}$) versus GB density λ (fraction of atoms removed) for representative symmetrical tilt GBs in Cu. For GBs composed on identical structural units, the data points are shown by symbols representing the respective structural units (◇ K, □ L, ◯ M, see Fig. 4.3). The diamond symbols in (a) and (f) represent metastable structures composed structural units K. All other points represent stable structures that minimize the GB energy for each density λ. The dashed line in (b) is an example of a tie line between two GB phases producing cups of the energy. The trend lines are shown as a guide to the eye.

A more favorable structure is composed of alternating L-type and K-type units arranged in the pattern ...-L-L-K-L-L-K..., where the dash indicates that the units are separated

several elastically distorted perfect-lattice units. Of course, due to the conservation of atoms, these K and L units contains some defects such as extra atoms or structural vacancies. This example clearly demonstrates the importance of displacing GB atoms over large distances when searching for the energy minimum. The widely accepted procedure when the energy is minimized with respect to local atomic displacements can easily miss low-energy structures (even if grain translations are applied).

The example in Fig. 4.6(a) is for $\theta = 16.26°$. The same behavior pertains to smaller angles. But as θ increases, the structure composed of K units becomes increasingly more favorable and eventually becomes the ground state at $\lambda = 0$ [Fig. 4.6(b)]. Nevertheless, the L unit structure appearing at $\lambda = 0.5$ remains even more stable. This trend continues until the angle reaches $\theta = 36.87°$. At this point, the L unit structure becomes slightly less favorable than the standard K units [Fig. 4.6(c)].

For the low-angle boundaries near $\theta = 90°$, the lowest-energy structure is again found at $\lambda = 0.5$ [Fig. 4.6(f)]. This time it consists of the structural units M [Fig. 4.3(c)]. The structure obtained by the conventional method ($\lambda = 0$) is composed of K units [17] and is less favorable than an array of distorted M units. This confirms again the importance of large atomic displacements during the energy minimization. As the angle decreases, the K units become more stable while the M units less stable. At angles below about 70°, the K unit structure becomes the ground state, whereas the structure composed of M units becomes the least favorable one (the energy peaks at $\lambda = 0.5$) [Fig. 4.3(e)]. As θ decreases further, the behavior becomes more complex. As the M units come closer together, their interaction apparently becomes attractive. When the angle reaches 53.13° corresponding to the $\Sigma 5\,(210)$ GB, the M units form a compact array found in the previous work [37, 46], where the units are connected head to tail. This energetically favorable structure creates a local minimum [Fig. 4.6(d)]. As a result, the $\Sigma 5\,(210)$ GB features three energy minima corresponding to three structures composed of the units K, L and M, respectively.

This analysis demonstrates that λ is a critical parameter controlling the structure and energy of GBs. Variations in λ cause a structural evolution in GBs that can be described

in terms of the structural unit model [118] if the mis-orientation angle is replaced by λ[10]. There is a small number of special structural units that constitute the building blocks of a series of boundaries. There are intervals of angles (respectively, λ values) in which the GB represents an array of two types of structural unit. For the set of GBs studied here, such basic structural units have been identified as K, L and M.

The function $\gamma(\lambda)$ (Fig. 4.6) has a thermodynamic meaning similar to the composition dependence of molar Gibbs energy in bulk thermodynamics. The same common tangent construction can be applied to predict the coexistence of different GB phases and their "compositions" λ[11]. When the energy minima are cusps, the common tangent is replaced by a tie line passing through the minimum points [Fig. 4.6(b)]. Coexistence of GB phases has indeed been observed in the recent atomistic simulations of $\Sigma 5$ GBs [45]. In both the present work and [37, 46], the GB cross-sections were kept relatively small. The imposed periodic boundary conditions stabilized the metastable and unstable states of the boundaries, enabling the construction of continuous $\gamma(\lambda)$ plots such as Fig. 4.6 (also see this works appendix). As the cross-section increases, the boundary will eventually break into single-phase regions separated by a one-dimensional phase boundary [36, 45][12]. The common tangent construction does not apply to the frequently used $\gamma(\theta)$ plots since the angle does not constitute an additive variable. Such plots are suitable for predicting GB dissociation transitions [16], but the geometric construction is then different from the common tangent. Nevertheless, it is instructive to plot $\gamma(\lambda, \theta)$, as in Fig. 4.7. While the energy of low-angle GBs depends primarily on the angle, for high-angle GBs both variables are equally important.

[10]The structural unit model [117, 118] has some intrinsic problems, such as the ambiguity in the choice of delimiting boundaries, and is not always borne out by experiments and simulations. Here, we only refer to the general ideas of this model, such as the existence of a small number of basic structural units forming the GBs.

[11]In this work, such predictions can only be made at low temperatures since γ is the GB energy and not free energy.

[12]In fact, we cannot exclude that the mixtures of structural units found in some of the low-angle GBs at $\lambda = 0$ represent early stages of separation in two phases composed of units K and/or L (receptively, M near $\theta = 90°$).

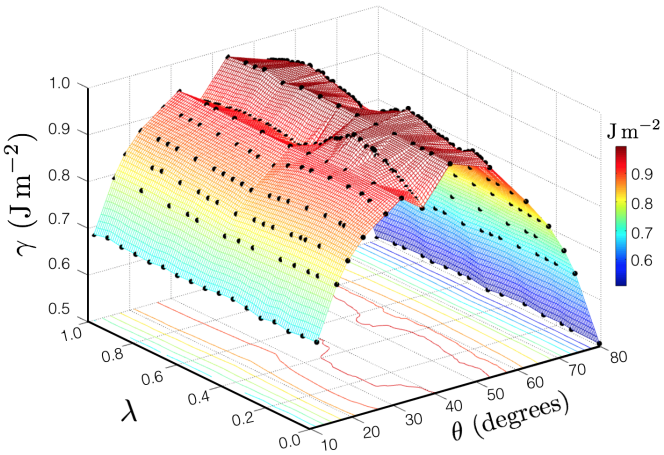

Figure 4.7: GB energy as a function of GB density λ and misorientation angle θ for [001] symmetrical tilt boundaries in Cu. The actual simulation points are indicated.

4.3.4 Silver and Aluminum results

It is natural to question whether these results are unique to copper or are a more general feature of FCC metals. This was addressed in Ref.[46], in that work the authors generated 0K curves for the (210) boundary using potentials for Gold, Silver, Copper and Nickel. In all cases it was seen that the curve shapes were qualitatively similar to copper. For Au,Ag and Cu the split kites were seen to be the lowest energy structure however in Ni regular kites were energetically more favorable. To see the effect that material has on our results we reapplied our method to the (210) and (410) boundaries in both silver and aluminum again using EAM potentials [131]. In Fig. 4.8 we show $\gamma(\lambda)$ for silver, just as in the previous work [46] the (210) boundary behaves nearly identically to copper, the same is true for the (410) GB which suggests a generality of our results for all noble FCC metals.

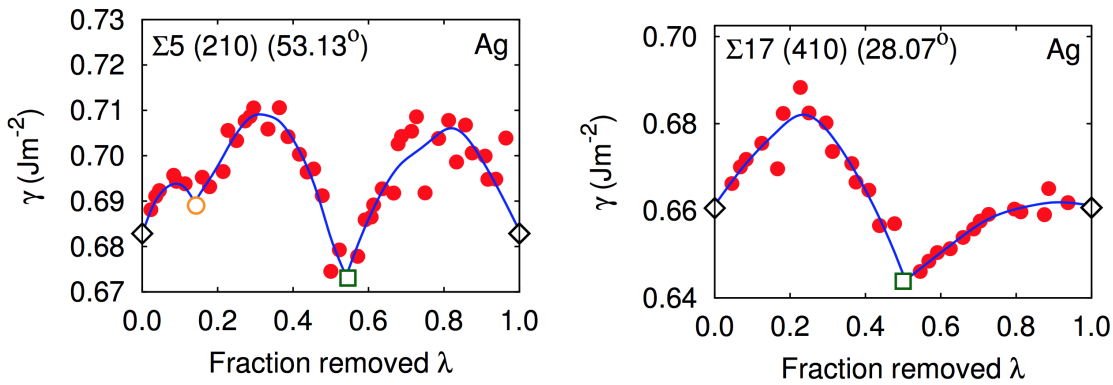

Figure 4.8: GB energy (in J/m^2) versus GB density λ (fraction of atoms removed) for symmetrical tilt GBs in Ag.

For Al [96], the general trends were found to be similar but some differences emerged. For example, for the $\Sigma 17\,(410)$ GB, the energy minimum at $\lambda = 0.5$ corresponding to the L unit structure [cf. Figs. 4.6(b)] becomes a maximum [Fig. 4.9(a)]. The most favorable structure that was found at $\lambda = 0.5$ is now an array of highly defected K units, whereas the L unit structure has a slightly higher energy. For the $\Sigma 5\,(210)$ GB in Al [Fig. 4.9(b)], the two minima are replaced by one at $\lambda = 0.5$. The respective GB structure is composed of M units connected head to tail [Fig. 4.9(c)]. This combination of M units was not seen in Cu. Further tests for other metals are warranted, but it is already evident that the specific GB structures and their relative energies may be material-dependent.

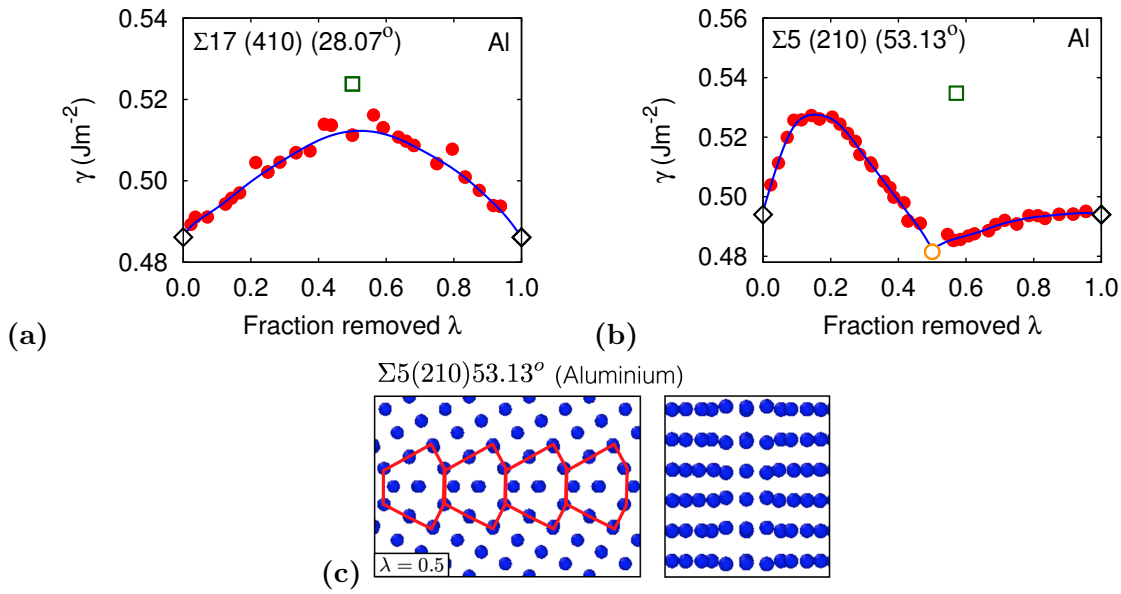

Figure 4.9: GB energy versus GB density λ (fraction of atoms removed) for (a) $\Sigma 17\,(410)$ and (b) $\Sigma 5\,(210)$ GBs in Al. The trend lines are shown as a guide to the eye. The most stable structure of the $\Sigma 5\,(210)$ GBs is composed of M units as shown in (c).

4.4 Conclusions

In summary, we have extended the previous studies of the $\Sigma 5$ GBs [36–38, 46] to a larger set of [001] symmetrical tilt GBs in order to evaluate the generality of the previous findings. The GB structures and energies have been calculated by allowing variations in the GB density λ and large displacements of atoms during the energy minimization. The results confirm the existence of stable and metastable GB phases over the entire range of misorientation angles. The GBs contain arrays of structural units that follow a systematic behavior that can be rationalized in therms of the structural unit model [118]. Each of the GBs is composed of one or two types of structural unit, usually separated by a few perfect-lattice units. λ should be included in the descriptions of GBs as an additional parameter capable of predicting GB phases and phase transformations.

Chapter 5: Canonical ensemble temperature fluctuations

In Sec. 1.2.1 we denoted the fluctuated energy in the canonical system as $E(t)$. In the present discussion we will drop the argument and just express this quantity as E to simplify the notation. Additionally the different points of view concerning canonical temperature fluctuations were briefly discussed in Sec. 1.6 however we will re-iterate them here in more detail, the different perspectives are as follows:

(i) Temperature fluctuations in canonical systems is a real physical phenomenon and can be measured experimentally [22]. If the volume and number of particles in the system are fixed, then [19, 70, 93]

$$\left\langle (\Delta T)^2 \right\rangle = \frac{kT_0^2}{Nc_v^0}, \tag{5.1}$$

where $\Delta T = T - T_0$ is the deviation of the system temperature T from the thermostat temperature T_0, c_v^0 is the constant-volume specific heat (per particle) at the temperature T_0, and k is Boltzmann's constant. As mentioned in Sec. 1.2.1, the angular brackets $\langle ... \rangle$ indicate the canonical ensemble average.[13] Spontaneous energy exchanges between the system and the thermostat bring the system to quasi-equilibrium states in which the temperature is slightly higher or slightly lower than T_0. It is also possible to quantify the cross-correlation between the fluctuating temperature and the system's total energy by the equation [19, 70, 93]

$$\langle \Delta E \Delta T \rangle = kT_0^2, \tag{5.2}$$

where $\Delta E = E - E_0$ and E_0 is the equilibrium energy.

[13] By contrast, the temperature T appearing in Eq.(5.1) is defined by averaging over much shorter segments of the trajectory as discussed later in the chapter.

(ii) Temperature of a canonical system is *defined* as the temperature of the thermostat. Thus, $T \equiv T_0$ by definition and the very notion of temperature fluctuations is meaningless [63–65].

(iii) While fluctuations of the system energy E are well-defined, non-equilibrium temperature T is ill-defined [64, 126]. One can *formally* define T as $T \equiv T_0 + (E - E_0)/(Nc_v^0)$, which makes T just a nominal parameter identical to energy [126]. From this point of view, Eq.(5.1) contains no new physics in comparison with the well-established energy fluctuation relation [19, 70, 93]

$$\left\langle (\Delta E)^2 \right\rangle = NkT_0^2 c_v^0. \tag{5.3}$$

(iv) Even for an equilibrium *isolated* system, temperature is not a well-defined parameter. It can be evaluated by measuring the system energy and trying to estimate the temperature of the thermostat with which the system was in equilibrium before being disconnected [30, 84]. This reduces the temperature definition to a statistical problem addressed in the framework of the estimation theory. The statistical uncertainty associated with the temperature estimate can be interpreted as its "fluctuation".

As an operational definition, the non-equilibrium temperature is identified in the present study as the kinetic energy of the particles averaged on an appropriate timescale. In Sec. 5.1 we set the stage by reviewing the thermodynamic arguments [19, 70, 93] and introducing three timescales of the problem that permit a clear definition of non-equilibrium temperature. After presenting the simulation methodology in Sec. 5.2, we report on MD results for the kinetic, potential and total energy fluctuations and the respective correlation functions for the solid (Sec. 5.3). Using this data, we are able to extract the temperature fluctuations and verify Eqs.(5.1) and (5.2) *independently* of Eq.(5.3). In Sec. 5.4 we summarize the results of this work and formulate conclusions.

5.1 Theory

We briefly introduced the canonical ensemble in Sec. 1.2.1 however we will revisit the concept here in a more rigorous way with special attention to the timescales associated with different processes. If a thermodynamic system is disconnected from its environment and becomes isolated, it reaches thermodynamic equilibrium after a characteristic relaxation time τ_r. Suppose the isolated system is still in the process of relaxation. While E, V and N are fixed, other thermodynamic properties can vary. If we mentally partition the system into relatively small subsystems, their parameters E, V and N can vary during the relaxation. It is important to recognize that the relaxation time t_r of a small subsystem is much shorter than τ_r of the entire system, at least for short-range interatomic forces. Thus, there is a certain timescale t_q such that

$$t_r \ll t_q \ll \tau_r, \tag{5.4}$$

on which the small subsystems remain infinitely close to equilibrium, even though the entire system is not in full equilibrium. The subsystems weakly interact with each other across their interfaces, causing a slow drift of the entire system towards equilibrium. Such virtually equilibrium subsystems are called *quasi-equilibrium* [93] and the entire isolated system is said to be in a quasi-equilibrium state.[14] On the quasi-equilibrium timescale t_q, the isolated system can be thought of as equilibrated in the presence of isolating walls separating its small subsystems. Accordingly, each quasi-equilibrium subsystem α can be described by a fundamental equation $S_\alpha = S_\alpha(E_\alpha, V_\alpha, N_\alpha)$, from which the local temperature, pressure and chemical potential can be found by $T_\alpha = 1/(\partial S_\alpha/\partial E_\alpha)$, $p_\alpha = T_\alpha(\partial S_\alpha/\partial V_\alpha)$ and $\mu_\alpha = -T_\alpha(\partial S_\alpha/\partial N_\alpha)$, respectively. If the number of subsystems is large enough, we can talk about spatially continuous temperature, pressure and chemical potential fields. Such fields appear in the standard treatments of irreversible thermodynamics [87] and are only defined on the quasi-equilibrium timescale. They evolve during the relaxation process and eventually become uniform when the entire system reaches equilibrium.

[14] Landau and Lifshitz [70] call the quasi-equilibrium states "quasi-stationary", which may cause some confusion since the term "stationary" is often used to describe steady-state flows in driven systems.

Following the fluctuation-dissipation concepts [20, 67, 70, 85, 101, 103, 104], one can expect that similar quasi-equilibrium states arise during equilibrium fluctuations in an isolated system. Accordingly, the fluctuated states can be described by well-defined local values of the intensive parameters, including temperature. Again, such local intensive parameters are only defined on the quasi-equilibrium timescale t_q.

Turning to canonical fluctuations, consider a small subsystem of an equilibrium isolated system. Let us call this subsystem a system and the rest of the isolated system a reservoir. Consider a timescale t_q such that $t_r \ll t_q \ll \tau_r$, where t_r is the relaxation time of the system and τ_r is the global relaxation time of the system plus reservoir. On this timescale, the system can be considered as quasi-equilibrium and thus virtually isolated. As such, it possess all intensive properties mentioned above. Fluctuations generally occur on all timescales. However, if we monitor the system properties averaged over the timescale t_q, then we can talk about fluctuations of its intensive parameters. In particular, quasi-equilibrium fluctuations that preserve the system volume and number of particles (canonical ensemble) include well-defined temperature fluctuations. As long as the temperature is properly defined on the quasi-equilibrium timescale, it will satisfy the fluctuation relation (5.1).

We next apply these concepts to a crystalline solid comprising a fixed number of atoms $N \gg 1$. The local relaxation timescale t_r can be identified with a typical phonon lifetime. Suppose the solid is isolated and in equilibrium. Its instantaneous potential energy U and kinetic energy of the centers of mass of the particles K fluctuate whereas the total energy $E = K + U$ is strictly fixed. The timescale t_K of the kinetic (as well as potential) energy fluctuations is the inverse of a typical phonon frequency $\bar{f}$: $t_K \sim 1/\bar{f}$. Assuming that the solid is nearly harmonic, this timescale is much shorter than t_r. The temperature of the solid is fixed at $T = E/3k$ and can be evaluated from the equipartition relation $\langle K \rangle = 3NkT/2$ by monitoring the kinetic energy over a long time $t \gg t_r$.

If the same solid is now connected to a thermostat, two types of fluctuation occur. First, the same fluctuations as in the isolated system, including the energy exchanges between the phonon modes on the t_r timescale. Second, there will be fluctuations in the total energy

of the solid due to energy exchanges between the solid and the thermostat. The two types of fluctuation are governed by physically different relaxation processes: phonon scattering inside the solid in the first case and heat flow between the solid and the thermostat in the second. The respective relaxation times, t_r and τ_r, are significantly different. Usually $\tau_r \gg t_r$, i.e., the energy exchanges with the thermostat occur on a much longer timescale that depends on the system size, the system/thermostat interface and other factors. Thus, there is a timescale t_q in between, $t_r \ll t_q \ll \tau_r$, on which the solid remains quasi-equilibrium and can be assigned a well-defined temperature. We can use the equipartition relation to find this quasi-equilibrium temperature,

$$T = \frac{2\langle K \rangle_q}{3Nk}, \tag{5.5}$$

where the subscript q indicates that the time average must be taken on the quasi-equilibrium timescale t_q.[15]

If the kinetic energy is averaged over the thermodynamic timescale $t \gg \tau_r$, then the equipartition relation trivially gives the thermostat temperature

$$T_0 = \frac{2\langle K \rangle}{3Nk}. \tag{5.6}$$

By contrast, the quasi-equilibrium temperature defined by Eq.(5.5) fluctuates around T_0 and is predicted to satisfy the fluctuation formula (5.1). We emphasize that Eq.(5.5) defines T independently of the instantaneous or average values of the total energy and makes no reference to the specific heat of the substance.[16] Instead, the temperature fluctuations can

[15]The reader is reminded that $\langle ... \rangle$ is the time average over a very long trajectory of the system in the phase space. By default, the time averaging is performed in the canonical ensemble (NVT); otherwise the ensemble is indicated as a subscript. For example, in Sec. 5.3.1 we discuss the time average $\langle ... \rangle_{NVE}$ computed in the micro-canonical (NVE) ensemble. Some observables are averaged over many time intervals of the same finite length (say, θ). This is indicated in the subscript, e.g., $\langle ... \rangle_\theta$. $\langle ... \rangle_q$ denotes the time average over a finite time interval on the quasi-equilibrium timescale t_q.

[16]For example, for a molecular solid the rotational and vibrational degrees of freedom contribute to c_v^0 but do not appear in Eq.(5.5), which only includes the kinetic energy of the centers of mass.

be used to *extract* the specific heat c_v^0. For a classical harmonic solid composed of atoms (not a molecular crystal), $c_v^0 = 3k$ and Eq.(5.1) becomes

$$\left\langle (\Delta T)^2 \right\rangle = \frac{T_0^2}{3N}. \tag{5.7}$$

The key point of this treatment is that the kinetic energy of the centers of mass of the particles must be averaged over the appropriate timescale. We caution against using the "instantaneous temperature" defined by the instantaneous value of the kinetic energy as $\hat{T} = 2K/3Nk$, as is often done in the MD community. The "temperature" $\hat{T}$ so defined essentially represents the kinetic energy K/N itself up to units. Although this unit conversion can sometimes make the MD results look more intuitive, it fails to predict the correct temperature fluctuations. Using the standard canonical distribution, it is easy to show that for any classical system [72]

$$\left\langle (\Delta K)^2 \right\rangle = \frac{3N(kT_0)^2}{2}, \tag{5.8}$$

from which

$$\left\langle (\Delta \hat{T})^2 \right\rangle = 2\frac{T_0^2}{3N}. \tag{5.9}$$

For an atomic solid, this equation is off by a factor of two. Consequently, the specific heat of the solid extracted from Eq.(5.1) using the "instantaneous temperature" $\hat{T}$ is $3k/2$ instead of the correct $3k$.

In spite of the failure of the "instantaneous temperature" $\hat{T}$ to describe the mean-square fluctuation of temperature, it does satisfy some other fluctuation relations, including Eq.(5.2) which then becomes $\left\langle \Delta E \Delta \hat{T} \right\rangle = kT_0^2$. Like the energy variance $\left\langle (\Delta E)^2 \right\rangle$, the covariance $\langle \Delta E \Delta T \rangle$ remains the same for both instantaneous and quasi-equilibrium fluctuations. In the following sections, Eqs.(5.1), (5.2) and (5.3) will be verified by MD simulations with different choices of the thermostat.

5.2 Methodology of simulations

5.2.1 Molecular dynamics simulations

As a model system we chose face-centered cubic copper with atomic interactions described by an embedded-atom potential [99]. The potential accurately reproduces many physical properties of Cu, including phonon dispersion relations. The MD simulations were performed with the LAMMPS code [107] with the time integration step of $dt = 0.001$ ps. Except for the system in a "natural thermostat" discussed later, all simulations were conducted in a cubic simulation block with periodic boundary conditions. The block edge was 7.23 nm and the total number of atoms was $N = 32000$. The block edges were aligned with $\langle 100 \rangle$ directions of the crystal lattice. The simulation temperature was chosen to be $T_0 = 100$ K and the lattice parameter was adjusted to ensure that the solid was stress-free at this temperature.

Prior to studying thermal fluctuations, two types of additional simulations were performed to generate data needed for a comparison with fluctuation results. Firstly, the phonon density of states $g(f)$ at 100 K was computed by the method developed by Kong [66] and implemented in LAMMPS. This method was chosen because it does not rely on fluctuations and provides independent results for comparison. Secondly, to test the accuracy of the simulation methodology, the specific heat of the solid was computed by a direct (non-fluctuation) method. This was accomplished by running canonical (NVT) MD simulations at the temperatures of 50, 100 and 150 K and calculating the time average energies $\langle E \rangle$. The volume was fixed at the value corresponding to 100 K. The energy was found to follow a linear temperature dependence in this temperature interval, from which the derivative $(\partial \langle E \rangle / \partial T)_{N,V}$ was evaluated by a linear fit. The specific heat at 100 K was then found from the equation $c_v^0 = (\partial \langle E \rangle / \partial T)_{N,V}/N$. The number obtained was 24.89 J/(mol K), which is close to the equipartition theorem prediction $3k = 24.94$ J/(mol K).

5.2.2 Post-processing procedures

We next describe the statistical analysis of the MD results at the post-processing stage. Consider a long MD simulation run implemented for a time t_{tot}. Suppose two fluctuating properties, X and Y, are saved at every integration step of the simulation. These can be the kinetic, potential or total energy of the solid. We trivially compute the time average values $\langle X \rangle$ and $\langle Y \rangle$, as well as the variances $\langle (\Delta X)^2 \rangle$ and $\langle (\Delta Y)^2 \rangle$ and the covariance $\langle \Delta X \Delta Y \rangle$, were $\Delta X = X - \langle X \rangle$ and $\Delta Y = Y - \langle Y \rangle$.

For a spectral analysis, we break the long stochastic processes $X(t)$ and $Y(t)$ into a large number of shorter processes, $x(t)$ and $y(t)$, by dividing the total time t_{tot} into smaller intervals of the same duration $\theta \ll t_{\text{tot}}$. The time θ was chosen to be longer than the correlation times of both variables, so that the intervals represent statistically independent samples with different initial conditions. For each time interval $0 \leq t \leq \theta$ we perform a discrete Fourier transformation of $x(t)$ and $y(t)$ to obtain a set of Fourier amplitudes, $\hat{x}_j$ and $\hat{y}_j$, corresponding to the frequencies $f_j = j/\theta$, where $j = 0, \pm 1, \pm 2, \ldots$. These amplitudes are complex numbers satisfying the symmetry relations $\hat{x}_{-j} = \hat{x}_j^*$ and $\hat{y}_{-j} = \hat{y}_j^*$ (the asterisk denotes complex conjugation). The functions

$$\hat{C}_{XX}(f_j) = \frac{\overline{\hat{x}_j \hat{x}_j^*}}{f_1}, \qquad \hat{C}_{YY}(f_j) = \frac{\overline{\hat{y}_j \hat{y}_j^*}}{f_1},$$

where the bar denotes averaging over all time intervals, represent the ensemble-averaged power spectra of X and Y. Likewise,

$$\hat{C}_{XY}(f_j) = \frac{\overline{\hat{x}_j \hat{y}_j^*}}{f_1}$$

represents the spectral power of X-Y correlations.

Following the Wiener-Khinchin theorem [68, 70], the functions $\hat{C}_{XX}(f_j)$, $\hat{C}_{YY}(f_j)$ and

$\hat{C}_{XY}(f_j)$ were then subject to inverse Fourier transformations to obtain the auto-correlation functions (ACF) $C_{XX}(t) = \langle X(0)X(t)\rangle$ and $C_{YY}(t) = \langle Y(0)Y(t)\rangle$ and the cross-correlation function (CCF) $C_{XY}(t) = \langle X(0)Y(t)\rangle$. In this work, we are interested in correlations between properties relative to their average values, namely, $C_{\Delta X\Delta X}(t) = \langle \Delta X(0)\Delta X(t)\rangle$, $C_{\Delta Y\Delta Y}(t) = \langle \Delta Y(0)\Delta Y(t)\rangle$ and $C_{\Delta X\Delta Y}(t) = \langle \Delta X(0)\Delta Y(t)\rangle$. These were readily obtained by removing the point f_0 from the spectra prior to the Fourier inversion.

All correlation functions in the frequency domain shown in the figures below have been normalized by $\langle(\Delta X)^2(\Delta Y)^2\rangle^{1/2}$. For ACFs, the area under the normalized plots agains the frequency is therefore unity.

To evaluate the effect of the averaging timescale on the fluctuation relations more directly, the spectral analysis was supplemented by a simple coarse-graining procedure in the time domain. For this procedure, we lifted the requirement that the time interval θ be longer than the correlation time. For every time interval l, we computed the time average energy values $\langle X\rangle_l$, $\langle Y\rangle_l$, etc. A formal temperature T_l was defined by the equipartition relation $T_l = 2\langle K\rangle_l/3Nk$. These coarse-grained values were then treated as a new dataset, for which we computed the fluctuation properties such as $\langle(\Delta E)^2\rangle_\theta$, $\langle(\Delta T)^2\rangle_\theta$ and $\langle\Delta E\Delta T\rangle_\theta$. These fluctuation properties were examined as functions of the time interval θ. For $\theta = dt$, this procedure reduces to computing the fluctuations of instantaneous properties. By increasing θ, we can scan various timescales, including t_r, τ_r, and the quasi-equilibrium timescale in between.

5.3 Simulation results and discussion

5.3.1 NVE simulations

The goal of the NVE simulations was to evaluate the phonon relaxation time at the chosen temperature and make consistency checks of the methodology. In Fig. 5.1 we show the kinetic energy ACF in the frequency and time domains. The results were obtained from a $t_{\text{tot}} = 2$ ns MD run by averaging over $\theta = 3$ ps time intervals. For comparison, the plot

of $\hat{C}_{\Delta K \Delta K}(f)$ [Fig. 5.1(a)] includes the phonon density of states $g(f/2)$ computed by the non-fluctuation method [66] and plotted against the frequency f followed by normalization to unit area.

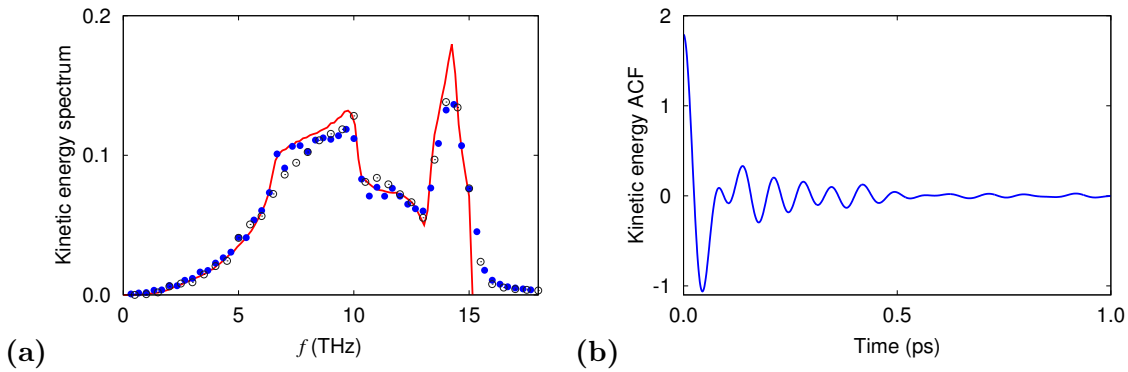

Figure 5.1: Results of NVE MD simulations. (a) Normalized power spectrum $\hat{C}_{\Delta K \Delta K}(f)$ of kinetic energy fluctuations (filled circles), velocity ACF $\hat{C}_{vv}(f/2)$ (open circles), and phonon density of states $g(f/2)$ (solid line). (b) The kinetic energy ACF $C_{\Delta K \Delta K}(t)$.

The close similarity between the plots is not surprising: in a perfectly harmonic solid, the kinetic energy ACF is identical to the phonon density of states except for the doubling of the frequency scale [28, 97, 115]. This doubling is due to the fact that kinetic energy goes through zero twice per vibration period. In the present simulations, the vibrations were not perfectly harmonic. The anharmonicity slightly washed out the shape of the spectrum and produced a high-frequency tail. Since the total energy is strictly conserved, the potential energy ACF has an identical shape (not shown here). As another test, the velocity ACF $\hat{C}_{vv}(f)$ was computed from the same simulation run. As expected, it was found to be very similar to $\hat{C}_{\Delta K \Delta K}(f)$ except for the frequency doubling effect: $\hat{C}_{vv}(f/2) \approx g(f/2) \approx \hat{C}_{\Delta K \Delta K}(f)$.

The time-dependent ACF $C_{\Delta K \Delta K}(t)$ shown in Fig. 5.1(b) indicates that the relaxation time due to phonon scattering is about 0.5 ps. Strictly speaking, this time depends on the

phonon frequency and polarization, but we are only interested in a crude estimate. For comparison, the period t_K of kinetic energy fluctuations can be estimated using a typical frequency of $\bar{f} = 10$ THz [Fig. 5.1(a)], which gives about $t_K \approx 0.1$ ps. The factor of five difference between the two timescales is a measure of anharmonicity of this solid at 100 K.

In the NVE ensemble, the variance of the kinetic energy of the centers of mass of the particles is [72]

$$\langle(\Delta K)^2\rangle_{NVE} = \frac{3N(kT_0)^2}{2}\left(1 - \frac{3k}{2c_v^0}\right). \tag{5.10}$$

Using $\langle(\Delta K)^2\rangle_{NVE}$ obtained by the simulation, this equation was inverted to solve for c_v^0. The number obtained was 25.06 J/(mol K), which is in good agreement with 24.94 J/(mol K) predicted by the equipartition theorem.

We emphasize that equilibrium temperature fluctuations in the NVE ensemble are undefined since quasi-equilibrium states are only sampled by small subsystems of the system but not the system as a whole. As already mentioned, one can always formally define an "instantaneous temperature" $\hat{T}$ and its fluctuations, but this temperature is identical (up to units) to the instantaneous kinetic energy per atom and does not provide new physical insights.

5.3.2 NVT simulations

The NVT MD simulations were conducted with two time constants of the Langevin thermostat: $\tau_r = 10$ and 100 ps. The simulations times were $t_{\text{tot}} = 1000\tau_r$ (10 and 100 ns, respectively). The kinetic and total energy fluctuations are illustrated in Fig. 5.2. To facilitate the comparison, the energies were shifted relative to their time average values and normalized by standard deviations.

The plots clearly demonstrate the existence of two different fluctuation processes: fast fluctuations of kinetic energy and much slower fluctuations of total energy. The fast fluctuations occur on the timescale of phonon frequencies, whereas the slow fluctuations occur

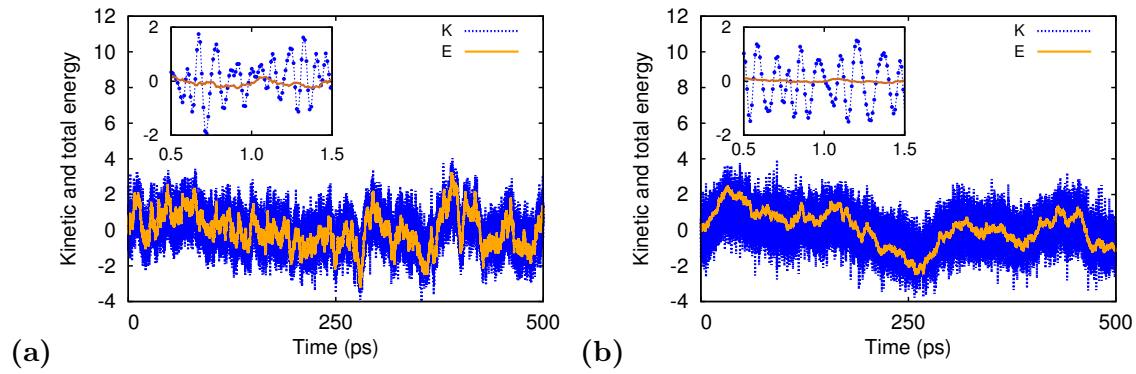

Figure 5.2: Representative fluctuations of the kinetic (blue) and total (orange) energy in the NVT ensemble with the thermostat time constants (a) $\tau_r = 10$ ps and (b) $\tau_r = 100$ ps. To enable comparison, the energies were shifted relative to the average values and normalized by the standard deviations. The insets zoom into shorter time intervals to demonstrate the existence of two different timescales of the fluctuations (fast and slow).

on the thermostat timescale τ_r. The large disparity between the two timescales is demonstrated in the insets, where the kinetic energy fluctuations are superimposed on nearly constant total energy. This two-scale behavior is especially manifest for the slower thermostat ($\tau_r = 100$ ps) and is a clear signature of quasi-equilibrium states, in which the system behaves as if it were isolated and thus maintained a constant energy.

Figures 5.3(a,b) show the results of the timescale analysis discussed in Sec. 5.2.2, in which the energies were averaged over different time intervals θ before computing their fluctuations (Fig. 5.3(c) will be discussed later).

The variances/covariances $\langle(\Delta T)^2\rangle_\theta$, $\langle\Delta E\Delta T\rangle_\theta$ and $\langle(\Delta E)^2\rangle_\theta$ are compared with the right-hand sides of Eqs.(5.1), (5.2) and (5.3), respectively. The deviation is normalized by the value of the right-hand side and plotted against θ. Recall that the minimum value of θ is the integration step dt, corresponding to instantaneous values of the energies. Observe that the "instantaneous temperature" fluctuation $\left\langle(\Delta\hat{T})^2\right\rangle$ has a 50% error. This number is consistent with the theoretical prediction in Sec. 5.1 that an estimate of temperature fluctuations from $\hat{T}$ will be off by a factor of two. As the averaging time θ increases, the

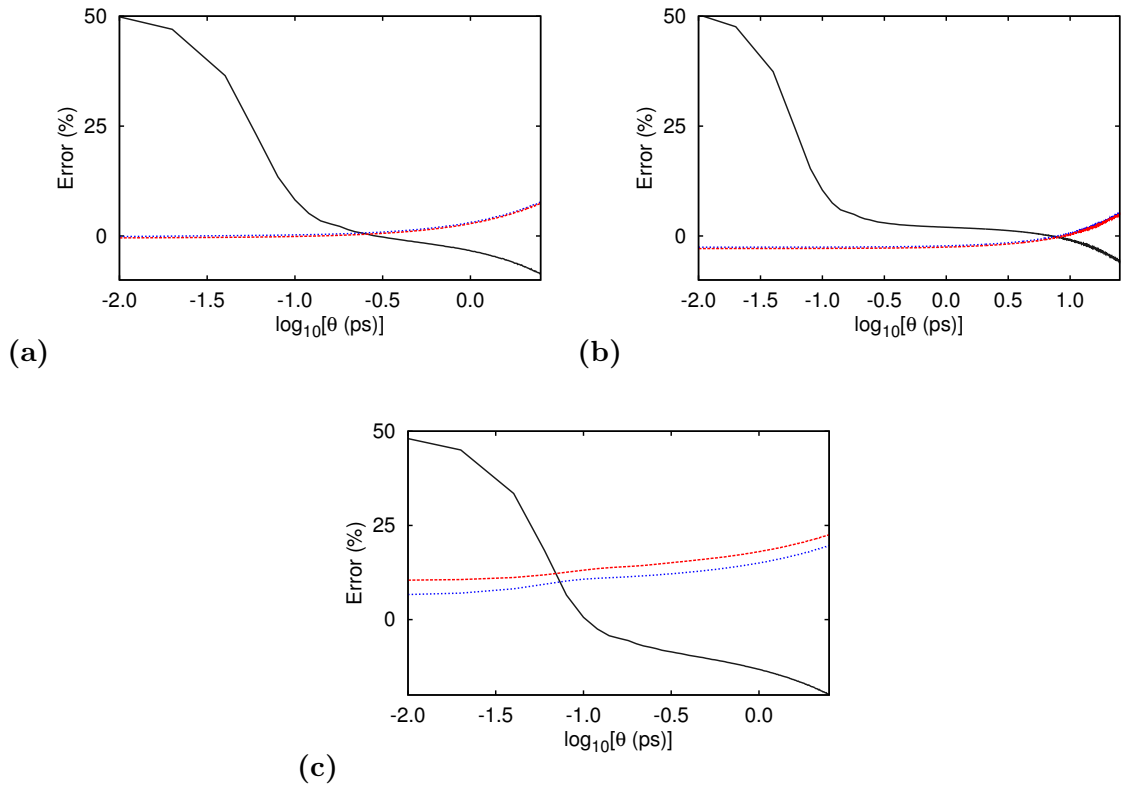

Figure 5.3: Normalized difference between the right and left-hand sides of fluctuation relations as functions of the averaging time interval θ: Eq.(5.1) (black solid line), Eq.(5.2) (red dashed line) and Eq.(5.3) (blue dotted line) . (a) Langevin thermostat with $t_r = 10$ ps, (b) Langevin thermostat with $t_r = 100$ ps, (c) natural thermostat.

error diminishes. When θ exceeds the phonon relaxation time t_r (about 0.5 ps), the error reduces to $\pm$ a few percent and remains on this low level until θ approaches the thermostat time τ_r. At that point the error increases again since the averaging begins to smooth the temperature fluctuations. In the limit of $\theta \to \infty$, all fluctuations are totally suppressed and the error goes to 100%. This behavior clearly demonstrates the existence of a timescale on which the temperature defined by the average kinetic energy satisfies the fluctuation relation (Eq. 5.1). As predicted in Sec. 5.1, this timescale lies between t_r and τ_r where the system samples quasi-equilibrium states. Comparing Figs. 5.3(a) and 5.3(b), we observe that the range of validity of Eq.(5.1) widens as the thermostat time τ_r increases at a fixed

t_r, which is again consistent with the definition of quasi-equilibrium states. By contrast, the errors in $\langle \Delta E \Delta T \rangle_\theta$ and $\langle (\Delta E)^2 \rangle_\theta$ remain negligible on all timescales until θ approaches τ_r and the averaging begins to suppress the fluctuations. This is also fully consistent with the theory. As discussed in Sec. 5.1, Eqs.(5.2) and (5.3) remain valid for both instantaneous and quasi-equilibrium values of the fluctuating properties, which is consistent with Figs. 5.3(a,b).

Turning to the spectral analysis of the fluctuations, Fig. 5.4 presents the power spectra of the kinetic and potential energies for the two Langevin thermostats. For the total energy, the spectrum shows a monotonic decay with frequency and dies off at frequencies larger than $1/\tau_r$, which supports the notion that the total energy fluctuations are primarily caused by slow exchanges with the thermostat. By contrast, the kinetic energy spectrum consists of two parts separated by a frequency gap. The low-frequency part is very similar to that for the total energy, suggesting a strong correlation. The high-frequency part has a shape of the phonon spectrum (plotted as a function of $2f$) and is virtually identical to the spectrum computed in the NVE ensemble (cf. Fig. 5.1). Note also that the high-frequency part of the spectrum is the same regardless of the thermostat time constant. This part of the spectrum is dominated by the phonon processes and is independent of how and whether the system interacts with environment. The gap between the low and high-frequency parts of the spectrum is where the system is found in quasi-equilibrium states. As expected, this gap widens as τ_r increases.

The kinetic-potential and kinetic-total CCFs in the frequency domain are plotted in Fig. 5.5. The respective ACFs are also shown for comparison. Note that, at high frequencies, the kinetic-potential energy CCF $\hat{C}_{\Delta K \Delta U}(f)$ is a mirror image of the kinetic energy ACF $\hat{C}_{\Delta K \Delta K}(f)$ [Fig. 5.5(a)].

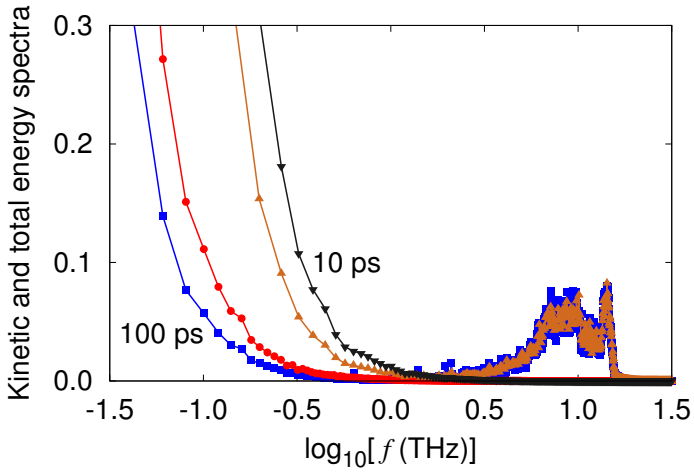

Figure 5.4: Normalized power spectra of kinetic and total energy fluctuations in the NVT ensemble with a Langevin thermostat for two different time constants (10 and 100 ps). Square and triangle symbols - kinetic energy, circle and nabla symbols - total energy.

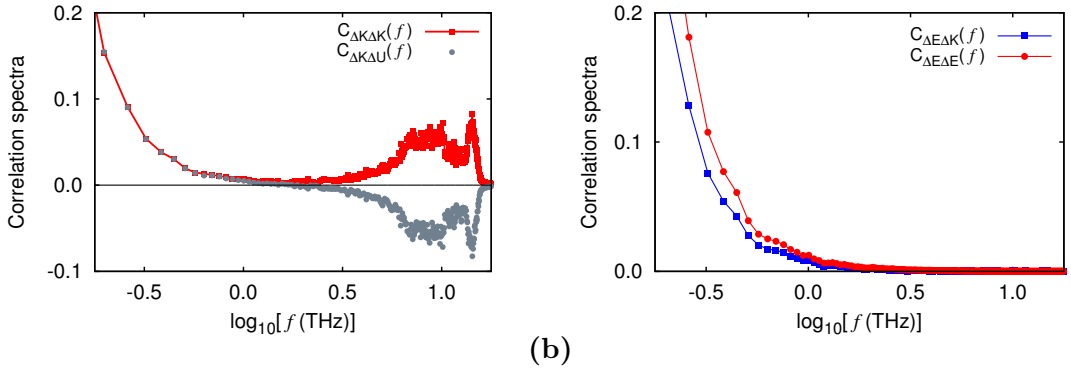

Figure 5.5: Results of NVT MD simulations with a Langevin thermostat ($\tau_r = 10$ ps). (a) Comparison of the kinetic energy ACF and kinetic-potential energy CCF in the frequency domain. Note that both spectra have the same shape but opposite sign at high frequencies and coincide at low frequencies. (b) Comparison of the total energy ACF and kinetic-total energy CCF in the frequency domain. Both functions show a similar monotonic decrease with frequency and die off above $1/\tau_r$.

This reflects the nearly perfect anti-correlation between the two energies on the phonon

timescale where the energy exchanges with the thermostat are negligible and the solid behaves as if it were isolated. In the low-frequency range below the gap, $\hat{C}_{\Delta K \Delta U}(f)$ and $\hat{C}_{\Delta K \Delta K}(f)$ practically coincide. This is also expected since the energy exchanges with the thermostat increase or decrees the kinetic and potential energies (averaged over the phonon timescale) simultaneously. Although these correlation functions are only shown for $\tau_r = 10$ ps, the results for $\tau_r = 100$ ps look very similar except for a wider frequency gap. On the other hand, the $\hat{C}_{\Delta K \Delta E}(f)$ and $\hat{C}_{\Delta E \Delta E}(f)$ correlation functions are similar for all frequencies [Fig. 5.5(b)]. In the low-frequency range, this is consistent with the correlated behavior of all components of energy during the thermostat exchanges. At high frequencies, the fast fluctuations of kinetic energy and nearly constant total energy produce a zero CCF. Since both correlation functions are strongly dominated by low frequencies, $\langle(\Delta E)^2\rangle$, $\langle \Delta E \Delta K \rangle$ and $\langle \Delta E \Delta T \rangle$ remain the same on both the instantaneous and quasi-equilibrium timescales.

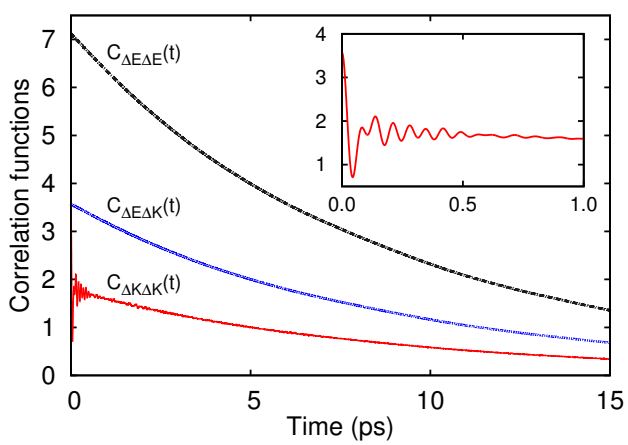

Figure 5.6: Energy correlation functions in the time domain obtained by NVT MD simulations with a Langevin thermostat ($\tau_r = 10$ ps). The inset is a zoom into the short-range part of the kinetic energy ACF.

Figure 5.6 shows the correlation functions in the time domain. Again, only the functions

for $\tau_r = 10$ ps are shown; the result for $\tau_r = 100$ ps lead to similar conclusions. Two of the functions accurately follow the exponential relations

$$C_{\Delta E \Delta E}(t) = \langle (\Delta E)^2 \rangle e^{-t/\tau_r} \tag{5.11}$$

and

$$C_{\Delta E \Delta K}(t) = \langle \Delta K \Delta E \rangle e^{-t/\tau_r} \tag{5.12}$$

expected for a system interacting with a Langevin thermostat. By contrast, the kinetic energy ACF $C_{\Delta K \Delta K}(t)$ only follows the exponential relation

$$C_{\Delta K \Delta K}(t) = \langle (\Delta K)^2 \rangle_q e^{-t/\tau_r}, \;\; t \gg t_r, \tag{5.13}$$

on the timescale $t \gg t_r$. Here, $\langle (\Delta K)^2 \rangle_q = 1.786$ eV^2 is the value obtained by extrapolation to $t \to 0$. For shorter times, $C_{\Delta K \Delta K}(t)$ is a superposition of Eq.(5.13) and fast-decaying oscillations representing phonon processes. This short-range part is illustrated in the inset and is the same for $\tau_r = 100$ ps (not shown). Furthermore, this part is identical to $C_{\Delta K \Delta K}(t)$ obtained in the NVE ensemble (cf. Fig. 5.1). This is illustrated in Fig. 5.7 by superimposing the NVT and NVE ACFs, which show accurate agreement.

It follows that the entire function $C_{\Delta K \Delta K}(t)$ computed in the NVT ensemble can be presented in the form

$$C_{\Delta K \Delta K}(t) = [C_{\Delta K \Delta K}(t)]_{NVE} + \langle (\Delta K)^2 \rangle_q e^{-t/\tau_r}, \tag{5.14}$$

where the first term represents the short-range correlations. Equation (5.14) shows the same timescale decomposition as already observed in the spectral form. $\langle (\Delta K)^2 \rangle_q$ represents the quasi-equilibrium timescale and can be used to calculate the temperature fluctuations.

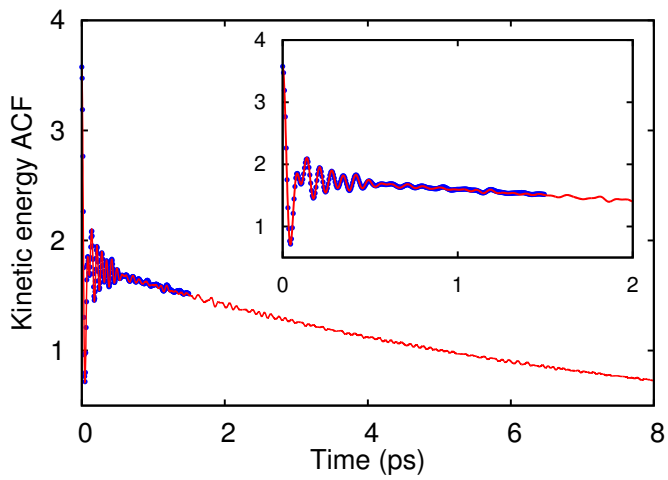

Figure 5.7: The NVT kinetic energy ACF for a Langevin thermostat with $\tau_r = 10$ ps (red curve) superimposed on the NVE kinetic energy ACF (blue points). The inset shows a zoom into the short-time region.

Taking Eq.(5.14) to the limit of $t \to 0$, we obtain

$$\langle(\Delta K)^2\rangle = \langle(\Delta K)^2\rangle_{NVE} + \langle(\Delta K)^2\rangle_q. \tag{5.15}$$

Inserting $\langle(\Delta K)^2\rangle$ and $\langle(\Delta K)^2\rangle_{NVE}$ from Eqs.(5.8) and (5.10), respectively, we arrive at

$$\langle(\Delta K)^2\rangle_q = \frac{9Nk^3T_0^2}{4c_v^0}. \tag{5.16}$$

The temperature is defined by Eq.(5.5), from which

$$\langle(\Delta T)^2\rangle = \frac{4\langle(\Delta K)^2\rangle_q}{9N^2k^2}. \tag{5.17}$$

Inserting $\langle(\Delta K)^2\rangle_q$ from Eq.(5.16) we exactly recover the fluctuation relation (5.1).

As an additional numerical test, c_v^0 was extracted from Eq.(5.16) to obtain $c_v^0 = 24.89$

J/(mol K) in good agreement with the independent calculation in Sec. 5.2.1.

5.3.3 Additional tests

To demonstrate that the results reported in the previous sections are not artifacts of the Langevin thermostat, selected simulations were repeated using the Nose-Hover thermostat implemented in LAMMPS [107]. The results (not shown here for brevity) were found to be in full agreement with the simulations employing the Langevin thermostat, including the timescale separation and validation of the fluctuation relation (5.1) with temperature computed in quasi-equilibrium states.

Both the Langevin and Nose-Hover algorithms implement virtual thermostats that correctly sample the canonical distribution but still differ from a physical thermostat. The latter is commonly associated with a large volume of some inert substance possessing a large heat capacity and separated from the system by a physical interface. The energy exchange with the thermostat is then controlled by heat conduction across the interface, which is different from random perturbations of atoms uniformly across the system as in the virtual thermostats. To eliminate any possibility that the virtual thermostats could affect our conclusions, efforts were taken to model a "natural" thermostat and show that the conclusions remain valid. By a "natural" thermostat we mean a simulation block much larger than our system and separated from the latter by a physical interface.

As the first step, the NVE MD simulations were executed as above (Sec. 5.3.1), but this time, atoms within a relatively small cubic block selected at the center of the system were treated as the system itself, whereas the rest of the simulation cell was considered a thermostat. Accordingly, the energy correlation functions were only computed for the small subsystem. Repeating the same statistical analyses as above, it was confirmed that the phonon relaxation time and the thermostat exchange time were significantly different, creating a large time interval (accordingly, a frequency gap in the spectrum of kinetic energy) in which the system existed in quasi-equilibrium states. The temperature defined on this quasi-equilibrium timescale was found to satisfy the fluctuation relation (5.1).

But even this test was not found completely satisfactory. The volume of the inner lattice block selected as our system was not strictly fixed but rather fluctuated during the simulations. Strictly speaking, the ensemble implemented on the system was NPT (with zero pressure) rather than NVT. Although the fluctuation relations (5.1) and (5.2) remain valid in the NPT ensemble as well [93], the simulations with the virtual thermostats were conducted in a different (NVT) ensemble.

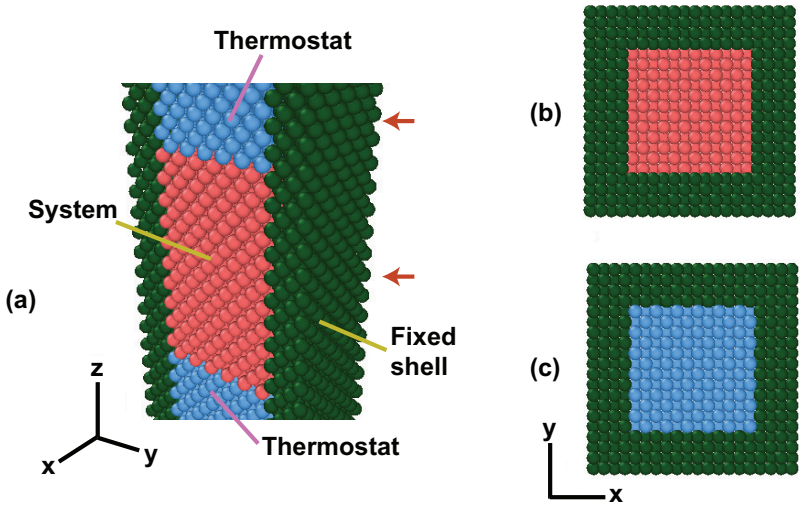

Figure 5.8: The anatomy of the "natural" thermostat implemented in this work. (a) Vertical cross-section of the simulation block revealing the cubic system under study at the center, the thermostat regions above and below the system, and a fixed shell enclosing both the system and the thermostat. The entire assembly is much longer in the vertical (z) direction than shown. (b) and (c) show horizontal (x-y) cross-sections at the levels indicated by the arrows.

To make sure that the comparison is made for the same ensemble, the natural thermostat was redesigned as shown in Fig. 5.8. A cubic lattice block with an edge of about 2 nm (about 1400 atoms) was embedded at the center of a larger periodic block with the dimensions $3.6 \times 3.6 \times 72$ nm (80,000 atoms). This relatively small inner lattice block was the system to be studied. Atoms within a 0.8 nm shell parallel to the long (z) direction were fixed in their positions. The remaining atoms above and below the cubic block represented the thermostat and were subject to the following constraint: they could only vibrate in the x

and y directions while their z-coordinates were fixed. As a result, the cubic system was fully surrounded by atoms incapable of motion in the directions normal to the faces of the cube. The volume of the system was thereby fixed, imitating rigid walls of a calorimeter. At the same time, the thermostat atoms above and below the cube could exchange energy with it by heat conduction across the interfaces mediated by transverse phonons (polarized in the x-y plane). This heat exchange controlled the system temperature. The entire assembly was brought to thermal equilibrium at the temperature of 100 K.[17] As usual, the lattice parameter was chosen to ensure zero mechanical stress in the system. Once equilibrium was reached, a 20 ns long NVE MD simulation was performed to compute statistical properties of fluctuations as described above.

Fig. 5.3(c) shows the normalized differences between the variances/covariances $\langle(\Delta T)^2\rangle_\theta$, $\langle\Delta E\Delta T\rangle_\theta$ and $\langle(\Delta E)^2\rangle_\theta$ computed with the natural thermostat and the right-hand sides of Eqs.(5.1), (5.2) and (5.3), respectively. The results are qualitatively the same as obtained with the Langevin thermostat [Fig. 5.3(a,b)]. The deviation from the temperature fluctuation relation (5.1) is again about 50% when the instantaneous temperature is used ($\theta = dt$) and reduces to approximately $\pm$ 10% when the temperature is defined by the kinetic averaged over the time intervals $\theta \gtrsim 0.1$ ps. When θ reaches a few ps or higher, the error increases again due to the smoothing of fluctuations by averaging over timescales comparable with the thermostat time. We can conclude that the latter must be on the order of 10 ps. Thus, the quasi-equilibrium timescale for this thermostat is between ~ 0.1 and ~ 10 ps. In this time interval, the temperature fluctuation relation (5.1) is approximately followed, although not as accurately as with the Langevin thermostat. This is understandable given that the system in the natural thermostat was a factor of 20 smaller and subject to a size effect.[18] Upscaling of both the system and the thermostat would likely reduce the error but was not pursued in this work.

[17]Since the partially constrained atoms forming the thermostat were thermally active only in the x and y directions, their temperature was computed as $\langle K\rangle/Nk$. In the system itself, the temperature was as usual $2\langle K\rangle/3Nk$.

[18]The phonon mean free path at this temperature is estimated to be about 1.3 nm, which is comparable to the system size.

Spectral analysis of energy fluctuations has shown that the system closely follows the same trends as for the Langevin and Nose-Hoover thermostats. As one example, Fig. 5.9 compares the power spectra of kinetic energy for the natural and Langevin thermostats.

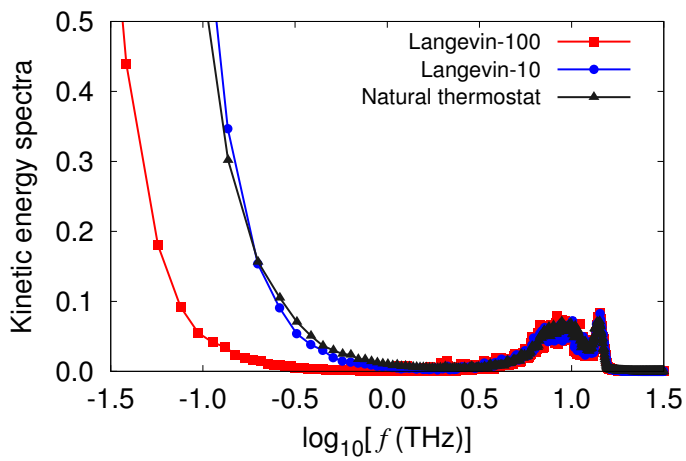

Figure 5.9: Power spectra of kinetic energy from NVT MD simulations of systems connected to a natural thermostat and two Langevin thermostats with the time constants of 10 and 100 ps.

The high-frequency parts of the spectra coincide almost perfectly. The low-frequency parts controlled by energy exchanges with the thermostat also have similar shapes. In fact, for the natural thermostat, this part of the spectrum is very close to that for the Langevin thermostat with $\tau_r = 10$ ps. This confirms the above estimate of the time constant of the natural thermostat. This also shows that the time constants of the Langevin thermostat chosen for this study were quite realistic. Overall, we can conclude that the association of the temperature fluctuation relation (5.1) with the quasi-equilibrium timescale has a generic validity and does not reflect some specific features of thermostats.

5.4 Conclusions

We have addressed the long-standing controversy regarding the meaning, or even existence, of temperature fluctuations in canonical systems. Over the past decades, the temperature fluctuation relation (5.1) appearing in many textbooks and papers [19, 22, 70, 93] has received different interpretations, including the assertion that this equation is meaningless [63–65] or at best a mere formality [30, 84, 126]. We have demonstrated that Eq.(5.1) is a physically meaningful relation that remains valid as long as the temperature is defined on an appropriate timescale. This interpretation of temperature fluctuations has been supported by MD simulations of a quasi-harmonic solid connected to a thermostat.

The simulations have confirmed the existence of two different fluctuation timescales in canonical systems. The shorter timescale is associated with the time required for a small isolated system to reach thermodynamic equilibrium. For an atomic solid studied here, this time t_r is controlled by phonon scattering. In this work, this time was about 0.5 ps at the temperature of 100 K. The longer timescale arises due to slow energy exchanges between the system and the thermostat. Such exchanges may occur by a variety of physically different mechanisms, such as heat transfer across the system/thermostat interface. For the natural and virtual thermostats studied here, the energy exchange time τ_r was on the order of 10 to 100 ps. Thus, τ_r is orders of magnitude longer than t_r. At the intermediate timescale t_q ($t_r \ll t_q \ll \tau_r$) the system remains in internal thermodynamic equilibrium and can be treated as if it were disconnected from the thermostat. In such quasi-equilibrium states, it has well-defined intensive properties such as temperature, pressure and chemical potential.

In particular, temperature can be defined through the equipartition relation using the kinetic energy averaged on the quasi-equilibrium timescale t_q. It has been shown that fluctuations of the temperature so defined do follow Eq.(5.1). Attempts to define temperature through kinetic energy averaged over shorter ($< t_r$) or longer ($> \tau_r$) time intervals result in significant deviations from Eq.(5.1).

The timescale separation is also reflected in the shape of the kinetic energy ACF in the

frequency domain, showing two peaks separated by a frequency gap. The peak at $f = 0$ arises from energy exchanges with the thermostat, whereas the second peak is associated with phonon processes and has the shape of the phonon density of states (plotted against $2f$). The frequency gap represents the quasi-equilibrium states. The potential energy ACF has a similar structure and can also be used for the identification of quasi-equilibrium states. Thus, measured or computed energy spectra of a canonical system carry all information about the timescale on which temperature fluctuations are well-defined and follow Eq.(5.1).

The conclusions of this work were tested by MD simulations with two virtual thermostats (Langevin and Nose-Hoover) and a natural thermostat consisting of large crystalline regions surrounding the system. In the future, a similar study could evaluate the validity of pressure fluctuation relations for canonical systems [70, 93, 113].

Chapter 6: Summary

In summary, the third chapter of this work has advanced the field of binary alloy GB premelting by proposing a novel analytical form of the disjoining potential that describes repulsive, attractive and intermediate interactions between solid-liquid interfaces by a single equation. Atomistic simulations of GBs in binary Cu-Ag solutions were conducted to explore various temperatures, chemical compositions and GB energies and to test and expand our theory. The fluctuation approach applied previously to single-component GBs [31, 56] and extended here to binary systems, was applied to extract the disjoining potentials from the simulations under various conditions. All three types of disjoining potentials were found: repulsive, attractive and intermediate, in full agreement with predictions of the liquid layer model with the analytical potential. Multiple consistency checks performed during the simulations demonstrate the reliability of the results. In particular, the GB free energy was computed by thermodynamic integration, producing results consistent with the liquid layer model with the analytical disjoining potential. An important result of the simulations is the confirmation of the existence of multiple stable and metastable states of premelted GBs under appropriate conditions. Such states are characterized by different GB widths as well as other excess properties. During continuous variations of thermodynamic state of the grains, the relative stability of such states varies and at some point can result in a thin-thick phase coexistence. Additional calculations could generate a thin-thick phase coexistence line on the Cu-Ag phase diagram, but this is left for future work.

In the fourth chapter of the work we have extended the previous studies of the $\Sigma 5$ GBs [36–38, 46] to a larger set of [001] symmetrical tilt GBs in order to evaluate the generality of the previous findings. The GB structures and energies have been calculated by allowing variations in the GB density λ and large displacements of atoms during the energy minimization. From this work we have demonstrated that λ should be included in

the descriptions of GBs as an additional parameter capable of predicting GB phases and phase transformations.

In chapter five we have addressed the long-standing controversy regarding the meaning, or even existence, of temperature fluctuations in canonical systems. Over the past decades, the temperature fluctuation relation (5.1) appearing in many textbooks and papers [19, 22, 70, 93] has received different interpretations, including the assertion that this equation is meaningless [63–65] or at best a mere formality [30, 84, 126]. We have demonstrated that Eq.(5.1) is a physically meaningful relation that remains valid as long as the temperature is defined on an appropriate timescale. This interpretation of temperature fluctuations has been supported by MD simulations of a quasi-harmonic solid connected to a thermostat.

Finally, as a closing summary we include the following list which includes all of the publications which resulted from this thesis:

1. **2017:** J. Hickman and Y. Mishin, Extra variable in grain boundary description. Physical Review Materials 1, No. 1, p. 010601, [selected as EDITOR'S SUGGESTION].

2. **2016:** J. Hickman and Y. Mishin, Disjoining potential and grain boundary premelting in bi- nary alloys. Physical Review B 93, No. 224108.

3. **2016:** Y. Mishin and J. Hickman, Energy spectrum of a Langevin oscillator. Physical Review E 94, No. 6, p. 062151.

4. **2016:** J. Hickman and Y. Mishin, Temperature fluctuations in canonical systems: Insights from molecular dynamics simulations. Physical Review B 94, No. 184311.

Chapter A: GB structure catalog

Figures A.1 and A.2 contain the complete set of $\gamma(\lambda)$ plots for the Cu GBs studied in chapter-4 of this work. The trend lines are shown as a guide to the eye. For GBs composed on identical structural units, the data points are shown by symbols representing the respective structural units ($\diamondsuit$ K, $\square$ L, $\bigcirc$ M).

In Tab. A.1 we compare the energies associated with the new global minima obtained using our method and the previous values associated with regular kites. In the rightmost column of tab.A.1 we denote in bold the boundaries which have new energies lower than those of regular kites. Again this table reiterates the fact that the majority of the STGB studied have structures with energies lower than the regular kites.

Table A.1: A comparison of the energies associated with the regular kite K_1 with the new global minima obtained in this work. In the rightmost column the new values with energies lower than that of regular kites are displayed in bold font

Boundary	θ	γ_{gb} (Jm^{-2}) (regular kites)	γ_{gb} (Jm^{-2}) (new minima)
Σ101(1010)	11.42^o	0.686	**0.676**
Σ25(710)	16.26^o	0.796	**0.783**
Σ37(610)	18.92^o	0.837	**0.823**
Σ13(510)	22.62^o	0.878	**0.864**
Σ17(410)	28.07^o	0.914	**0.903**
Σ53(720)	31.89^o	0.939	**0.935**
Σ5(310)	36.87^o	0.905	0.905
Σ5(210)	53.13^o	0.951	**0.936**
Σ17(530)	61.93^o	0.856	0.856
Σ13(320)	67.38^o	0.790	0.790
Σ25(430)	73.74^o	0.677	**0.666**
Σ61(650)	79.61^o	0.533	**0.513**

Figures A.4 to A.6 display the structures of select Cu GBs studied in this work.

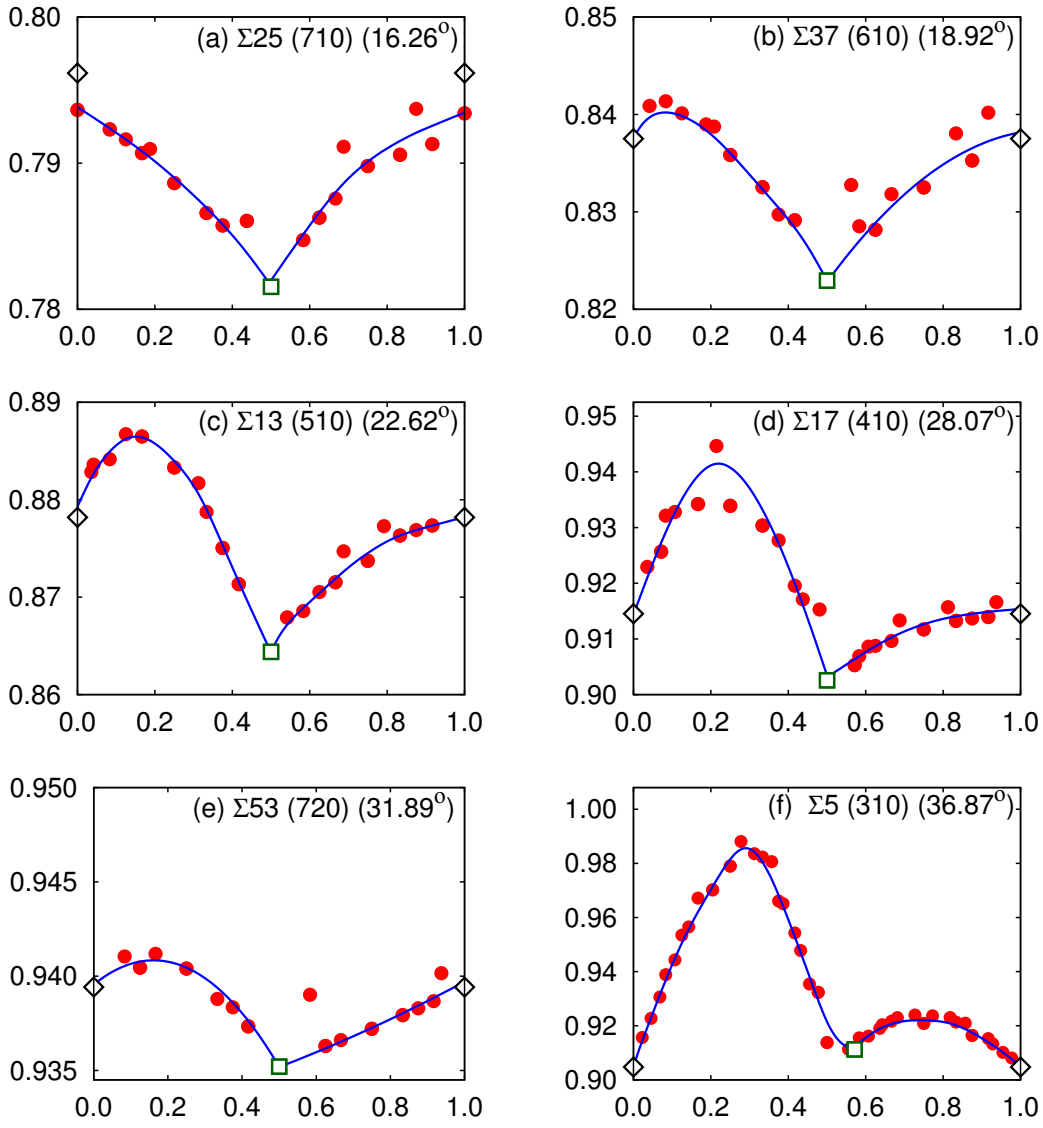

Figure A.1: GB energy (in J/m^2) versus GB density λ (fraction of atoms removed) for symmetrical tilt GBs in Cu.

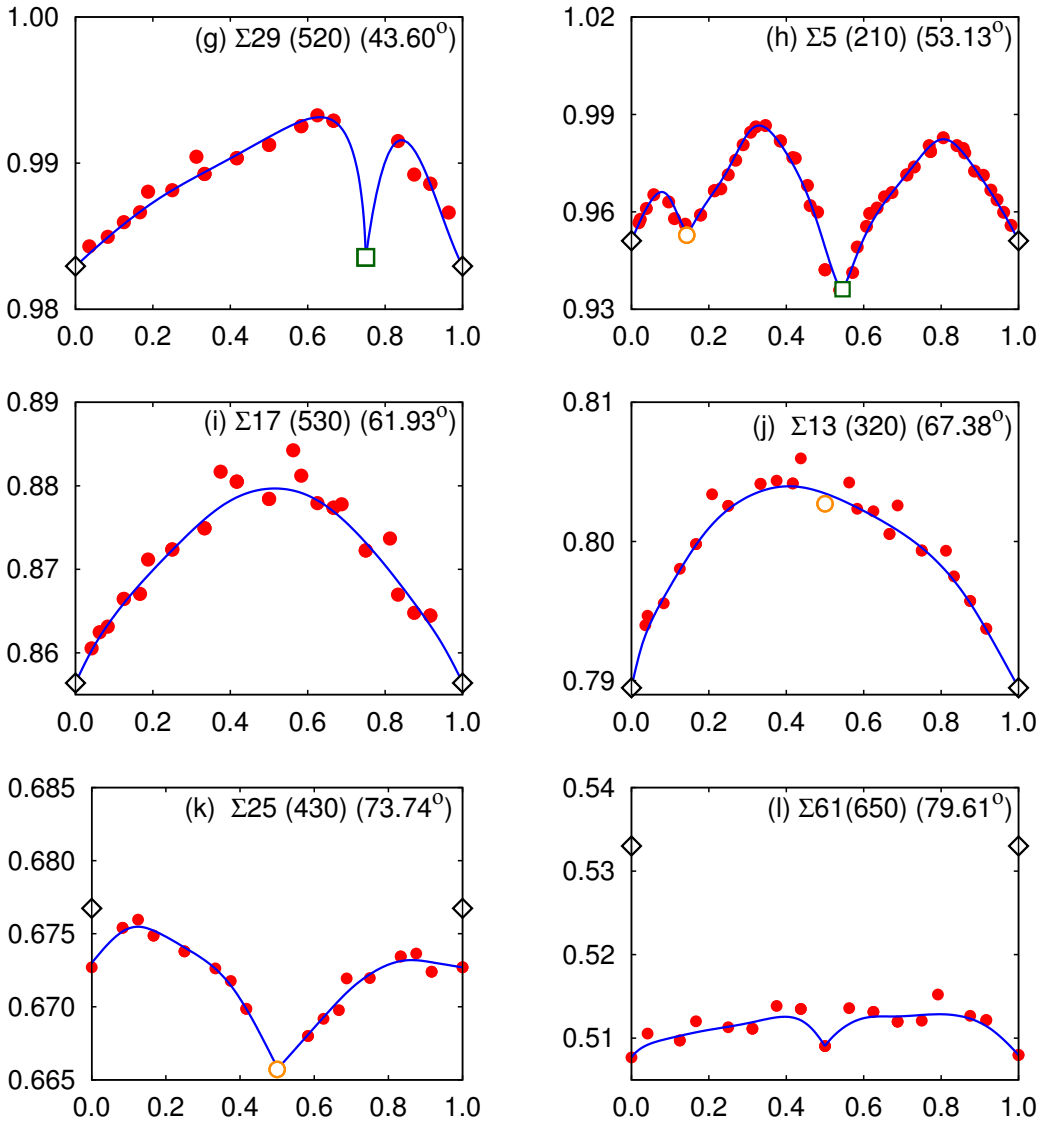

Figure A.2: GB energy (in J/m^2) versus GB density λ (fraction of atoms removed) for symmetrical tilt GBs in Cu.

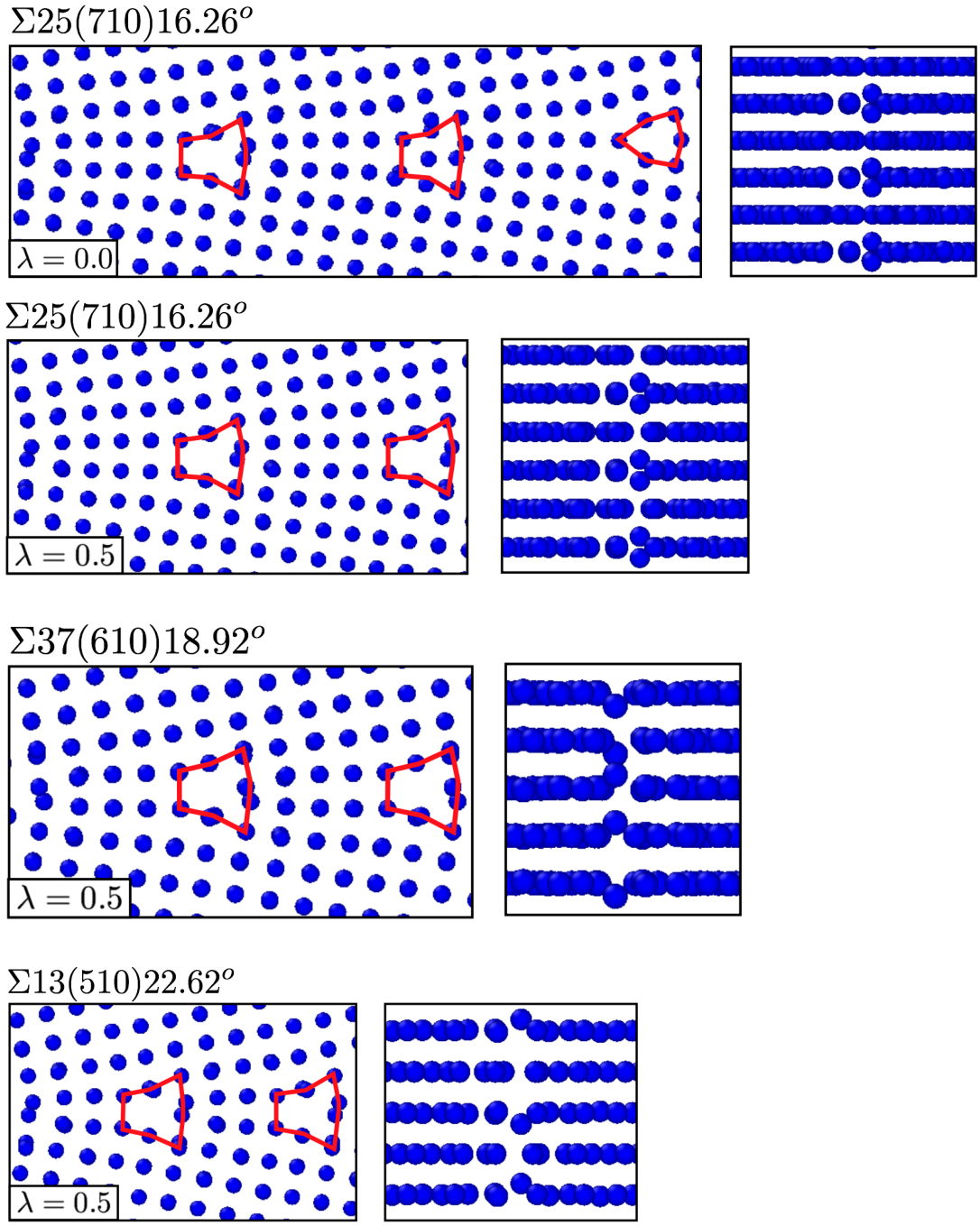

Figure A.3: Structures of symmetrical tilt GBs in Cu. The structures are projected parallel to the [001] tilt axis (left) and normal to the tilt axis (right). The GB density λ are indicated.

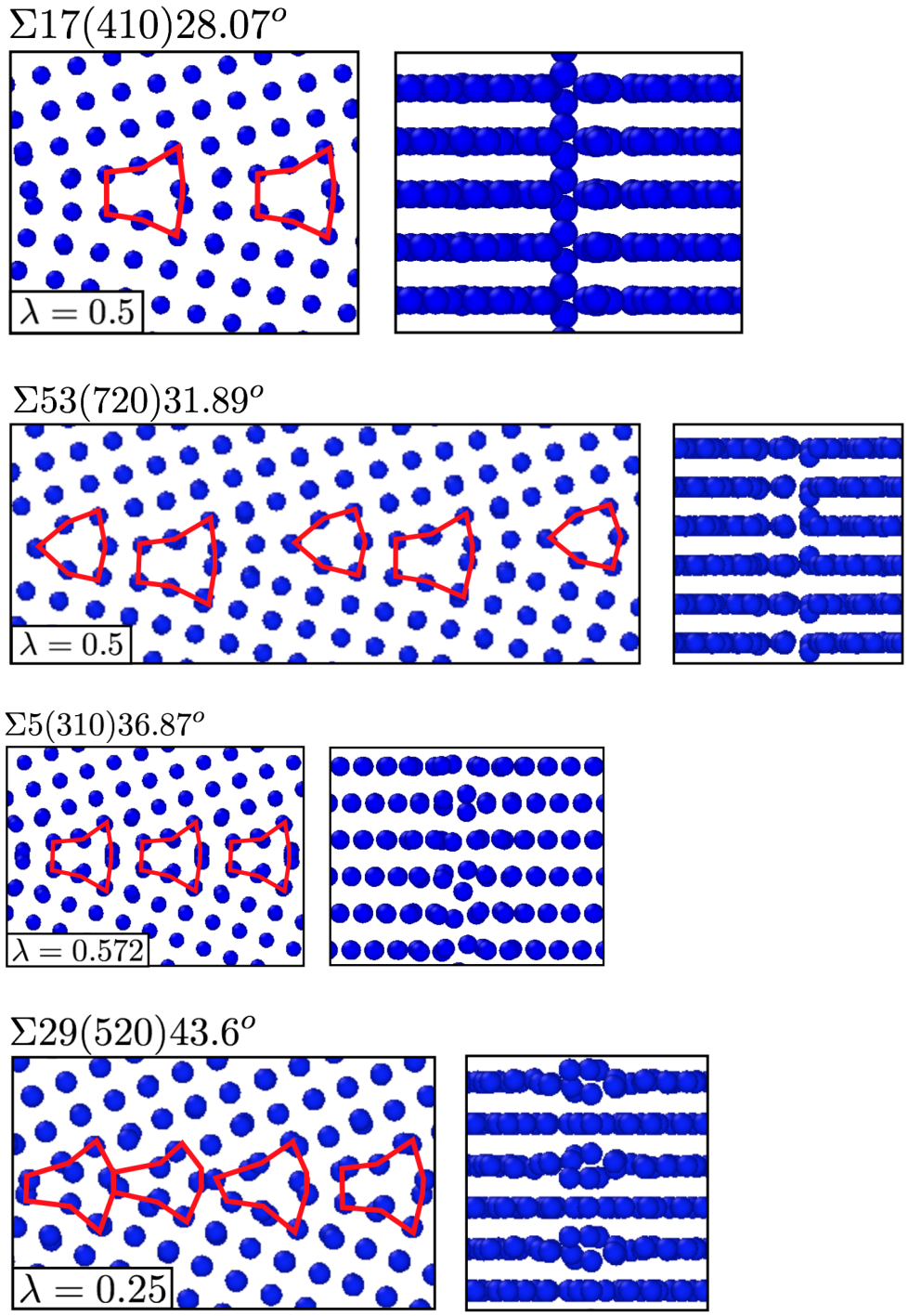

Figure A.4: Structures of symmetrical tilt GBs in Cu. The structures are projected parallel to the [001] tilt axis (left) and normal to the tilt axis (right). The GB density λ is indicated.

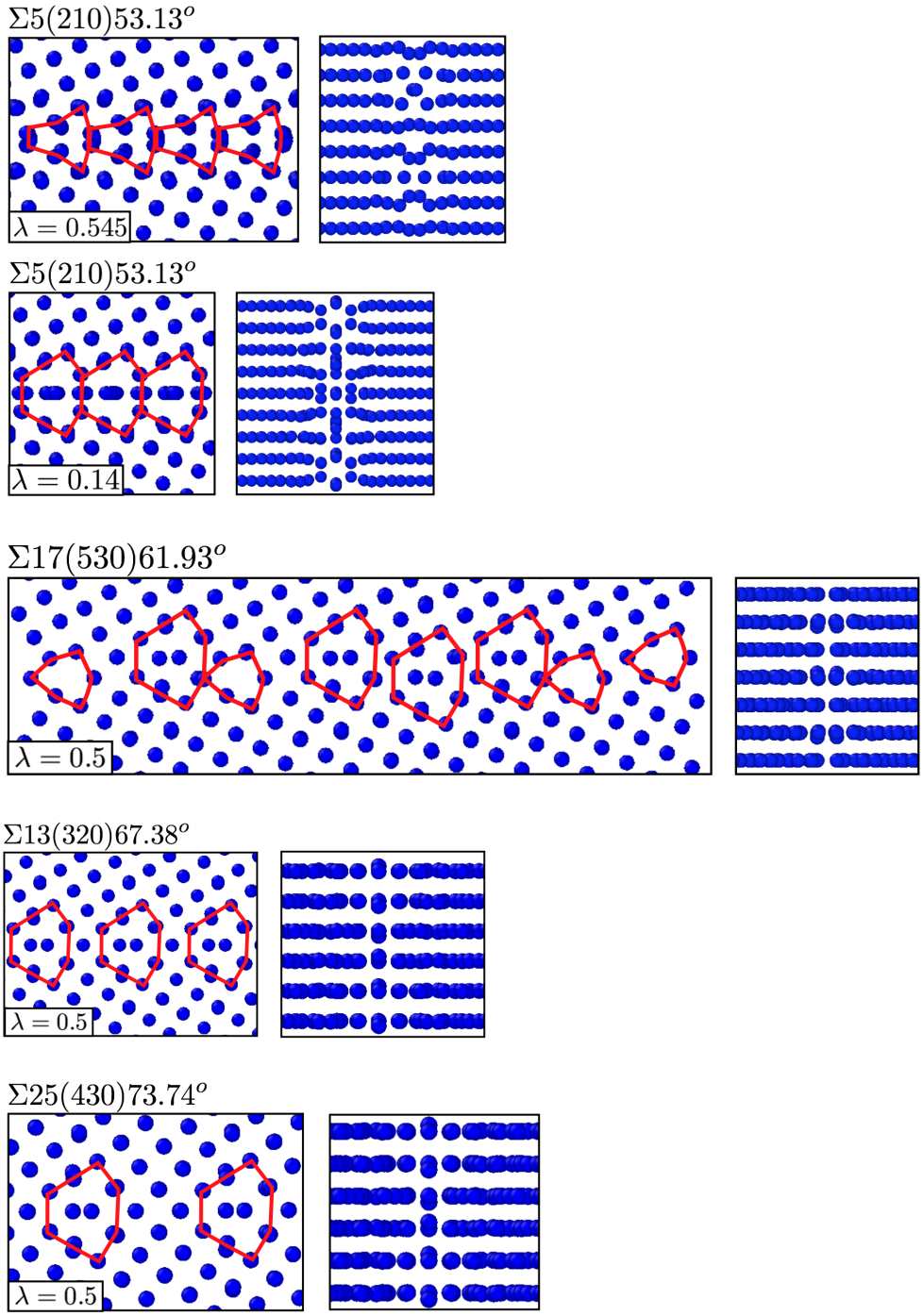

Figure A.5: Structures of symmetrical tilt GBs in Cu. The structures are projected parallel to the [001] tilt axis (left) and normal to the tilt axis (right). The GB density λ is indicated.

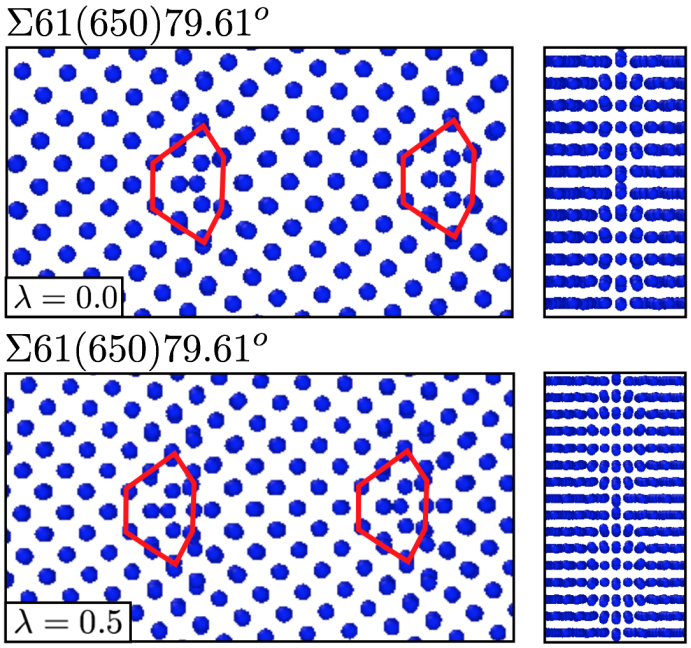

Figure A.6: Structures of symmetrical tilt GBs in Cu. The structures are projected parallel to the [001] tilt axis (left) and normal to the tilt axis (right). The GB density λ is indicated. The structures are composed of M units whose connection to each other alternates along the tilt axis from head-to-tail to separated by an extra plane. This explains why the projection along the tilt axis does not look like in other boundaries.

Bibliography

Bibliography

[1] Adland, A., Karma, A., Spatschek, R., Buta, D., and Asta, M. (2013). Phase-field-crystal study of grain boundary premelting and shearing in bcc iron. *Phys. Rev.* B, 87:024110.

[2] Alsayed, A. M., Islam, M. F., Zhang, J., Collings, P. J., and Yodh, A. G. (2005). Premelting at defects within bulk colloidal crystals. *Science*, 309:1207–1210.

[3] Asadi, E. and Zaeem, M. A. (2015). A review of quantitative phase-field crystal modeling of solid–liquid structures. *JOM*, 67:186–201.

[4] Balluffi, R. W. and Maurer, R. (1988). On rotating sphere-on-plate experiments and the question of whether high angle grain boundaries melt below bulk meting temperatures. *Scripta Metall.*, 22:709.

[5] Baram, M., Chatain, D., and Kaplan, W. D. (2011). Nanometer-thick equilibrium films: The interface between thermodynamics and atomistics. *Science*, 332(6026):206–209.

[6] Becker, C. A. (2011). Atomistic simulations for engineering: Potentials and challenges. In *Tools, Models, Databases and Simulation Tools Developed and Needed to Realize the Vision of ICME*. ASM.

[7] Berry, J., Elder, K. R., and Grant, M. (2008). Melting at dislocations and grain boundaries: A phase field crystal study. *Phys. Rev.* B, 77:224114.

[8] Besold, G. and Mouritsen, O. G. (1994). Grain-boundary melting: A monte carlo study. *Phys. Rev.* B, 50:6573 – 6576.

[9] Besold, G. and Mouritsen, O. G. (2000). Competition between domain growth and interfacial melting. *Comp. Mater. Sci.*, 18:225–244.

[10] Boninsegni, M. and Prokof'ev, N. (2012). Colloquium: Supersolids: What and where are they? *Rev. Mod. Phys.*, 84:759–776.

[11] Broughton, J. Q. and Gilmer, G. H. (1986). Thermodynamic criteria for grain boundary melting: A molecular-dynamics study. *Phys. Rev. Lett.*, 56:2692–2695.

[12] Broughton, J. Q. and Gilmer, G. H. (1998). Grain-boundary shearing as a test for interface melting. *Modelling Simul. Mater. Sci. Eng.*, 6:87–97.

[13] Brown, J. A. and Mishin, Y. (2004). Effect of surface stress on Ni segregatin in (110) NiAl thin films. *Phys. Rev.* B, 69:195407.

[14] Brown, J. A. and Mishin, Y. (2005). Segregation and structural transformations at $\Sigma 3$ grain boundaries in NiAl: A Monte Carlo study. *Acta Mater.*, 53:2149–2156.

[15] Cahn, J. W. (1979). Thermodynamics of solid and fluid surfaces. In Johnson, W. C. and Blackely, J. M., editors, *Interface Segregation*, chapter 1, pages 3–23. American Society of Metals, Metals Park, OH.

[16] Cahn, J. W. (1982). Transitions and phase equilibria among grain boundary structures. *J. Physique Colloques*, 43(C6):199–213.

[17] Cahn, J. W., Mishin, Y., and Suzuki, A. (2006). Coupling grain boundary motion to shear deformation. *Acta Mater.*, 54:4953–4975.

[18] Callen, H. (1965). Thermodynamic fluctuations. *American Journal of Physics*, 33:919–922.

[19] Callen, H. B. (1985). *Thermodynamics and an introduciton to thermostatistics*. Wiley, New York, second edition.

[20] Callen, H. B. and Welton, T. A. (1951). Irreversibility and generalized noise. *Phys. Rev.*, 83:34–40.

[21] Cantwell, P. R., Tang, M., Dillon, S. J., Luo, J., Rohrer, G. S., and Harmer, M. P. (2013). Grain boundary complexions. *Acta Mater.*, 62:1–48.

[22] Chiu, T. C. P., Swanson, D. R., Adriaans, M. J., Nissen, J. A., and Lipa, J. A. (1992). Temperatue fluctuations in the canonical ensemble. *Phys. Rev. Lett.*, 69:3005–3009.

[23] Ciccotti, G., Guillope, M., and Pontikis, V. (1983). High-angle grain-boundary transition: A molecular-dynamics study. *Phys. Rev.* B, 27:5576–5585.

[24] commons.wikimedia.org. (2009). Cubique-a-faces-centrees-atomes-par-maille.svg.

[25] commons.wikimedia.org. (2013). Tiltandtwistboundaries-remade.jpg.

[26] Craven, C., Dosseh, G., Rousseau, B., and Fuchs, A. H. (1990). Grain boundary premelting in crystalline benzene as studied by proton N.M.R. *Journal de Physique*, 51:2489–2499.

[27] Daw, M. S. and Baskes, M. I. (1984). Embedded-atom method: Derivation and application to impurities, surfaces, and other defects in metals. *Phys. Rev.* B, 29:6443–6453.

[28] Dicky, J. and Paskin, A. (1969). Computer simulation of the lattice dynamics of solids. *Phys. Rev.*, 188:1407–1418.

[29] Divinski, S. V., Lohman, M., Herzig, C., Straumal, B., Baretzky, B., and Gust, W. (2005). Grain-boundary melting phase transition in the Cu-Bi system. *Phys. Rev.* B, 71:104104.

[30] Falcioni, M., Villamaina, D., Vulpiani, A., Puglisi, A., and Sarracino, A. (2011). Estimate of temperature and its uncertainty in small systems. *Am. J. Phys.*, 79:777–785.

[31] Fensin, S. J., Olmsted, D., Buta, D., Asta, M., Karma, A., and Hoyt, J. J. (2010). Structural disjoining potential for grain-boundary premelting and grain coalescence from molecular-dynamics simulations. *Phys. Rev.* E, 81:031601.

[32] Foiles, S. M. (1994). Evaluation of harmonic methods for calculating the free energy of defects in solids. *Phys. Rev.* B, 49:14930–14938.

[33] Forgacs, G., Lipowsky, R., and Nieuwenhuizen, T. M. (1991). The behavior of interfaces in ordered and disordered systems. In Domb, C. and Lebowitz, J., editors, *Phase transitions and critical phenomena*, volume 14, chapter 2, pages 135–364. Academic Press, San Diego.

[34] Frenkel, D. and Smit, B. (2002). *Understanding molecular simulation: from algorithms to applications*. Academic, San Diego, second edition.

[35] Frolov, T. (2014). Effect of interfacial structural phase transformations on the coupled motion of grain boundaries: A molecular dynamics study. *Appl. Phys. Lett.*, 104:211905.

[36] Frolov, T., Asta, M., and Mishin, Y. (2016). Phase transformations at interfaces: Observations from atomistic modeling. *Current Opinion in Solid State and Materials Science*, 20:308–315.

[37] Frolov, T., Divinski, S. V., Asta, M., and Mishin, Y. (2013a). Effect of interface phase transformations on diffusion and segregation in high-angle grain boundaries. *Phys. Rev. Lett.*, 110:255502.

[38] Frolov, T., M.Asta, and Mishin, Y. (2015). Segregation-induced phase transformations in grain boundaries. *Phys. Rev.* B, 92:020103(R).

[39] Frolov, T. and Mishin, Y. (2009a). Solid-liquid interface free energy in binary systems: Theory and atomistic calculations for the (110) cu-ag interface. *J. Chem. Phys.*, 131:054702.

[40] Frolov, T. and Mishin, Y. (2009b). Temperature dependence of the surface free energy and surface stress: and atomistic calculation for cu (110). *Phys. Rev.* B, 79:045430.

[41] Frolov, T. and Mishin, Y. (2010a). Effect of nonhydrostatic stresses on solid-fluid equilibrium. II. interface thermodynamics. *Phys. Rev.* B, 82:174114.

[42] Frolov, T. and Mishin, Y. (2010b). Orientation dependence of the solid–liquid interface stress: atomistic calculations for copper. *Model. Simul. Mater. Sci. Eng.*, 18:074003.

[43] Frolov, T. and Mishin, Y. (2012a). Thermodynamics of coherent interfaces under mechanical stresses. i. theory. *Phys. Rev. B*, 85:224106.

[44] Frolov, T. and Mishin, Y. (2012b). Thermodynamics of coherent interfaces under mechanical stresses. II. application to atomistic simulation of grain boundaries. *Phys. Rev. B*, 85:224107.

[45] Frolov, T. and Mishin, Y. (2015). Phases, phase equilibria, and phase rules in low-dimensional systems. *J. Chem. Phys.*, 143:044706.

[46] Frolov, T., Olmsted, D. L., Asta, M., and Mishin, Y. (2013b). Structural phase transformations in metallic grain boundaries. *Nature Communications*, 4:1899.

[47] Gibbs, J. W. (1948). On the equilibrium of heterogeneous substances. In *The collected works of J. W. Gibbs*, volume 1, pages 55–349. Yale University Press, New Haven.

[48] Gottstein, G., Molodov, D. A., and Shvindlerman, L. S. (1998). Grain boundary migration in metals: Recent developments. *Interface Sci.*, 6:7–22.

[49] Guillope, M., Ciccotti, G., and Pontikis, V. (1984). Relation between intergranular diffusion and structure: A molecular dynamics study. *Surface Sci.*, 144:67–76.

[50] Gupta, V. K., Yoon, D. H., Meyer, H. M., and Luo, J. (2007). Thin intergranular films and solid-state activated sintering in nickel-doped tungsten. *Acta Mater.*, 55:3131–3142.

[51] Hashibon, A., Adler, J., Finnis, M. W., and Kaplan, W. D. (2001). Ordering at solid-liquid interfaces between dissimilar materials. *Interface Sci.*, 9:175–181.

[52] Hashibon, A., Adler, J., Finnis, M. W., and Kaplan, W. D. (2002). Atomistic study of structural correlations at a liquid-solid interface. *Comput. Mat. Sci.*, 24:443–452.

[53] Hickman, J. and Mishin, Y. (2016a). Disjoining potential and grain boundary premelting in binary alloys. *Phys. Rev.* B, 93:224108.

[54] Hickman, J. and Mishin, Y. (2016b). Temperature fluctuations in canonical systems: Insights from molecular dynamics simulations. *Physical Review B*, 94(18):184311.

[55] Hickman, J. and Mishin, Y. (2017). Extra variable in grain boundary description. *Physical Review Materials*, 1(1):010601.

[56] Hoyt, J. J., Olmsted, D., Jindal, S., Asta, M., and Karma, A. (2009). Method for computing short-range forces between solid-liquid interfaces driving grain boundary premelting. *Phys. Rev.* E, 79:020601.

[57] Hsieh, T. E. and Balluffi, R. W. (1989). Experimental study of grain boundary melting in aluminum. *Acta Metall.*, 37:1637–1644.

[58] https://software.nasa.gov/software/LAR 18773-1 (The ParaGrandMC code can be obtained from the NASA Software Catalog).

[59] Huang, P. Y., Ruiz-Vargas, C. S., van der Zande, A. M., Whitney, W. S., Levendorf, M. P., Kevek, J. W., Garg, S., Alden, J. S., Hustedt, C. J., Zhu, Y., Park, J., McEuen, P. L., and Muller, D. A. (2011). Grains and grain boundaries in single-layer graphene atomic patchwork quilts. *Nature*, 469:389–392.

[60] Inoko, F., Okada, T., Muraga, T., Nakano, Y., and Yoshikawa, T. (1997). Strain induced grain boundary premelting in bulk copper bicrystals. *Interface Sci.*, 4:263–272.

[61] Kaplan, W. D. and Kauffmann, Y. (2006). Structural order in liquids induced by interfaces with crystals. *Annu. Rev. Mater. Res.*, 36:1–48.

[62] Keblinski, P., Wolf, D., Phillpot, S. R., and Gleiter, H. (1999). Self-diffusion in high-angle fcc metal grain boundaries by molecular dynamics simulations. *Philos. Mag. A*, 79:2735.

[63] Kittel, C. (1973). On the nonexistence of temperature fluctuations in small systems. *Am. J. Phys.*, 41:1211–1212.

[64] Kittel, C. (1988). Temperature fluctuation: An oxymoron. *Phys. Today*, 41:93.

[65] Kittel, C. and Kroemer, H. (2000). *Thermal physics*. Freeman, W. H. & Company, New York, NY, second edition.

[66] Kong, L. T. (2011). Phonon dispersion measured directly from molecular dynamics simulations. *Comp. Phys. Comm.*, 182:2201–2207.

[67] Kubo, R. (1966). The fluctuation-dissipation theorem. *Rep. Prog. Phys.*, 29:255–285.

[68] Kubo, R., Toda, M., and Hashitsume, N. (1991). *Statistical Physics II. Nonequilibrium statistical mechanics*, volume 31 of *Solid-State Sciences*. Springer-Verlag, Berlin, Heidelberg, New York, second edition.

[69] Landau, D. P. and Binder, K. (2009). *A guide to Monte Carlo simulations in statistical physics*. Cambridge University Press, Cambridge, third edition.

[70] Landau, L. D. and Lifshitz, E. M. (2000). *Statistical Physics, Part I*, volume 5 of *Course of Theoretical Physics*. Butterworth-Heinemann, Oxford, third edition.

[71] Larché, F. C. and Cahn, J. W. (1985). The interactions of composition and stress in crystalline solids. *Acta Metall.*, 33:331–367.

[72] Lebowitz, J. L., Percus, J. K., and Verlet, L. (1967). Ensemble dependence of fluctuations with application to machine computing. *Phys. Rev.*, 153:250–254.

[73] Liang, T., Devine, B., Phillpot, S. R., and Sinnott, S. B. (2012). Variable charge reactive potential for hydrocarbons to simulate organic-copper interactions. *J. Phys. Chem.*, 116:7976–7991.

[74] Lipowsky, R. (1986). Melting at grain boundaries and surfaces. *Phys. Rev. Lett.*, 57:2876.

[75] Lipowsky, R. and Fisher, M. E. (1987). Scaling regimes and functional renormalization for wetting transitions. *Phys. Rev.* B, 36:2126–2141.

[76] Liu, C. L. and Plimpton, S. J. (1995). Molecular statics and dynamics study of diffusion along [001] tilt grain boundaries in ag. *Phys. Rev.* B, 51:4523–4528.

[77] Lobkovsky, A. and Warren, J. W. (2002). Phase field model of premelting of grain boundaries. *Physica D*, 164:202–212.

[78] Lu, J. and Szpunar, J. A. (1995). Molecular dynamics simulation of a twist $\sigma = 5$ grain boundary. *Interface Sci.*, 3:143–150.

[79] Lu, L. L., Hu, T. T., Lu, G. M., and Chen, Z. (2014). Phase-field crystal study of segregation induced grain-boundary premelting in binary alloys. *Physica* B, 451:128–133.

[80] Luo, J., Gupta, V. K., Yoon, D. H., and Meyer, H. M. (2005). Segregation-induced grain boundary premelting in nickel-doped tungsten. *Appl. Phys. Lett.*, 87:231902.

[81] Lutsko, J. F., Wolf, D., Phillpot, S. R., and Yip, S. (1989). Molecular-dynamics study of lattice-defect-nucleated melting in metals using an embedded-atom-method potential. *Phys. Rev.* B, 40:2841–2855.

[82] Lutsko, J. F., Wolf, D., Yip, S., Phillpot, S. R., and Nguyen, T. (1988). Molecular-dynamics method for the simulation of bulk-solid interfaces at high temperatures. *Phys. Rev.* B, 38:11572–11581.

[83] Ma, C., Sun, H., Zhao, Y., Li, B., Li, Q., Zhao, A., Wang, X., Luo, Y., Yang, J., Wang, B., and Hou, J. G. (2014). Evidence of van Hove singularities in ordered grain boundaries of graphene. *Phys. Rev. Lett.*, 112:226802.

[84] Mandelbrot, B. B. (1989). Temperature fluctuations: A well-defined and unavoidable notion. *Phys. Today*, 42:71–73.

[85] Marconi, U. M. B., Puglisi, A., Rondoni, L., and Vulpiani, A. (2008). Fluctuation–dissipation: Response theory in statistical physics. *Physics Reports*, 461:111–195.

[86] Masumura, R. A., Glicksman, M. E., and Vold, C. L. (1972). Absolute solid-liquid and grain boundary energies of bismuth. *Scripta Metall.*, 6:943–946.

[87] De Groot, S. R. and Mazur, P. (1984). *Non-equilibrium thermodynamics*. Dover, New York.

[88] Palafox-Hernandez, J. P., Laird, B. B., and Asta, M. (2011). Atomistic characterization of the cu–pb solid–liquid interface. *Acta Mater.*, 59:3137–3144.

[89] von Alfthan, S., Haynes, P. D., Kashi, K., and Sutton, A. P. (2006). Are the structures of twist grain boundaries in silicon ordered at 0 K? *Phys. Rev. Lett.*, 96:055505.

[90] von Alfthan, S., Kaski, K., and Sutton, A. P. (2007). Molecular dynamics simulations of temperature-induced structural transitions at twist boundaries in silicon. *Phys. Rev.* B, 76:245317.

[91] Mellenthin, J., Karma, A., and Plapp, M. (2008). Phase-field crystal study of grain-boundary premelting. *Phys. Rev.* B, 78:184110.

[92] Mishin, Y. (2014). Calculation of the γ/γ' interface free energy in the Ni-Al system by the capillary fluctuation method. *Modeling Simul. Mater. Sci. Eng.*, 22:045001.

[93] Mishin, Y. (2015). Thermodynamic theory of equilibrium fluctuations. *Annals of Physics*, 363:48–97.

[94] Mishin, Y., Asta, M., and Li, J. (2010). Atomistic modeling of interfaces and their impact on microstructure and properties. *Acta Mater.*, 58:1117 – 1151.

[95] Mishin, Y., Boettinger, W. J., Warren, J. A., and McFadden, G. B. (2009). Thermodynamics of grain boundary premelting in alloys. I. Phase field modeling. *Acta Mater.*, 57:3771–3785.

[96] Mishin, Y., Farkas, D., Mehl, M. J., and Papaconstantopoulos, D. A. (1999). Interatomic potentials for monoatomic metals from experimental data and ab initio calculations. *Phys. Rev.* B, 59:3393–3407.

[97] Mishin, Y. and Hickman, J. (2016). Energy spectrum of a langevin oscillator. *Physical Review E*, 94(6):062151.

[98] Mishin, Y., Mehl, M. J., and Papaconstantopoulos, D. A. (2005). Phase stability in the Fe-Ni system: Investigation by first-principles calculations and atomistic simulations. *Acta Mater.*, 53:4029–4041.

[99] Mishin, Y., Mehl, M. J., Papaconstantopoulos, D. A., Voter, A. F., and Kress, J. D. (2001). Structural stability and lattice defects in copper: Ab initio, tight-binding and embedded-atom calculations. *Phys. Rev. B*, 63:224106.

[100] Nguyen, T., Ho, P. S., Kwok, T., Nitta, C., and Yip, S. (1992). Thermal structural disorder and melting at a crystalline interface. *Phys. Rev.* B, 46:6050–6060.

[101] Nyquist, H. (1928). Thermal agitation of electric charge in conductors. *Phys. Rev.*, 32(110-113).

[102] Oh, S. H., Kauffmann, Y., Scheu, C., Kaplan, W. D., and Ruhle, M. (2005). Ordered liquid aluminum at the interface with sapphire. *Science*, 310:661–663.

[103] Onsager, L. (1931a). Reciprocal relations in irreversible processes. I. *Phys. Rev.*, 37:405–426.

[104] Onsager, L. (1931b). Reciprocal relations in irreversible processes. II. *Phys. Rev.*, 38:2265–2279.

[105] Pandit, R., Schick, M., and Wortis, M. (1982). Systematics of multilayer adsorption phenomena on attractive substrates. *Phys. Rev.* B, 26:5112–5140.

[106] Phillpot, S. R. and Rickman, J. M. (1992). Simulated quenching to the zero-temperature limit of the grand-canonical ensemble. *J. Chem. Phys.*, 97:2651–2658.

[107] Plimpton, S. (1995). Fast parallel algorithms for short-range molecular-dynamics. *J. Comput. Phys.*, 117:1–19.

[108] Pollet, L., Boninsegni, M., Kuklov, A., and Toyer, M. (2007). Superfluidity of grain boundaries in solid He 4. *Phys. Rev. Lett.*, 98:135301.

[109] Purja Pun, G. P., Yamakov, V., and Mishin, Y. (2015). Interatomic potential for the ternary Ni–Al–Co system and application to atomistic modeling of the B2–$L1_0$ martensitic transformation. *Model. Simul. Mater. Sci. Eng.*, 23:065006.

[110] Rappaz, M., Jacot, A., and Boettinger, W. J. (2003). Last-stage solidification of alloys: Theoretical model of dendrite-arm and grain coalescence. *Metall. Mater. Trans.* A, 34:467–479.

[111] Rivnay, J., Jimison, L. H., Northrup, J. E., Toney, M. F., Noriega, R., Lu, S., Marks, T. J., Facchetti, A., and Salleo, A. (2009). Large modulation of carrier transport by grain-boundary molecular packing and microstructure in organic thin films. *Nature Mater.*, 8:952 – 958.

[112] Rowan, E. (2013). *The structural disjoining potential of grain boundary premelting in binary alloys using phase field crystal model.* Master of Applied Science Thesis, McMaster University, Hamilton, Ontario, Canada.

[113] Rudoi, Y. D. and Sukhanov, A. D. (2000). Thermodynamic fluctuations within the gibbs and einstein approaches. *Phys. Usp.*, 43:1169–1199.

[114] Sadigh, B., Erhart, P., Stukowski, A., Caro, A., Martinez, E., and Zepeda-Ruiz, L. (2012). Scalable parallel monte carlo algorithm for atomistic simulations of precipitation in alloys. *Phys. Rev.* B, 85:184203.

[115] Scheidler, P., Kob, W., Latz, A., Horbach, J., and Binder, K. (2001). Frequency dependent specific heat of viscous silica. *Phys. Rev.* B, 63:104204.

[116] Spatschek, R., Adland, A., and Karma, A. (2013). Structural short-range forces between solid-melt interfaces. *Phys. Rev.* B, 87:024109.

[117] Sutton, A. P. and Balluffi, R. W. (1995). *Interfaces in Crystalline Materials.* Clarendon Press, Oxford.

[118] Sutton, A. P. and Vitek, V. (1983). On the structure of tilt grain boundaries in cubic metals - I. symmetrical tilt boundaries. *Phil. Trans. Roy. Soc. Lond. A*, 309:1–36.

[119] Suzuki, A. and Mishin, Y. (2003). Atomistic modeling of point defects and diffusion in copper grain boundaries. *Interface Science*, 11:131–148.

[120] Suzuki, A. and Mishin, Y. (2005). Atomic mechanisms of grain boundary diffusion: Low versus high temperatures. *J. Mater. Sci.*, 40:3155–3161.

[121] Tang, M., Carter, W. C., and Cannon, R. M. (2006a). Diffuse interface model for structural transitions of grain boundaries. *Phys. Rev.* B, 73:024102.

[122] Tang, M., Carter, W. C., and Cannon, R. M. (2006b). Grain boundary transitions in binary alloys. *Phys. Rev. Lett.*, 97:075502.

[123] Tersoff, J. (1988). New empirical approach for the structure and energy of covalent systems. *Phys. Rev.* B, 37:6991–7000.

[124] Thomson, E. S., Hansen-Goos, H., Wettlaufer, J. S., and Wilen, L. A. (2013). Grain boundary melting in ice. *J. Chem. Phys.*, 138:124707.

[125] van Duin, A. C. T., Dasgupta, S., Lorant, F., and Goddard, W. A. (2001). Reaxff: A reactive force field for hydrocarbons. *J. Phys. Chem.*, 105:9396–9409.

[126] van Hemmen, J. L. and Longtin, A. (2013). Temperature fluctuations for a system in contact with a heat bath. *J. Statist. Phys.*, 153:1132–1142.

[127] Vold, C. L. and Glicksman, M. E. (1972). Behavior of grain boundaries near the melting point. In Hu, H., editor, *The Nature and Behavior of Grain Boundaries*, pages 171–183. Metallurgical Society of AIME, Plenum Press, New York.

[128] Wang, N., Spatschek, R., and Karma, A. (2010). Multi-phase-field analysis of short-range forces between diffuse interfaces. *Phys. Rev.* E, 81:051601.

[129] Watanabe, T., Kimura, S. I., and Karashima, S. (1984). The effect of grain boundary structural transformation on sliding in (1010)-tilt zinc bicrystals. *Philos. Mag.* A, 49:845–864.

[130] Williams, P. L. and Mishin, Y. (2009). Thermodynamics of grain boundary premelting in alloys. II. Atomistic simulation. *Acta Mater.*, 57:3786–3794.

[131] Williams, P. L., Mishin, Y., and Hamilton, J. C. (2006). An embedded-atom potential for the Cu-Ag system. *Modelling Simul. Mater. Sci. Eng.*, 14:817–833.

[132] Yamakov, V., Hochhalter, J. D., Leser, W. P., Warner, J. E., Newman, J. A., Purja Pun, G. P., and Mishin, Y. (2015). Multiscale modeling of sensory properties of co–ni–al shape memory particles embedded in an al metal matrix. *J. Mate. Sci.*, 5:1204–1216.

Curriculum Vitae

James F. Hickman
Department of Physics and Astronomy
George Mason University
4400 University Dr, Fairfax, VA 22030
phone: (717)-261-6982 email: jhickma3@gmu.edu

Education:

- **2011-2014:** George Mason University:
  - Masters of science: applied physics (December 2014) (4.0/4.0 GPA)
- **2011:** Lock Haven University:
  - Nanotechnology fabrication certification (Summer 2011)(3.567/4.0 GPA)
  - Certification obtained in collaboration with the Pennsylvania State University
- **2007-2011:** Shippensburg University:
  - Bachelor of science: (June 2011)(3.87/4.0 GPA)
    - Double major in physics and applied mathematics

Research experience:

- **2012-2017:** George Mason University: Graduate research assistant
  - Advisor: Professor Yuri Mishin
- **2010:** George Mason University: Undergraduate research experience in mathematics
  - Advisor: Professor Padmanabhan Seshaiyer

Publications:

- **2017:** J. Hickman and Y. Mishin, Effect of bi-crystallography on thermal resistance in silicon grain boundaries. (in preparation).

- **2017:** J. Hickman and Y. Mishin, Extra variable in grain boundary description. Physical Review Materials 1, No. 1, p. 010601, [selected as EDITOR'S SUGGESTION].
- **2016:** J. Hickman and Y. Mishin, Disjoining potential and grain boundary premelting in bi- nary alloys. Physical Review B 93, No. 224108.
- **2016:** Y. Mishin and J. Hickman, Energy spectrum of a Langevin oscillator. Physical Review E 94, No. 6, p. 062151.
- **2016:** J. Hickman and Y. Mishin, Temperature fluctuations in canonical systems: Insights from molecular dynamics simulations. Physical Review B 94, No. 184311.

Academic Presentations:

- **2017:** Atomistic simulations of solid state systems: Introduction and applications. Shippensburg University Student Seminar Series (Shippensburg Pa).
- **2017:** Effect of bi-crystallography on thermal resistance of grain boundaries. The Minerals, Metals and Materials Society Annual Meeting and Exhibition (INVITED)(San Diego Ca).
- **2016:** Atomistic modeling of pre-melted grain boundaries. XV International Conference on Intergranular and Interphase Boundaries in Materials (Moscow).
- **2016:** Equilibrium fluctuations of grain boundary properties in alloy systems. The Minerals, Metals and Materials Society Annual Meeting and Exhibition (Nashville Tn).
- **2015:** Atomistic modeling of pre-melted grain boundaries. The Minerals, Metals and Materials Society Annual Meeting and Exhibition (Orlando Fl).
- **2014:** Fluctuations in pre-melted grain boundaries. The Minerals, Metals and Materials Society Annual Meeting and Exhibition (San Diego Ca).
- **2014:** Thermodynamic simulations and parallel processing with applications to grain boundary phenomena. Shippensburg University Student Seminar Series (Shippensburg Pa).
- **2013:** Monte Carlo simulations: The disjointing potential and grain boundary premelting in binary CuAg systems. SIAM/MAA Fourth Mid-Atlantic Regional Applied Mathematics Student Conference (Shippensburg PA).

Academic workshops attended:

- **2014:** Mason mathematical modeling workshop. Fairfax, VA (host: George Mason University).
- **2014:** Open knowledge-base of interatomic models content workshop. College Park, MD (host: University of Maryland).

- **2013:** LAMMPS users workshop and symposium. Albuquerque, NM (host: Sandia National Laboratory).
- **2013:** Short course in modeling materials. Argonne, IL (host: Argonne National Laboratory).

Teaching experience:

- **2016-2017:** George Mason University: Athletic department math and physics tutor
- **2015-2016:** George Mason University: Substitute recitation instructor
- **2015:** Seoul Korea: Computational physics instructor
  - Week-1: Seoul Science High School
  - Week-2: Seoul High School
- **2013-2014:** Educational Connections: Private in home math and physics tutor
- **2012-2013:** Oak Hill Elementary: After school math coach
- **2011-2012:** George Mason University: Graduate teaching assistant
  - Instructor for six sections of introductory physics
- **2008-2011:** Shippensburg University Learning Center: Math and physics tutor
  - certification as a CRLA Level-3 tutor.

STEM community outreach:

- **2016:** Arlington Traditional Elementary School: STEM day volunteer assistant
- **2015:** Lake Braddock Middle School: After school science club presenter
- **2015:** Centerville High School: Volunteer science fair judge
- **2015:** Arlington Traditional Elementary School: STEM day volunteer assistant
- **2014-2015:** Fairfax County: VEX Robotics Coach
- **2014:** Robeson High School: After school science club presenter
- **2012-2013:** George Mason University: Paul Robeson leadership academy coach